Near-field investigation of surface plasmon polaritons

Jincy Jose

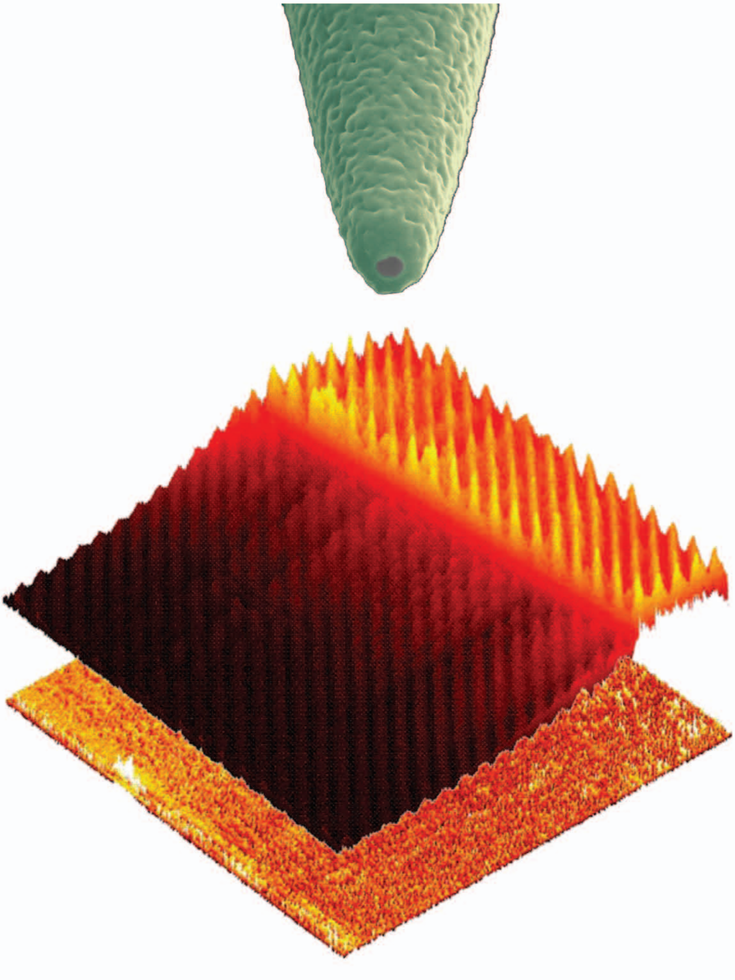

NEAR-FIELD INVESTIGATION OF SURFACE PLASMON POLARITONS

Thesis committee members:

Prof. dr. G. van der Steenhoven	University of Twente, The Netherlands
Prof. dr. J. L. Herek	University of Twente, The Netherlands
Dr. ir. H. L. Offerhaus	University of Twente, The Netherlands
Prof. dr. W. L. Barnes	University of Exeter, United Kingdom
Dr. M. P van Exter	University of Leiden, The Netherlands
Prof. dr. L. Kuipers	University of Twente, The Netherlands
Prof. dr. J. Huskens	University of Twente, The Netherlands

This research has been supported by NanoNed, a national nanotechnology program coordinated by the Dutch Ministry of Economic Affairs (flagship and project number: Advanced nanoprobing, 6942).

This research has been carried out at:
Optical Sciences group,
Mesa$^+$ Institute for Nanotechnology,
Department of Science and Technology (TNW),
University of Twente,
Enschede, The Netherlands

ISBN: 978-90-365-3091-0
DOI: 10.3990/1.9789036530910
printed by GVO drukkers, Ede, The Netherlands

NEAR-FIELD INVESTIGATION OF SURFACE PLASMON POLARITONS

DISSERTATION

to obtain
the degree of doctor at the University of Twente,
on the authority of the rector magnificus,
prof. dr. H. Brinksma,
on account of the decision of the graduation committee,
to be publicly defended
on Thursday, December 9th 2010, at 13.15

by

Jincy Jose

born on 16 July 1983
in Angamaly, India

This dissertation has been approved by:

Prof. dr. J.L. Herek	(Promotor)
Dr. ir. H.L. Offerhaus	(Assistant Promotor)

“Your vision will become clear only when you can look into your heart.
Who looks outside, dreams; who looks inside, awakens.” - Carl Jung

Contents

1

Introduction

In 1704, Newton demonstrated that total internal reflection at an interface separating a denser and a rarer medium can be inhibited and predicted the existence of evanescent waves in the optically rarer medium [1, 2]. The term *evanescent* means ‘tending to vanish’. The amplitude of the evanescent wave decays exponentially away from the interface, making it impossible to detect them far away from the interface. The evanescent waves are most intense within one-third of a wavelength from the interface. The region that contains the evanescent waves is called the ‘near-field’. Near-field Optics (NFO) concerns the behavior of electromagnetic waves in structures that are small compared to the illumination wavelength or in the close vicinity of a surface. The technique of Near-field Scanning Optical Microcopy (NSOM) enables the investigation of light-matter interactions by collecting evanescent waves generated close to the interface, providing a sub-wavelength resolution.

A rapidly developing hybrid branch of optics and electronics, unraveling the optical properties of metallic thin films and nanostructures, is plasmonics. Both plasmonics and NFO can be thought of different branches in Optics, closely connected to each other. Surface Plasmon Polaritons (SPPs) [3] are electromagnetic excitations coupled to the free charges of a conductive medium (metal) and bound to an interface with a dielectric. The simplicity of plasmonics is that you do not need a sophisticated experimental setup to generate SPPs. The fundamental building blocks of a Surface Plasmon Resonance (SPR) device are a glass prism coated with a thin (around 50 nm) film of noble metal, a monochromatic light source, a photodetector, and a polarizer. The most simplest of the SPP excitation scheme is a Kretschmann-Raether configuration [4]. For p- (or parallel) polarized incident light, the evanescent waves generated in total internal reflection in the glass prism, resonantly excite SPPs on the metal-air interface. The excitation of SPPs is seen as a minimum in the intensity of light reflected off the metal film. The Kretschmann-Raether configuration is commonly used for sensing applications [5] and can be easily incorporated in an NSOM for imaging the SPPs [6].

Since their first observation [7], the presence of SPPs were commonly deduced by detecting the light reflected off the metal layer. The evanescent nature of the SPPs prevents their direct detection by far-field techniques. Direct visualization of SPPs is significant if one may want to manipulate SPPs by engineering the metal surface [8, 9]. The direct detection of SPPs is possible by introducing a sub-wavelength scatterer that can perturb and convert the SPP field into a propagating field, to be detected in the far-field. The excitation of SPPs in the Kretschmann-Raether configuration and their detection using an NSOM [10, 11, 12, 13] have found applications in sensing [5, 14, 15], focusing [8, 16], and wave-guiding [17].

1.1 Phase shifts at surface plasmon resonance

In 1947, another optical phenomenon related to the evanescent wave was demonstrated by Goos and Hänchen: a lateral displacement of the light reflected off a metal layer [18]. The so called Goos-Hänchen (GH) shift is due to the presence of the evanescent waves which undergo a phase shift with respect to the incident light [19]. The GH shift in total internal reflection, for example in a glass-air system, is of the order of the illumination wavelength [20]. Hence measuring the GH shift requires a highly stable experimental setup. An increase in the GH shift to several microns can be achieved by coating the glass surface with a metal layer [21]. Exciting SPPs on the metal surface can also be used to increase the GH shift, due to the sharp phase change at SPR. The enhancement in the GH shift has been used to improve the sensitivity of SPR sensors [22, 23, 24].

In SPR sensors, detection of the phase shift at resonance shows the highest sensitivity [22]. Most commonly, the phase shift at SPR has been measured by using the s- (or perpendicular) polarized light as a reference, since SPPs cannot be excited for that polarization. However, the phase in the s-polarized light varies slowly at SPR due to a phase change in the associated evanescent waves. In this thesis, two different approaches are demonstrated to retrieve the phase shift at SPR on a gold thin film and a gold buried grating. First, an interface that does not support SPPs, such as a glass-air interface, is used as the reference. This enables one to measure the phase shift at SPR on the gold thin film, without changing the polarization state of the incident light and hence could be a convenient approach for SPR sensing. The second approach is to extract the phase shift at SPR on the gold buried grating by using a non-resonant diffracted order as the reference.

1.2 Buried grating

The momentum of SPPs is higher than that of light of the same frequency in the free space and hence SPPs are bound to the metal-dielectric interface. The SPP field decays in a direction both perpendicular and parallel to the interface. The decay of the SPP field perpendicular to the interface leads to a field confinement on the metal surface and the decay along the interface defines the propagation length of SPPs. Due to the lossy nature of metals, the SPPs propagating along the surface reduce their energy in the form of heat into the metal [25]. In addition to the heat dissipation into the metal, the propagation length of SPPs is also influenced by the radiative damping of SPPs by surface irregularities as well as the presence of a higher refractive index medium.

A prism, a grating or a sub-wavelength scatterer are commonly used to provide the extra momentum to couple to SPPs. By combining the prism and the grating, multiple SPPs can be excited. The grating-coupled SPPs propagate on the grating and hence couple back to radiation (radiative damping), which will reduce their propagation length. A novel grating design is presented in this thesis - a grating turned up-side down referred to as a 'buried grating'. A three-dimensional view of a buried gold grating placed on top of a glass hemispherical prism, exciting multiple SPPs is shown in Fig. 1.1. The most practical benefit of using a buried grating is that one can have a flat metal surface as a template for self-assembled monolayer and functionalized bio-molecular platform for bio-sensing applications.

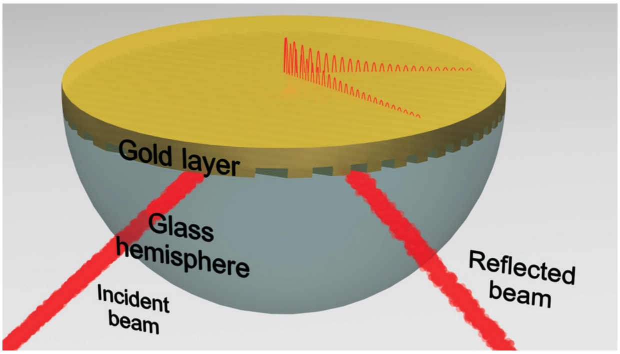

Figure 1.1: Three-dimensional view of a buried gold grating placed on top of a glass hemispherical prism exciting SPPs coupled via the grating and the prism. (Picture made by Florian sterl)

1.3 Outline of the thesis

This thesis is the merging of plasmonics and near-field optics. A near-field scanning optical microscope is used throughout the thesis to detect SPPs and investigate the phase shift and the propagation length of SPPs, which play important roles in improving the sensitivity and dynamic range of SPR sensors.

Chapter 2 gives an introduction to the field of plasmonics. Surface plasmon polaritons, their occurrence, properties, excitation, detection, attenuation and applications are briefly explained.

In Chapter 3, a brief overview of NSOM is given. Among the different NSOM configurations, the principle and operation of a Photon Scanning Tunneling Microscope (PSTM) is presented in detail. A heterodyne interferometric PSTM is demonstrated to simultaneously detect the topography of a sample surface and the amplitude and phase of the optical near-field on the surface. Applications of the PSTM such as detection of the optical intensity on the exit of an integrated waveguide, imaging of the complex SPP field on a thin gold film, and the SPP interference fields generated on a buried gold grating by combining the prism and the grating coupling schemes are demonstrated.

Chapter 4 presents the extraction of phase shifts at SPR on two different samples: a flat gold surface and a buried gold grating. In the former sample, the phase shift across a glass-gold transition region of the sample, due to the excitation of SPPs on the flat gold surface, is detected by using an adjacent glass surface as a reference. The resonant phase of SPPs excited on the buried gold grating is extracted using a non-resonant diffracted order as the reference. The phase shift measured in the former sample incorporates both the Goos-Hänchen shift and the SPR phase shift; while that in the later sample extracts the SPR phase shift.

In Chapter 5, the influence of a grating on the scattering and the propagation length of SPPs are studied. The propagation length of SPPs on two different grating designs - a buried grating and an exposed grating - are detected using the heterodyne interferometric PSTM. The full width at half maximum of the surface plasmon resonances in the near-field of the gratings and the propagation length of the SPPs beyond the gratings are measured. Furthermore, the performance of the gratings are compared for applications such as sensing and nanofocusing. Simulations based on rigorous coupled wave analysis to evaluate the figure of merit of a SPR sensor, for both gratings, are presented. Finally, a combination of a phase-matched buried grating and a tapered waveguide is proposed as a device for three-dimensional nanofocusing of SPPs.

2

Plasmonics: metal based nanooptics

2.1 Introduction

A large portion of the periodic table is occupied by metals such as alkali metals, alkaline earth metals, transition metals, post-transition metals, lanthanoids and actinoids. Metals are known for their characteristic physical, chemical, mechanical, and electrical properties. The free electrons in metals make them good reflectors, for frequencies up to the visible part of the electromagnetic spectrum [26].

The free electrons in metals undergo collective oscillations with respect to the stationary ions and the quanta of these oscillations are called plasmons. Plasmons can couple with photons or electrons to form plasmon polaritons. For small metal particles, referred to as 'metal nanoparticles' with sizes less than the wavelength of the incident electromagnetic radiation, the plasmons concentrate energy in all three dimensions within a nanoscale, and are called localized surface plasmons. The associated resonance is called the Localized Surface Plasmon Resonance (LSPR) [27] and is illustrated in Fig. 2.1a. The size-dependent optical properties of metal nanoparticles have been used to impart colors in stained glass and pottery since the time of the Romans [28].

If we make the surface of the nanoparticle larger by increasing its diameter, the three dimensional localized nature of the plasmon polaritons are lost. Instead the

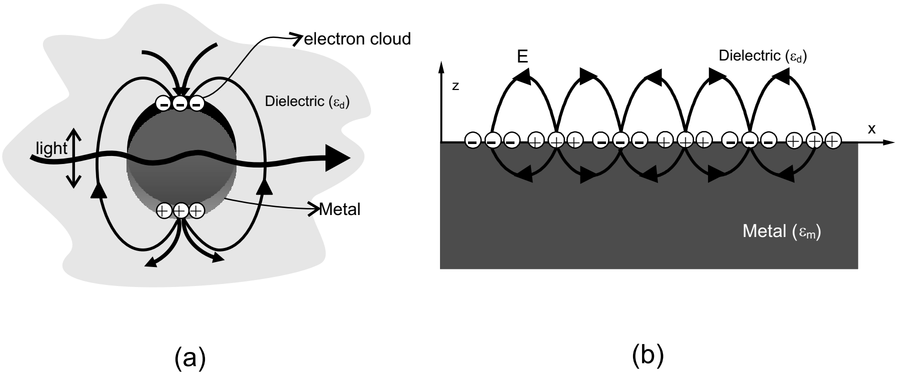

Figure 2.1: Schematic diagrams illustrating the charge and electric field associated with (a) a localized surface plasmon and (b) a surface plasmon on an extended metal film.

plasmon polaritons are confined to the surface of the metal to form Surface Plasmon Polaritons (SPPs) [29]. A widely used definition for SPPs on an extended metal surface is: "collective oscillation of conduction electrons on an interface separating a metal and a dielectric, whose amplitude decays exponentially away from the interface" [28]. The charge and electric field associated with surface plasmons on an extended metal film is depicted in Fig. 2.1b.

2.2 Surface Plasmon Polaritons (SPPs)

In 1902, Wood observed certain anomalies in the diffraction of light on a metal grating [7]. Some of those anomalies were later identified as due to the excitation of SPPs [30]. Later in 1957, Ritchie experimentally verified the excitation of SPPs on a metal surface using electron energy loss spectroscopy measurements [3]. SPPs can be understood from the dispersive (frequency dependent) property of metals and the solutions of Maxwell's equations for a metal-dielectric interface. The frequency dependent complex dielectric function, $\epsilon_{\mathrm{m}}(\omega)$ of a free electron gas [26], approximated using the Drude-Lorentz model, is given by

$$\epsilon_{\mathrm{m}}(\omega) = 1 - \frac{\omega_{\mathrm{p}}^2}{\omega^2 + \mathrm{i}\gamma\omega}, \tag{2.1}$$

where

$$\omega_{\mathrm{p}} = \sqrt{\frac{\mathrm{N}e^2}{\epsilon_\circ \mathrm{m}_\circ}}, \tag{2.2}$$

is the 'plasma frequency' of the free electron oscillation, ω is the frequency of the incident electromagnetic radiation, γ is the collision frequency of the motion of the free electrons, N is the number of electrons per unit volume, e and $\mathrm{m}_\circ$ are the charge and effective mass of the electron, respectively, and $\epsilon_\circ$ is the permittivity of free space. The real and imaginary parts of the complex dielectric function of gold [31], used in the calculations presented in this thesis, are shown in Fig. 2.2. For

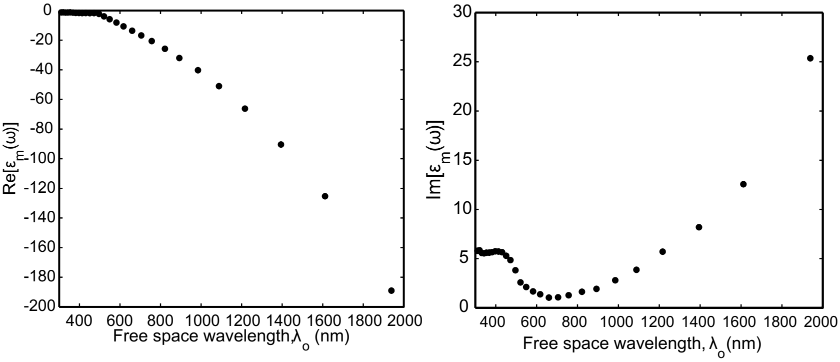

Figure 2.2: The real (left) and imaginary (right) part of $\epsilon_m(\omega)$ for gold determined by Johnson and Christy [31].

a lightly damped system, $\gamma \ll \omega$ and Eq. (2.1) reduces to

$$\epsilon_m(\omega) = 1 - \frac{\omega_p^2}{\omega^2}. \tag{2.3}$$

For low frequencies where ω is below the plasma frequency ω_p, $\epsilon_m(\omega)$ is real and negative or, in other words, the refractive index $n' = \sqrt{\epsilon_m}$ is imaginary.

An electromagnetic wave propagating through a medium with an imaginary refractive index decays exponentially in the medium [26]. Applying Maxwell's boundary conditions for an interface separating a metal and a dielectric, we get the SPP wave on the interface with evanescent confinement in both media [28]. The simplest geometry sustaining SPPs is that of a flat interface between a metal with a negative real dielectric function and a dielectric with a positive real dielectric function.

2.3 Properties of SPPs

The electromagnetic field associated with SPPs on a metal-dielectric interface can be described [32] by

$$E = E_o^{\pm} e^{i(k_\parallel x \pm k_\perp z - \omega t)}, \tag{2.4}$$

with the plus sign for $z \geq 0$ and the minus sign for $z \leq 0$, as shown in Fig. 2.1b. Here $k_\perp$ and $k_\parallel$ are the components of the incident wave vector (or propagation constant) perpendicular and parallel to the interface, respectively. $k_\perp$ and $k_\parallel$ are obtained by solving the Maxwell's equations for the interface [32] and are given by

$$k_{\perp i} = \sqrt{[\epsilon_i(\omega/c)^2 - k_\parallel^2]},\ i = m(\text{metal}), d(\text{dielectric}), \tag{2.5}$$

and

$$k_\parallel = k_i \sin\theta, \tag{2.6}$$

where c is the speed of light in vacuum, θ is the angle of incidence and k_i is the wave vector of the incident light in the dielectric. $k_\parallel$ is real and continuous through the interface and $k_{\perp m}$ is imaginary due to the fact that $k_{\parallel} > \frac{\omega}{c}$ and $\mathrm{Re}[\epsilon_m(\omega)] < 0$, which causes the SPP field amplitude to decrease exponentially as $e^{(-|k_{\perp i}||z|)}$, perpendicular to the interface, as illustrated in Fig. 2.3a. This property of SPPs leads to the field confinement on the interface. The spatial extension of the SPP field in the dielectric is higher than that in the metal because $\epsilon_d < |\, \mathrm{Re}[\epsilon_m(\omega)]\, |$. The SPP field is parallel (or p-) polarized, where the electric field vector lies in the plane containing the SPP wave vector k_{spp} .

The dispersion relation of SPPs propagating at the interface of an ideal metal ($\mathrm{Im}[\epsilon_m(\omega)] = 0$) and a dielectric is given by

$$k_{spp} = \frac{\omega}{c}\sqrt{\frac{\epsilon_m(\omega)\epsilon_d}{\epsilon_m(\omega)+\epsilon_d}}, \tag{2.7}$$

and is plotted in the dispersion graph shown in Fig. 2.3b, which shows that the momentum of the SPP wave is higher than the free-space light momentum, for $\omega < \omega_p$.

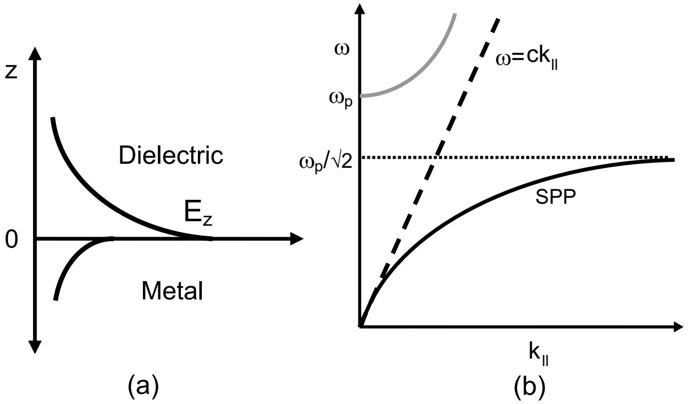

Figure 2.3: Schematic representation of (a) the exponential dependance of the field E_z and (b) the dispersion relation of SPPs at a metal-dielectric interface with negligible collision frequency. The black solid line is the SPP dispersion, the dashed line is the light line in air, and the gray curve denotes the dispersion of the radiative mode into the metal.

The graph is divided into two regions with respect to the light line $\omega = ck_{\parallel}$ in air: the one that supports bound (or non-radiative) modes which are to the right of the light line, and the other that supports radiative modes located to the left of the light line. For frequencies $\omega < \omega_p$, SPPs are non-radiative and confined to the metal-dielectric interface so that its dispersion curve lies to the right of the light line. Radiation into the metal occurs in the transparency regime for $\omega > \omega_p$. A gap in the frequency region is seen in between the non-radiative and the radiative regimes that prohibit propagation since k_{spp} is purely imaginary in that region.

2.4 Optical excitation of SPPs on a planar metal surface

Surface Plasmon Polaritons can be excited on a metal surface, either fast moving electrons or photons, when the in-plane wave vector component, $k_{\|}$, of the excitation beam matches the SPP wave vector k_{spp}. The high energy electrons penetrate the metal film, scatter in different directions, and transfer their momenta to SPPs [32]. To optically excite SPPs, special phase-matching techniques are required to shift the line light to intersect with the SPP dispersion curve, because k_{spp} is higher than $k_{\|}$, as is evident from Fig. 2.3b. The three widely used techniques to optically excite SPPs are prism coupling, grating coupling, and a sub-wavelength scatterer. The first two are investigated in this thesis. The sub-wavelength scatterer can either be located on the metal surface or be a nano-sized aperture of an optical fiber [33].

2.4.1 Prism coupling

A major advance in the study of SPPs was made in 1968, when Otto, Kretschmann, and Raether presented methods for the optical excitation of SPPs on planar metal films. Total internal reflection of light traveling from an optically denser to a rarer medium, for example from a glass prism to air, generates evanescent waves in the rarer medium [1]. The evanescent waves advance parallel to the interface with a wavelength component given by

$$\lambda_{\|} = \frac{2\pi}{k_{\|}}. \tag{2.8}$$

By placing an absorbing medium, such as a metal layer, in close proximity to the reflecting face of the prism, the reflection can be reduced or attenuated which is called Attenuated Total Reflection (ATR) [2]. ATR is a "lossy coupling" method since the intensity of the incident light decreases exponentially in the metal layer.

A contact between the metal surface and the reflecting face of the prism is not a necessary condition to obtain ATR. Depending on the location of the metal surface, two different ATR configurations are possible: an Otto configuration [34] and a Kretschmann-Raether configuration [4]. Schematics of the two configurations are shown in Fig. 2.4. In the Otto configuration, the metal surface is separated from the reflecting face of the prism by a dielectric of refractive index lower than that of the prism. The evanescent field generated by total internal reflection at the metal-dielectric interface couples to SPPs on the metal surface facing the dielectric spacer layer. This method is suited for applications where the metal layer is a few hundreds of micron thick.

In the Kretschmann-Raether configuration, a metal film with a thickness of several tens of nanometers is coated on top of the prism. The incident light illuminates the metal film through the prism. The exponentially decaying incident electromagnetic field couples to SPPs on the metal surface facing the rarer medium. The wave vector of the SPPs at the metal-prism interface is higher than that of light inside the prism and hence the Kretschmann-Raether configuration does not

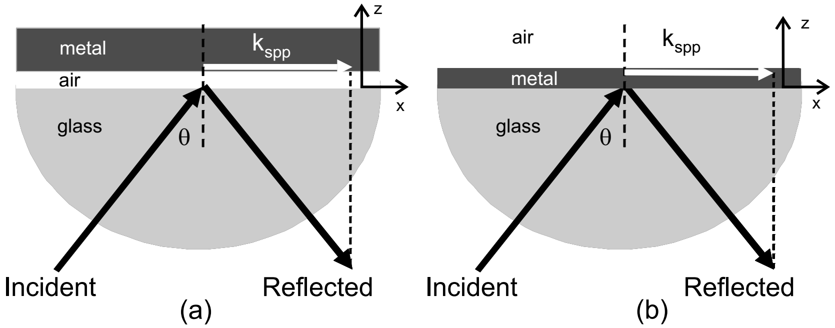

Figure 2.4: Schematic showing the excitation of SPPs in (a) an Otto configuration and (b) a Kretschmann-Raether configuration.

couple to SPPs at the metal-prism interface. In Surface Plasmon Resonance (SPR) sensors, Kretschmann-Raether configuration is the most commonly used coupling scheme due to the relatively simple optical system involved. A Kretschmann-Raether configuration is also easy to integrate into a near-field optical microscope for imaging SPPs, which will be discussed in Chapter 3.

Prism-coupled SPPs [13, 35, 36] are leaky waves that re-radiate light back to the prism. Equation (2.5) implies that $k_\perp$ is imaginary in the metal and real in the prism. This causes the re-radiated light to propagate in the glass prism, which destructively interferes with the specularly reflected beam to form a minimum in the specular reflection. The SPPs are 180° out of phase with the incident light. When the SPPs radiate light back to the prism, an additional 180° phase change occurs for the reradiated light and hence the reradiated light becomes in-phase with the incident light or out of phase with the specular reflected light. This explains the destructive interference between the re-radiated and the specularly reflected light.

A quantitative description of the prism-coupled SPPs is given in Ref. [32], using the Fresnel equations for a three layer (glass/gold/air) system. A schematic diagram of the glass/gold/air system with the Fresnel coefficients is shown in Fig. 2.5a. For p-polarized illumination, the Fresnel reflection and transmission coefficients are given by

$$r_{p123} = \frac{r_{p12} + r_{p23} e^{(2ik_{\perp 2} d)}}{1 + r_{p12} r_{p23} e^{(2ik_{\perp 2} d)}}, \tag{2.9}$$

and

$$t_{p123} = \frac{t_{p12} + t_{p23} e^{(ik_{\perp 2} d)}}{1 + r_{p12} r_{p23} e^{(2ik_{\perp 2} d)}}, \tag{2.10}$$

where

$$r_{pij} = \frac{n_j^2 k_{\perp i} - n_i^2 k_{\perp j}}{n_j^2 k_{\perp i} + n_i^2 k_{\perp j}}, \tag{2.11}$$

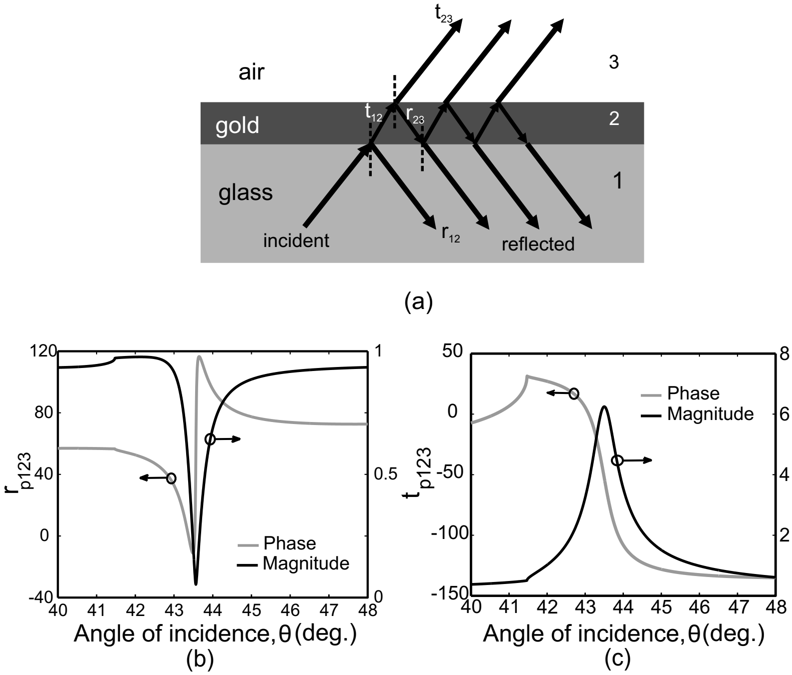

Figure 2.5: (a) Schematic diagram of a three layer system with the Fresnel reflection and transmission coefficients. The magnitude (black) and the phase (grey) of the Fresnel (b) reflection (r_{p123}) and (c) transmission (t_{p123}) coefficients, respectively, for a 50 nm thick gold layer.

and

$$t_{pij} = r_{pij} + 1, \tag{2.12}$$

are the Fresnel reflection and transmission coefficients, respectively, for a two layer system, $k_{\perp i}$ is the perpendicular component of the incident wave vector as given in Eq. (2.5), i and j can take values 1, 2, and 3 denoting the three different layers, and d is the thickness of the gold layer.

The magnitude and phase of the Fresnel reflection and transmission coefficients are shown in Fig. 2.5b and 2.5c, respectively, for a 50 nm thick gold layer. The dielectric function of the gold is $\epsilon_2 = -13.7 + i1.04$, taken from Ref. [31], for a free space wavelength of 632.8 nm. A dip in the magnitude of the reflection coefficient denotes the resonant excitation of SPPs at the gold-air interface. The minimum of the reflection coefficient coincides with the maximum of the transmission coefficient [32]. The sharp phase shift at the resonant excitation of SPPs has found application in SPR sensors [22, 23, 24]. The extraction of the phase shift at SPR using two different approaches will be discussed in Chapter 4.

For a smooth metal surface, the depth and the width of the reflection minimum depend on the thickness d of the metal layer. For p-polarized incident light, the magnitude of the Fresnel reflection and transmission coefficients as a function of the incident angle, for different thicknesses of the gold layer are depicted in Fig. 2.6a and 2.6b, respectively. Depending on the thickness of the metal layer, three different coupling regimes [10, 32] are possible:

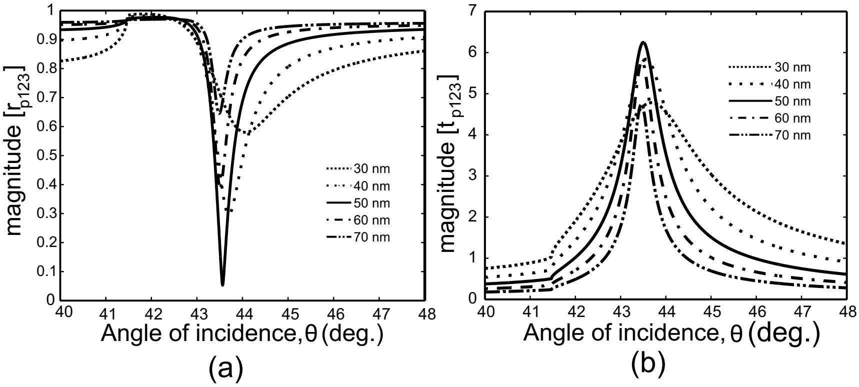

Figure 2.6: Angular dependance of Fresnel reflection and transmission coefficients r_{p123} and t_{p123}, respectively, calculated by using Eq. (2.9) and (2.10), for a gold layer with varying thicknesses.

Case 1: Under-coupling
When the metal layer is thick (d>50 nm), the re-radiated light disappears and the magnitude of the Fresnel reflection coefficient increases.

Case 2: Optimum coupling
An optimum coupling is achieved when the re-radiated light is equal to the light absorbed by the metal film. The thickness of gold layer required for an optimum coupling is 50 nm for a free space wavelength of 632.8 nm.

Case 3: Over-coupling
When the metal layer is thin (d<50 nm), the re-radiated light increases. Again the reflection minimum does not go to zero.

2.4.2 Grating coupling

A second SPP coupling mechanism is by using a diffraction grating. Patterning a metal surface with a periodic array of lines or holes increases or decreases the wave vector of the incident light by an integer multiple of the grating wave vector. The phase matching condition for the excitation of SPPs via a grating is given by

$$k_{spp} = k_{\parallel} \pm m k_g, \tag{2.13}$$

where m is the order of diffraction. The grating wave vector $k_g = \frac{2\pi}{\Lambda_g}$, where Λ_g is the period of the grating. A schematic of the grating coupling scheme is shown in Fig. 2.7.

Grating-coupled SPPs [37, 38] have yielded a wide range of optical phenomena such as cross-coupling between SPPs generated on both sides of the grating [39, 40],

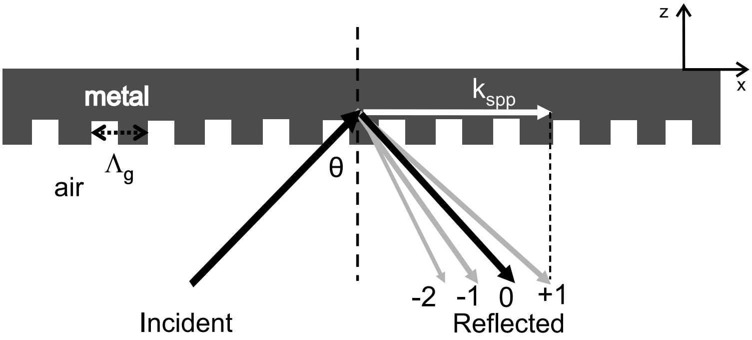

Figure 2.7: Schematic of the grating coupling scheme. The phase matching condition to excite SPPs in this particular case is $k_{spp} = k_{\|} + k_g$

energy gap formation in the propagation of SPPs due to the interference of SPPs on the grating [9], high resolution surface pattering using surface plasmon interference [41], and focusing SPPs by non-collinear phase matching using designer gratings [8]. In addition, a grating milled on the shaft of a sharp metal taper has been shown to couple light to SPPs that propagate to the tip apex of few tens of nanometers to form a nanoconfined light source [42].

2.5 Attenuation of SPPs

SPPs generated on a metal surface propagate along the surface. However, they gradually decay due to the attenuation inherent to the metal. The attenuation (or damping) of SPPs can be classified into two types: internal damping and radiation damping.

Internal damping
For a smooth metal surface, the attenuation of SPPs is mainly due to the absorption of the SPP field into the metal, which is called internal damping [32]. The intensity of SPPs propagating along the metal surface decreases as $e^{(-2\mathrm{Im}[k_{spp}]x)}$, which defines the 'propagation length' of SPPs as the length after which the intensity of SPPs decreases to 1/e, given by

$$L_{spp} = \frac{1}{2\mathrm{Im}[k_{spp}]}. \tag{2.14}$$

Using $\epsilon_m(\omega)$ for a gold layer of thickness 50 nm, taken from Johnson and Christy [31], the dependance of the SPP propagation length on the free space wavelength $\lambda_\circ$, for SPPs excited at the gold-air interface, is shown in Fig. 2.8. The propagation length of the SPPs increases with the free space wavelength of the incident electromagnetic radiation. For example, the SPP propagation length for silver is equal to 20 µm and 1 mm at $\lambda_\circ$ equal to 500 nm and 1500 nm, respectively [43].

Radiation damping
The coupling of photons to SPPs is a reversible process. The decoupling process

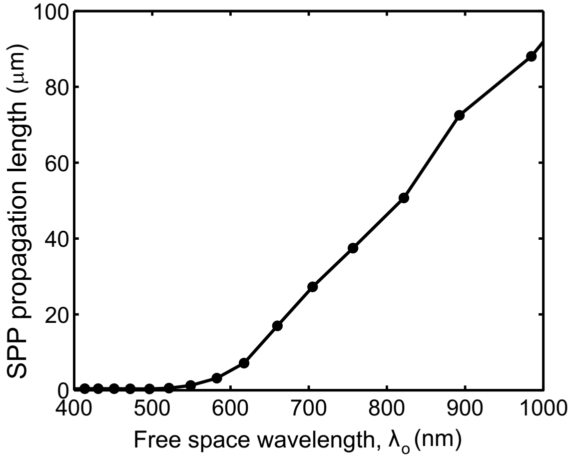

Figure 2.8: Propagation length of SPPs excited on a flat gold-air interface computed using the real and imaginary values of $\epsilon_m(\omega)$ [31] as a function of the free space wavelength λ_o of the incident electromagnetic radiation. Here it is assumed that the SPPs are not subjected to radiation losses.

is called Radiation damping. For a metal surface that is rough or periodically corrugated, there are two processes that can contribute to the radiative damping: the coupling of SPPs to radiation into the air space and the scattering of SPPs into other SPPs propagating in different direction without any change in the absolute value of the SPP wave vector. The former is discussed in the context of SPR sensors in Chapter 5.

SPPs propagating on a grating surface can reduce their momenta, by the grating wave vector k_g, radiating light into the air space [36, 44, 45]. The light, emitted via the roughness or the periodic surface corrugation, interferes with the reflected or transmitted part of the incident light [46]. The phase of the reradiated light with respect to the phase of the reflected or transmitted part of the excitation light determines the shape of the SPP resonance.

The propagation length of SPPs can be increased by modifying the Kretschmann-Raether configuration. The Kretschmann-Raether configuration is an asymmetric two-interface system, and hence the k_{spp} values at the two-interfaces are different and cannot couple with each other. However, for a symmetric two interface system, when the thickness d of the metal film is small enough ($k_{\perp m}d \ll 1$), the SPPs at the two interfaces interact with each other and the SPP dispersion curve splits into a higher and a lower frequency [32]. The SPPs associated with the higher frequency exhibit a longer propagation length which increases with decreasing d. They are called long-range SPPs [47]. In addition to the spatial decay of SPPs, there exists a temporal decay [32] of the SPPs that can be detected using a time-resolved optical pump-probe technique [48].

2.6 Detection of SPPs

Since SPPs are confined to the surface where they are generated, their direct detection is possible by frustrating and converting them back to a radiation. Detection techniques that perturb the field associated with the SPPs are near-field imaging, scattered light imaging, and fluorescence imaging.

A Photon Scanning Tunneling Microscope (PSTM) [49] has been used to visualize SPPs with sub-wavelength resolution [10, 13, 50], which will be discussed in Chapter 3. The SPP field can also be scattered by isolated surface irregularity [51] which gives a measure of the SPP propagation length on a metal surface [52]. Another way to detect SPPs is by coating a metal surface by emitters such as fluorescent molecules or quantum dots that can be excited by SPPs [53]. A Photoacoustic detection method can be used to measure the non-radiative dissipation of energy contained in the SPPs by probing the heat generated in the metal [54]. SPPs can also be detected by decoupling scheme such as the statistical or periodic roughness of the surface [55].

The conventional method to infer the presence of SPPs is by measuring the light reflected off a metal surface as shown in Fig. 2.9a. A 15 × 15 × 0.3 mm glass coverslip was sputter coated with a 50 nm thick gold layer (Ssens) and placed on top of a glass (BK7) hemispherical prism with index matching oil in between to form a Kretschmann-Raether configuration. A sheet polarizer (P) was used to choose the polarization state of the incident light. A fiber collimator illuminates (free-space wavelength of 632.8 nm) the sample and was mounted on a goniometric stage for angles ranging from 40° to 50.8°. The incident angles were calibrated by measuring the transmission angles without the hemispherical prism. A refraction of the beam after inserting the prism can cause a change in the incident angle from the set values. The divergence of the beam introduces a smearing in the incident angle of about 1°. The incident angle θ was chosen such that the light undergoes total internal reflection for a glass-air interface. A photodiode detects the light reflected off the metal film. A reflection measurement as a function of the incident angle is

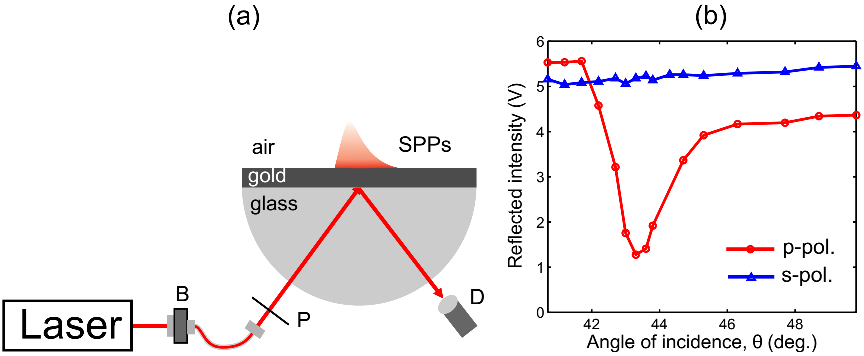

Figure 2.9: (a) The experimental set up to infer the excitation of SPPs where P is a polarizer, D is a photodiode, and B is an objective. (b) The intensity of light reflected off a 50 nm thick gold film for p- and s-polarized incident light as a function of the incident angle.

shown in Fig. 2.9b. The p-polarized incident light excites SPPs on the gold-air interface at an incident angle of 43.8°. The minimum in the reflection curve does not go to zero which is attributed to a difference in the amount of radiative damping when compared to that of the internal damping in the metal [56]. For s- (or perpendicular) polarized illumination a flat reflection curve is obtained since the incident light cannot couple to SPPs.

The leaky SPPs have also been used to visualize the SPPs propagating away from a highly focused excitation spot [57] as well as to image the SPP dispersion in the reciprocal space [58] using a technique called leakage radiation imaging. SPPs are excited by illuminating the metal film through a glass prism using a highly focused optical beam. The incident beam provides a range of in-plane wave vectors including those that satisfy the phase matching condition. The leakage radiation collected at the prism side shows the SPPs propagating away from the excitation spot.

2.7 Applications

Applications of SPPs vary from health [59] to sensing [5], from optical data storage [60] to optical waveguiding [16], and from surface lithography [41] to solar cells [61]. The most widely known application of SPPs is sensing of chemical and biological molecules and real-time monitoring of bio-molecular interactions [62] on a metal surface, where a change in the refractive index of the surrounding medium shifts the minimum in the reflection spectrum. Recently, a microfabricated silicon SPR sensor combining a Si prism and an optical grating has been developed for near-IR wavelengths [63] that might act as a miniaturized one-chip SPR sensor for point-of-care use.

Applications of the localized surface plasmon resonance include surface enhanced raman scattering [64] for ultrasensitive biomolecular detection [65], cancer diagnosis [66] and nanoshell-mediated cancer therapy [67, 68]. The recent development in nanolithographic tools has enabled surface patterning to nanometer dimensions to manipulate the propagation of SPPs [8, 9, 69]. SPPs have also been used to synthesize hybrid nanoparticles with varying size and shape in a controlled way [70]. Increasing the optical absorption in the active medium of a thin film solar cell using SPPs is another promising area [61].

In addition to manipulating SPPs by texturing a metal surface, Zhang and coworkers have shown patterning a metal surface using multiple SPPs interfering with each other, a technique called surface plasmon interference nanolithography [41]. The SPP mediated extraordinary transmission through sub-wavelength hole arrays observed by Ebbesen and colleagues in 1989 [71] has recently been investigated in the mid-IR region of the electromagnetic spectrum to act as an optical filter by changing the lattice constant and the dielectric medium bounding the hole arrays [72].

3

Photon scanning tunneling microscopy

3.1 Introduction

The generation of evanescent waves by total internal reflection paved the way for the development of internal reflection microscopy with applications such as fingerprinting, sensors and the measurement of thicknesses and refractive indices of thin films [2]. The transition from propagating waves to evanescent waves marks the lower limit on the size of an object that can be imaged using a conventional lens-based optical microscope. When the width of the object is smaller than half the wavelength λ of the illuminating light, a large part of its angular spectrum becomes evanescent and hence cannot be resolved in the far-field [73].

3.2 Near-field Scanning Optical Microscopy (NSOM)

In 1928, more than two centuries after Newton's demonstration of the existence of evanescent waves, Synge put forward a concept to beat the resolution limit in optical microscopy [74]. He proposed a miniature aperture, of approximately 10 nm diameter, in a flat screen and moving it with great precision at a few nanometers away from the object to be imaged. The resolution in this case is limited by the diameter of the aperture and the distance between the aperture and the object.

His concept developed over the years into a new form of optical microscopy called Near-field Scanning Optical Microscopy (NSOM). An NSOM consists of a submicron aperture on an optical fiber, tapered down to around 50 nm, called a 'probe'. The probe is brought close to the surface of the object. A two-dimensional image of the surface can be obtained by raster scanning the probe over the surface while keeping the object stationary, or vice versa.

The first near-field scanning microscope was realized by Ash and Nicholls in 1972, which was operated at microwave frequencies [75]. In 1984, optical super-resolution instruments were proposed [76] and a resolution down to $\lambda/20$ was achieved [77]. In 1989, Reddick demonstrated NSOM as a tool to investigate light-matter interactions at the nanoscale [49]. In the same year, Fischer developed a single particle plasmon near-field microscope [78].

3.2.1 Aperture-less and aperture NSOM

The basic principle of NSOM is the perturbation of the evanescent waves due to the interaction between the probe and the sample surface. Depending on the type of the probe used to perturb the evanescent waves, NSOM can be classified into aperture-less and aperture. A schematic of the NSOM configurations [79] is shown in Fig. 3.1.

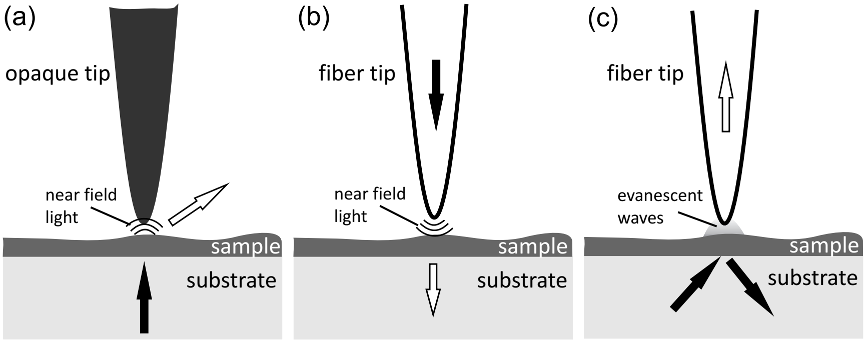

Figure 3.1: NSOM configurations: (a) an aperture-less NSOM, and (b) and (c) aperture NSOM in illumination and collection modes, respectively. The filled and open arrows indicate the illumination light and the detection light, respectively.

Aperture-less NSOM

Aperture-less NSOM uses either a sharp metallic probe or a fluorescent molecule attached to the apex of the probe as the near-field scatterer. The probe locally perturbs the near-field on the sample surface. Upon vibrating the probe, the scattered light can be detected in the far-field [80] as shown in Fig. 3.1a. A dielectric cantilever probe has recently been demonstrated to map the complex field of infrared nanoantennas by interferometric detection [81]. Fluorescence quenching in molecules by positioning a metallic probe close to the molecules forms another type of NSOM [82]. Similar to the surface-enhanced raman scattering mentioned in Chapter 2, the coupling to Surface Plasmon Polaritons (SPPs) on the apex of a metallic probe can give rise to local field enhancement, which is referred to as tip-enhanced raman scattering. It has been used to image nanostructures with a spatial resolution better than 30 nm [83].

Aperture NSOM

Aperture NSOM uses a tapered optical fiber probe (referred to as a 'tip') as the near-field scatterer. The two most commonly used methods to make the tip are chemical etching [84] and a thermal-mechanical process [85]. The chemical etching process involves immersing the extremity of a cleaved fiber into a buffered solution of hydrofluoric acid to make a sharp taper at the end of the fiber. In the thermal mechanical process, a fiber of typically 125 µm diameter is melted and pulled to get an apex diameter of approximately 75 nm. To reduce the coupling of stray light into the dielectric tip, it can be coated with a thin layer of metal (usually aluminium). The apex of the metal-coated fiber is cut perpendicular to the optical axis of the fiber using a Focused Ion Beam (FIB) to create an aperture. The results presented in this thesis were obtained using metal-coated dielectric tips. A Scanning Electron Microscope (SEM) image of a typical metal-coated dielectric tip is shown in Fig. 3.2.

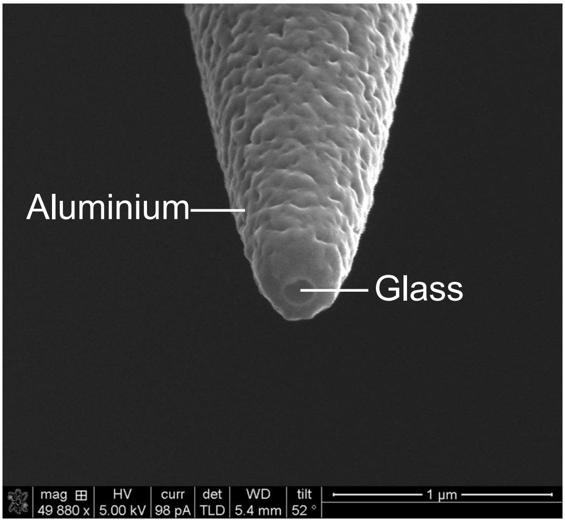

Figure 3.2: Scanning Electron Microscope image of a metal-coated dielectric tip with an aperture diameter of 130 nm. The metallic coatings are 4 nm chromium (hardly visible) as an adhesion layer followed by 200 nm aluminium.

The tip can act either as an emitter or as a collector. Hence the operation mode of the aperture NSOM can be divided into two: illumination-mode and collection-mode. In illumination-mode (Fig. 3.1b), the sample is illuminated by the tip. The light from the sub-micron aperture of the tip is largely evanescent. When the tip-to-sample distance is of the order of half the illumination wavelength, the evanescent waves are converted into propagating waves and collected either by the tip or by an objective lens placed on the transmission side of the sample. Decreasing the aperture diameter of the tip improves the optical resolution of the NSOM, but reduces the throughput of the tip [86]. A collection-mode NSOM, or a Photon Scanning Tunneling Microscope (PSTM) is shown in Fig. 3.1c. Evanescent waves generated on the sample surface are perturbed and propagate into the tip. The principle and applications of the PSTM are discussed in the rest of this chapter.

3.3 Photon Scanning Tunneling Microscope (PSTM)

A PSTM [49, 78, 87] can be considered as the optical analogue of a Scanning Tunneling Microscope (STM) [88]. The metallic tip used in the STM conducts charge, whereas the PSTM uses a tapered optical fiber to conduct photons. The STM requires electrically conductive samples and the PSTM requires optically transparent samples. The operating principle of PSTM is the frustration of the evanescent waves by the tip, to be detected in the far-field. The evanescent waves are generated using several methods such as total internal reflection, diffraction by a subwavelength grating, diffraction by a small aperture and diffraction in a waveguide.

3.3.1 Total internal reflection

The easiest way to generate evanescent waves is total internal reflection. For two media with refractive indices n_1 and n_2 such that $n_1 > n_2$, Snell's law gives

$$n_1 \sin\theta_1 = n_2 \sin\theta_2, \tag{3.1}$$

where θ_1 and θ_2 are the angles of incidence and refraction, respectively. The incident angle at which the refracted light grazes the interface separating the two media is called the *critical angle* θ_c given by

$$\theta_c = \sin^{-1}(\frac{n_2}{n_1}). \tag{3.2}$$

When $\theta_1 > \theta_c$, all the light energy is reflected back into the denser medium. This phenomenon is called *total internal reflection* and is depicted in Fig. 3.3a. If light propagates from glass with an index of refraction of 1.51 to air with the index of refraction of 1, the critical angle is 42.5°.

The solution of Maxwell's equations at the interface implies that the tangential component of the wave vector in the two media must be continuous across the boundary, given by

$$k_1 \sin\theta_1 = k_2 \sin\theta_2, \tag{3.3}$$

where k_1 and k_2 are the incident and transmitted wave vectors, respectively. Since $\theta_2 = 90°$ at total internal reflection, we have $k_1 \sin\theta_1 = k_2$. There exists a wave in the rarer medium with wave vector $k_{\parallel}$ given by

$$k_{\parallel} = k_2 = k_1 \sin\theta_1. \tag{3.4}$$

The perpendicular component of the wave vector in the denser medium is given by

$$k_{\perp} = \sqrt{k_1^2 - k_{\parallel}^2}. \tag{3.5}$$

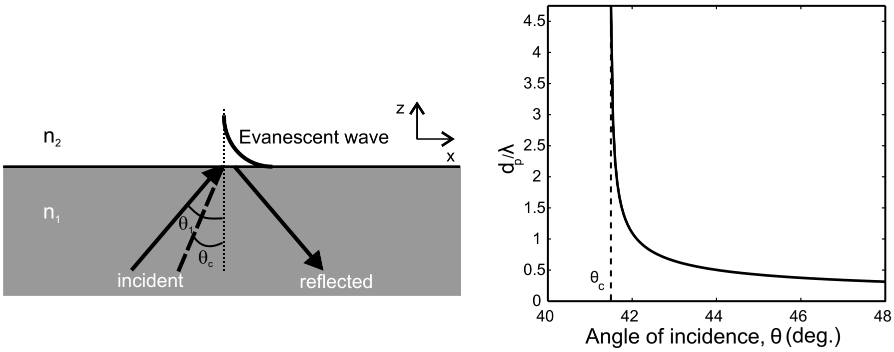

(a) (b)

Figure 3.3: (a) Total internal reflection of light at a boundary separating two media with refractive indices n_1 and n_2 such that $n_1 > n_2$. The evanescent wave is shown as an exponentially decaying wave in the rarer medium. (b) The ratio of the penetration depth d_p to the illumination wavelength λ in air as a function of the incident angle θ for a glass-air system.

Since k_1 is smaller than $k_\parallel$ in the rarer medium, $k_\perp$ becomes imaginary. On the $y = 0$ plane, the solution to Maxwell's equations is

$$E(x, z) = E_0 e^{(ik_\parallel x)} e^{(-z/d_p)}, \tag{3.6}$$

where $E_0 e^{(ik_\parallel x)}$ is the complex amplitude of the transmitted field. Equation (3.6) describes a wave advancing parallel to the interface (in the x direction) with its amplitude decaying exponentially away from the interface (in the z direction). Due to its vanishing nature away from the interface, this wave is called an *evanescent wave*. One property of the evanescent wave is that the surfaces of constant amplitude (parallel to the plane of the interface) are perpendicular to the surfaces of constant phase (normal to the plane of the interface). Since they do not coincide, the surface wave is inhomogeneous [89].

The distance perpendicular to the interface in the rarer medium at which the amplitude of the evanescent wave decreases to 1/e of its value on the interface is called the penetration depth d_p of the evanescent wave and is given by

$$d_p = \frac{\lambda}{2\pi\sqrt{(n_1 \sin\theta_1)^2 - n_2^2}}. \tag{3.7}$$

The value of d_p depends on the refractive indices of the two media, the illumination wavelength, and the incident angle [90]. The maximum penetration depth occurs at the critical angle and thereafter it decreases with the incident angle. The ratio $\frac{d_p}{\lambda}$ as a function of the incident angle, for an interface with $\frac{n_1}{n_2}$ equal to 1.51 (glass-air system) is shown in Fig. 3.3b.

The existence of evanescent waves in the rarer medium causes another interesting effect: the reflected beam undergoes a lateral displacement from its reflected position described by geometrical optics (Fig. 4.1 in Chapter 4). The lateral beam displacement has been experimentally verified in 1947 by Goos and Hänchen and the phenomenon is known as the “Goos-Hänchen effect” [18]. The combined spatial phase shift of the evanescent waves associated with the Goos-Hänchen effect and the surface plasmon resonance effect will be investigated in Chapter 4.

3.3.2 Frustrated Total Internal Reflection (FTIR)

In total internal reflection, there is no net energy flow through the boundary into the rarer medium [89]. However, when a third medium with a refractive index equal to or higher than that of the first medium is brought into the evanescent wave region, the incident light starts to couple into the third medium. The coupling from evanescent waves can be achieved using two processes: Attenuated Total Reflection (ATR) for absorptive materials (discussed in Chapter 2) and Frustrated Total Internal Reflection (FTIR)[1] for optically transparent samples. Unlike the ‘lossy coupling’ in the ATR, FTIR is a ‘lossless coupling’ scheme where there is redirection of energy without attenuation [2].

FTIR was first observed by Newton in the 17th century [1] and his experimental scheme is demonstrated in Fig. 3.4. In the experiment, the reflecting face of a prism is placed against a lens with a large radius of curvature. Incident light undergoes total internal reflection and produces a dark spot in the reflection and a bright spot in the transmission. An interesting observation was that the luminous area in the transmission was larger than the point of contact of the prism and the lens. Evanescent waves generated at the reflecting face of the prism, untouched but still close to the surface of the lens, are converted into waves transmitting through the lens leading to a bigger bright spot in transmission [79].

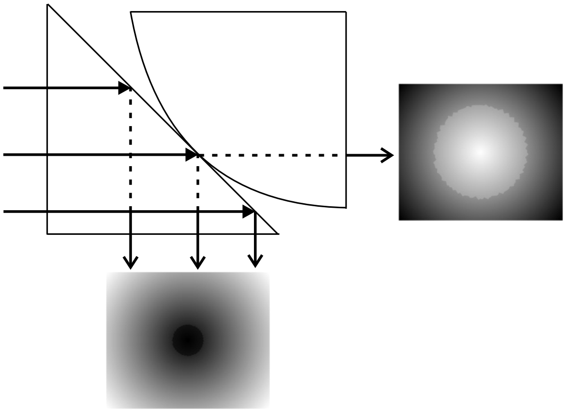

Figure 3.4: Pictorial representation of Newton’s experiment to demonstrate frustrated total internal reflection.

Instead of the lens in the Newton’s experiment, PSTM uses a tapered optical fiber to frustrate the evanescent waves. Upon introducing the fiber tip into the eva-

---

[1] Not to be confused with Fourier transform infrared spectroscopy

nescent wave region, FTIR occurs and the evanescent waves propagate into the fiber [91]. A schematic of FTIR using an optical fiber tip is shown in Fig. 3.5.

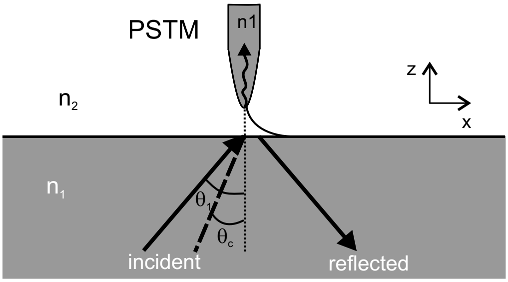

Figure 3.5: Principle of the PSTM: frustration of the evanescent waves by a tapered optical fiber tip.

3.4 Operating modes of PSTM

Imaging using PSTM is done by raster scanning the tip on the sample surface. To precisely control the tip-to-sample distance, a feedback mechanism is used. The PSTM can be operated in three different modes: constant intensity, constant height and constant distance. The three different modes of operations are schematically shown in Fig. 3.6.

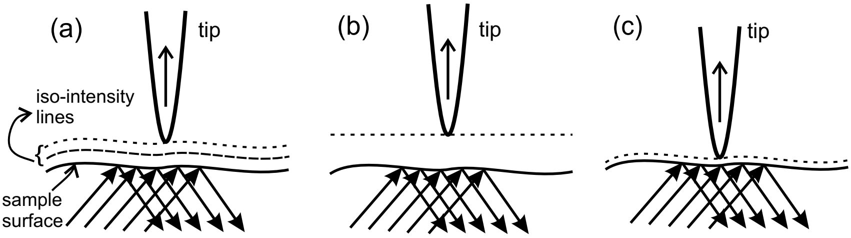

Figure 3.6: Operating modes of PSTM: (a) constant intensity mode, (b) constant height mode, and (c) constant distance mode.

In the constant intensity mode (Fig. 3.6a), the tip-to-sample distance is adjusted such that the intensity of light collected by the tip is maintained at a constant value throughout the scan [92]. The resulting feedback signal will resemble the height profile of the sample surface. The constant intensity mode is not suitable when the intensity near the surface varies [79], for instance, caused by a surface plasmon resonance. However, by using two different laser wavelengths with varying spot sizes such that one laser is used to excite SPPs and the other laser is used for feedback purposes, one can image the lateral propagation of the SPPs [10]. In constant height mode (Fig. 3.6b), the tip is scanned at a fixed distance from the average plane of the sample. The PSTM image shows variations of the optical signal picked up by the tip in accordance with the sample topography [91, 93]. A Constant distance mode [8, 49] (Fig. 3.6c) is the most widely used operating mode of the PSTM, where the relative distance between the tip and the sample is kept constant by using the shear forces acting on the tip [94], or by measuring the tunneling current [95] in the case of conductive samples. The former is generally termed as a shear force feedback mechanism.

3.5 Shear force feedback

A shear force feedback was first proposed by Betzig [96]. The tip is glued along the sides of one of the prongs of a quartz crystal tuning fork (32.768 Hz). The tuning fork is attached to a piezoelectric material and mechanically dithered at its resonance frequency by a dithering piezo-element [94]. The amplitude and the phase of the tuning fork signal can be detected. When the tip nearly touches the surface of the sample, the amplitude of the tuning fork signal is reduced and the phase shifts due to shear forces acting on the tip. The tuning fork signal is used as a feedback signal to position the tip at a constant distance of less than 20 nm above the sample surface using a piezoelectric scanner [84, 97]. The tuning fork feedback signal fed to the piezoelectric material encodes information about the height of the sample. In addition, two more piezos, one each for the lateral (or in-plane) movements of the tip, controlled with a position sensor, provide imaging in the plane of the sample. Thus a PSTM operated with a shear force feedback mechanism provides both optical and two-dimensional topographic (height) information of the sample.

3.6 Applications of PSTM

In the early nineties, PSTM was mainly used to image surfaces with sub-wavelength optical resolution [49, 90, 92]. Probing the evanescent waves generated on the surfaces revealed the sub-wavelength features on the surface. A more advanced application of the PSTM is to investigate the behavior of light at the nanoscale. In 1994, Dawson and coworkers used a PSTM to image, in real space, the propagation length of SPPs on a thin silver film [12]. PSTM has also been used to observe coupling of light into an optical waveguide of sub-wavelength cross section [91, 98], optical modes of silver colloid fractal structures [99] and transverse confinement of SPPs propagating on a thin metal strip [13].

3.6.1 Intensity distribution on an integrated waveguide

In this section, the PSTM is demonstrated as an imaging tool to detect the intensity of light exiting the end face of an integrated optical waveguide. A schematic of the setup is shown in Fig. 3.7a. The sample under investigation is an integrated optical waveguide written in fused silica using a femtosecond laser [100]. The PSTM is operated in constant distance mode using the shear force feedback mechanism. Unlike the total internal reflection arrangement, the PSTM is configured in such a way that the light emerging from the optical waveguide illuminated the tip head-on.

Light (free space wavelength of 632.8 nm) was coupled into the optical waveguide using an objective lens. The tip was raster scanned over the end face of the optical waveguide. A Photo Multiplier Tube (PMT) was used to detect the light collected by the tip. The output from the PMT is proportional to the intensity on the end face of the waveguide [101]. The measured topography and the optical intensity are shown in Fig. 3.7b and 3.7c, respectively. A line trace taken along the white dashed line in the topography image is shown in Fig. 3.7d. A height variation of approximately 120 nm is measured which is attributed to the rough fused silica surface. The bonding edge in the chip is seen as the relatively dark-colored region in the topography, with a height difference of approximately 263 nm. The optical intensity image shows a radially-symmetric pattern. A corresponding line trace in the intensity image, depicted in Fig. 3.7e, shows a lorentzian beam profile [2].

3.6.2 Heterodyne interferometric PSTM

A conventional PSTM yields the intensity of the optical field on the sample surface. A complete description of the optical field requires the measurement of amplitude, phase and polarization. The amplitude and phase of the evanescent waves on a sample surface can be measured by inserting the PSTM into one arm of a Mach-zehnder type interferometer [102, 103, 104]. Recently, Burresi and coworkers have modified a PSTM to probe also the polarization state of the optical near-field [105].

Heterodyne interferometric PSTM has been used to visualize the phase singularities of the optical field on a waveguide [102] and above a grating [103], to track optical pulses in real space and time in a photonic crystal waveguide [106, 107], to observe focusing of SPPs using a phase-matched grating [8], and to visualize excitation of the highly confined SPPs on a nanowire [108]. In this section, a heterodyne interferometric PSTM is demonstrated as a tool to image the amplitude and the phase of the SPP field, generated on a flat gold surface, in the Kretschmann-Raether configuration. A schematic of the experimental setup is shown in Fig. 3.8.

The laser light was divided into two branches using a 50/50 beam splitter: the signal branch and the reference branch. The signal branch includes the sample and the scanning tip. The sample was arranged as explained in Section 2.6. The optical frequency in the reference branch was shifted by 40 kHz using two Acousto-Optic Modulators: AOM1 and AOM2, which were driven at frequencies of 80.04 MHz and 80 MHz, respectively. The difference frequency (40 kHz) was used as the reference for a dual-phase lock-in-amplifier.

The electric fields in the signal branch and the reference branch can be represented [85] as

$$\mathrm{E_{SB}(x,y)} = \mathrm{E_s(x,y)e^{i[\frac{\omega_o}{2\pi}t+\phi_s(x,y)]}}, \tag{3.8}$$

and

$$\mathrm{E_{RB}} = \mathrm{E_r e^{i[(\frac{\omega_o}{2\pi}+40kHz)t]}}, \tag{3.9}$$

---

[2] The near-field intensity profile imaged using the PSTM has been used by the Integrated Optical and Microsystems (IOMS) group at the University of Twente to estimate the refractive index profile at the end face of the integrated waveguide.

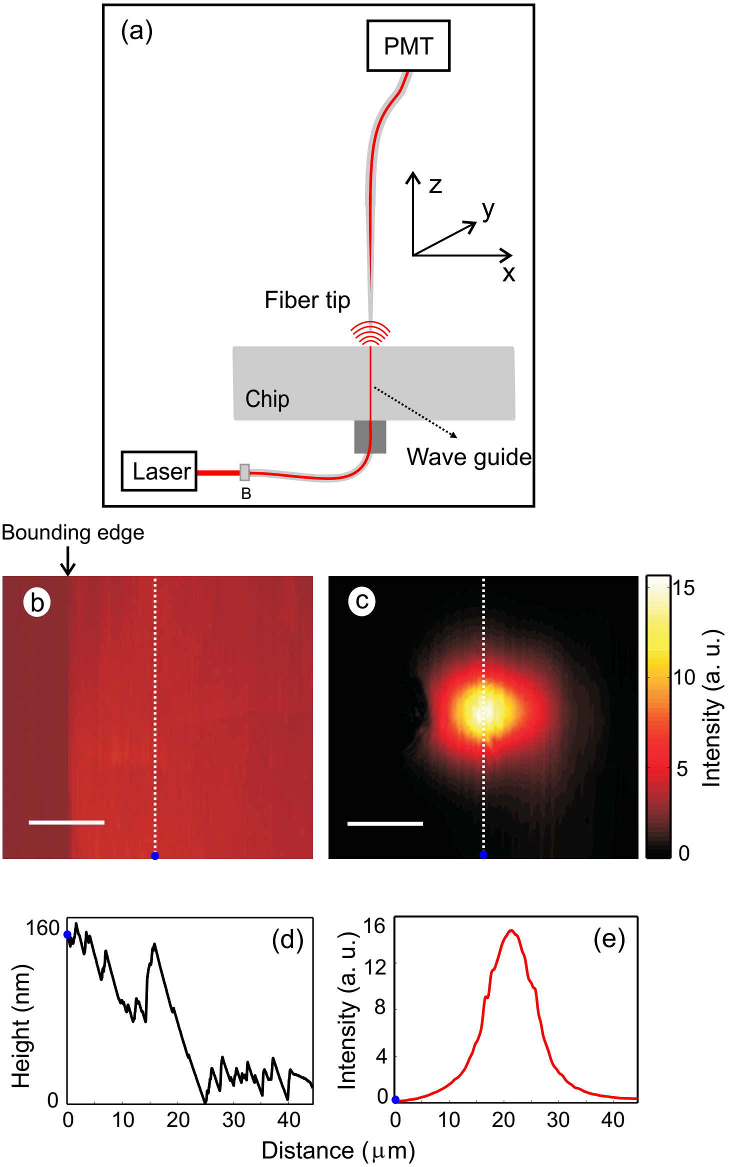

Figure 3.7: (a) Schematic of the PSTM setup to detect the intensity of light emerging from an integrated optical waveguide. B: Objective lens (b) The topography and (c) the optical intensity as detected by the tip. (d) and (e) Line traces along the white dotted lines in (b) and (c), respectively. The scale bar is 12 µm.

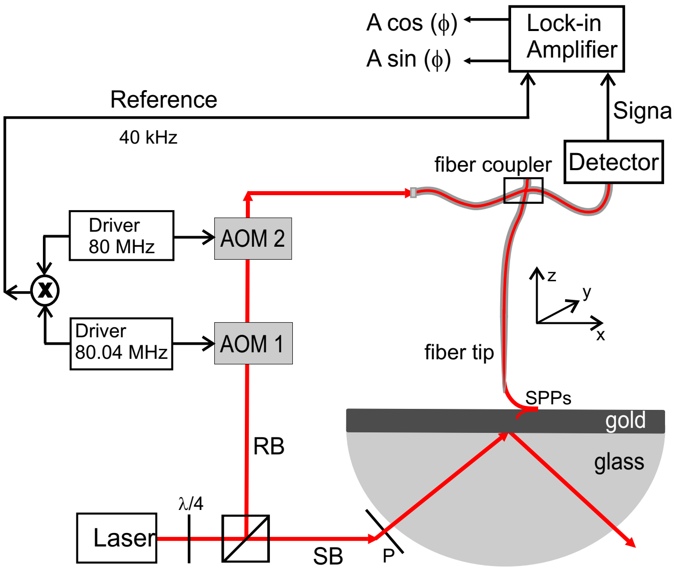

Figure 3.8: Schematic of a heterodyne interferometric PSTM. SB: Signal Branch, RB: Reference Branch, P: Polarizer, AOM: Acousto Optic Modulator.

respectively, where E_s and E_r are the real amplitudes of the optical field in the signal branch and the reference branch, respectively. ϕ_s is the phase of the optical field on the sample surface (with respect to the phase of the incident optical field), and $\omega_\circ$ is the incident laser frequency. Both the amplitude E_s and the relative phase ϕ_s are a function of the position (x and y).

The signal picked up by the tip is much lower than the signal in the reference branch and is detected by interfering with the signal in the reference branch. The interference occurs in a 2 × 2 fiber coupler. Depending on the optical path length difference between the signal branch and the reference branch, the interference is either constructive or destructive. The interference signal is detected using a photodiode and the output from the detector is given by

$$\begin{aligned} I_{det} &= [E_{SB}(x,y)+E_{RB}]^2, \\ I_{det} &\propto E_s^2(x,y)+E_r^2+2E_s(x,y)E_r\cos[40\mathrm{kHz}t+\phi_s(x,y)]. \end{aligned} \tag{3.10}$$

In a conventional PSTM (no interferometry), only the first term $E_s^2(x,y)$ is detected. The third term is the interference term and is proportional to $E_s(x,y)E_r$. Since $E_s \ll E_r$, the interference signal is much stronger than $E_s^2(x,y)$. The output from the detector is send to the lock-in-amplifier, which is locked at 40 kHz. One of the two output signals from the lock-in-amplifier is given by

$$\begin{aligned} V_1(x,y) &\propto 2E_s(x,y)E_r\cos[40\mathrm{kHz}t+\phi_s(x,y)]*\cos(40\mathrm{kHz}t), \\ &\propto 2E_s(x,y)E_r\cos[\phi_s(x,y)], \\ &\propto A\cos[\phi(x,y)], \end{aligned} \tag{3.11}$$

where $\phi(x,y) = \phi_s(x,y)$ and $A = 2E_s(x,y)E_r$ are the optical amplitude and the phase of the local field on the sample surface. Similarly, the 90° phase shifted output from the lock-in-amplifier is given by

$$V_2(x,y) \propto A \sin[\phi(x,y)]. \tag{3.12}$$

Using the two outputs from the lock-in-amplifier, both A and $\phi(x,y)$ are obtained as

$$A(x,y) \propto \sqrt{(V_1^2 + V_2^2)}, \tag{3.13}$$

and

$$\phi(x,y) = \tan^{-1}(\frac{V_2}{V_1}). \tag{3.14}$$

3.6.3 Complex SPP field detection

Linearly polarized light (free space wavelength of 632.8 nm) was converted into circularly polarized light using a quarter-wave plate (Fig. 3.8). By rotating the polarizer (P in Fig. 3.8), the polarization of the incident light can be changed from p to s. The incident angle is fixed at surface plasmon resonance angle, at which the reflected intensity showed a minimum (as shown in Fig. 2.9b in Chapter 2). Interferometric PSTM images of a complex SPP field detected on a flat gold surface are presented in Fig. 3.9. The topography of the sputter-coated gold film of thickness 50 nm is shown in Fig. 3.9a. The image shown is after correcting the tilt [109]. Dust particles with a height of approximately 40 nm can be seen. Figures 3.9b and 3.9c show the optical amplitude on the gold-air interface for p- and s-polarized incident light, respectively. The laser intensities for both p- and s-polarized incident beams were maximized before the respective measurements by turning the quarter-wave plate.

For the p-polarized incident beam, SPPs are excited at the gold-air interface and hence we see a higher optical amplitude in Fig. 3.9b compared to Fig. 3.9c. The cosine of the optical phase on the gold surface for p- and s-polarized incident light are depicted in Fig. 3.9d and 3.9e, respectively. The cosine of the phase of the optical field, for both polarizations, shows a plane wave propagation on the sample surface. The periodicity is the same in both images since the illumination angle is the same. The disturbances seen on the images taken for s-polarization are attributed to the low signal picked up by the tip. The fact that the observed wavefronts are straight and parallel show a high degree of stability of the interferometric set-up.

3.6.4 Imaging SPP interference

Interference between SPPs has two interrelated applications. It can create a periodically patterned metal surface which has applications in nanolithography [41]. On the other hand, a periodically patterned metal surface can generate interference between SPPs which leads to the formation of a photonic band gap material [110]. The field distribution and propagation direction of the SPPs on the patterned metal surface can be imaged and decomposed using the interferometric PSTM, which can help to design and optimize a patterned surface, for example to focus the SPPs [16].

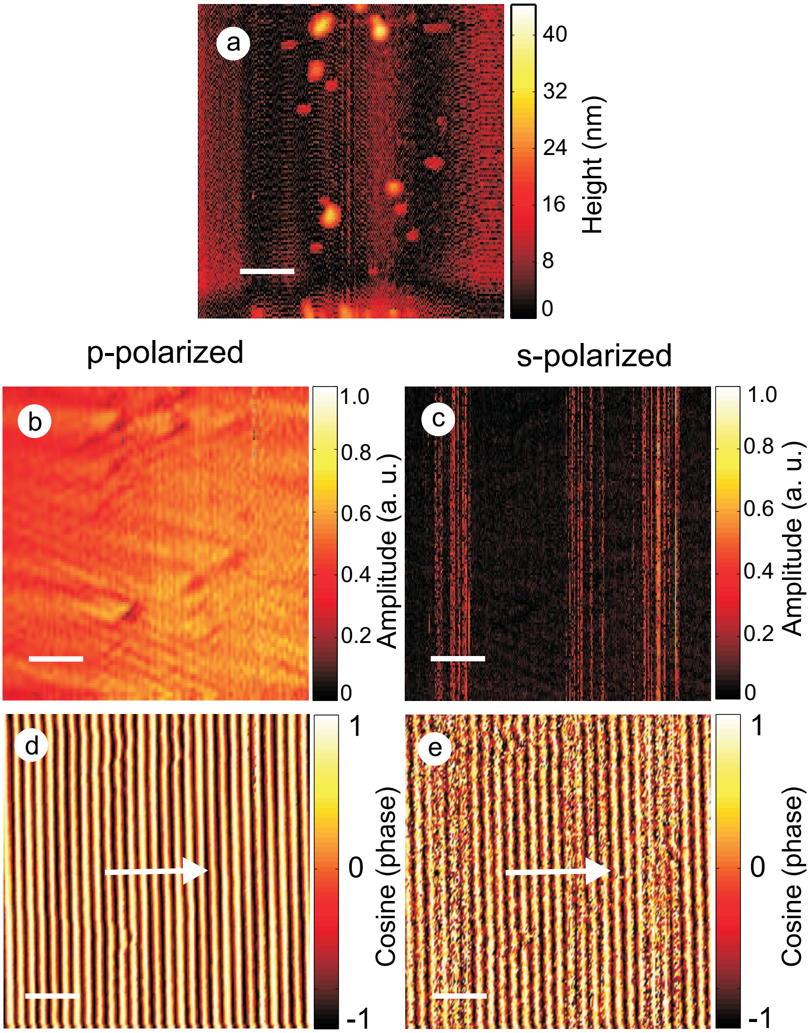

Figure 3.9: Interferometric PSTM measurement of a gold surface. (a) The measured topography. (b) and (c) The measured optical amplitude for p- and s-polarized incident light, respectively. (d) and (e) The cosine of the phase of the optical field for p- and s-polarized incident light, respectively. The arrows indicate the propagation direction of light. The scale bar is 2.7 μm.

Chapter 2 showed the excitation of SPPs on a gold surface via a prism and a grating. A combination of the prism and the grating allows the simultaneous excitation of the prism-coupled and the grating-coupled SPPs, for a suitable incident angle (θ) and in-plane rotation angle (β) of the grating (Chapter 4 gives a detailed explanation). The crossing point of the surface plasmon resonance bands (Fig. 4.9a in Chapter 4) implies the interference between SPPs coupled by the 0^{th} and the -1^{st} order evanescent waves. The interferometric PSTM can be used to image the complex SPP interference field at the gold-air interface of a buried grating. The fabrication of the buried grating is presented in Chapter 4. The measured topography and optical amplitude are shown in Fig. 3.10a and 3.10b, respectively. In Fig. 3.10c and 3.10d, line traces taken perpendicular to the grooves of the grating in the topography and the optical amplitude images, respectively, are shown. The topography of the grating shows a residual modulation of 34.5 ± 3.9 nm. A comparison between the topography and the optical amplitude line traces shows a higher optical amplitude on the troughs of the grating and a lower optical amplitude on the peaks of the grating.

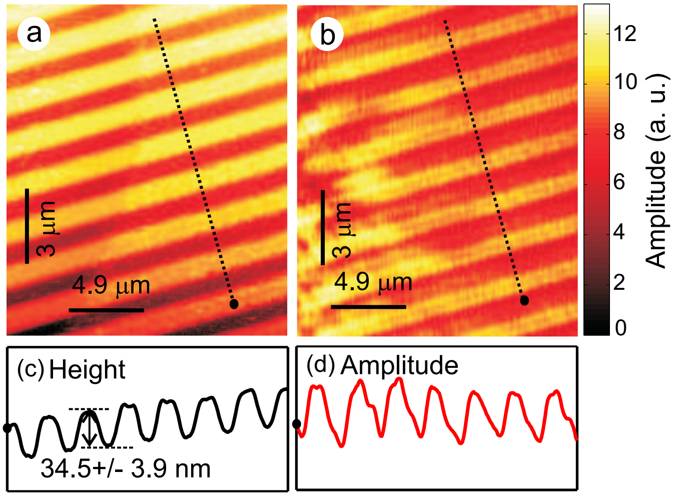

Figure 3.10: Interferometric PSTM measurement of a gold buried grating. (a) The measured topography. The dark and bright regions indicate the troughs and the peaks, respectively. (b) The measured optical amplitude. (c) and (d) Line traces taken along the black dotted lines in (a) and (b), respectively.

The cosine of the phase of the optical field is depicted in Fig. 3.11a. To investigate the different spatial frequencies in the optical field, a 2D Fourier transform of the optical field is taken [104], of which a zoom-in region is shown in Fig. 3.11b. Two prominent features are visible: the 0^{th} and the -1^{st} diffracted orders. The 0^{th} and the -1^{st} diffracted orders correspond to the excitation of the prism-coupled and the grating-coupled SPPs, respectively. The $+1^{\text{st}}$ diffracted order has a relatively low amplitude due to the absence of coupling to SPPs. The strength of the -1^{st} diffracted order relative to the peak amplitude in the 0^{th} diffracted order is 0.23; while that of the $+1^{\text{st}}$ diffracted order is 0.04. The 0^{th}, -1^{st}, and the $+1^{\text{st}}$ diffrac-

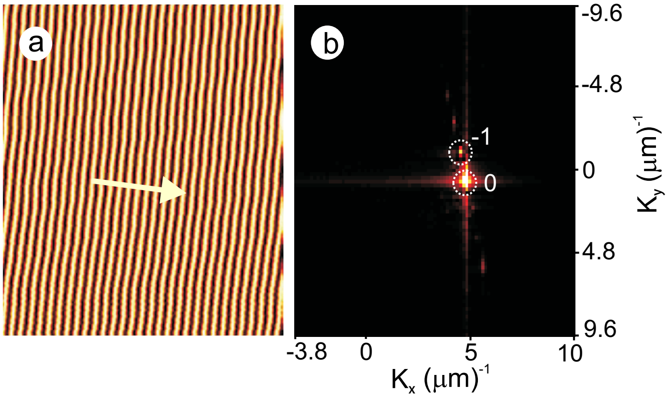

Figure 3.11: (a) The cosine of the phase of the optical field detected on the buried grating. The arrow indicates the propagation direction of the 0^{th} diffracted order. (b) Two-dimensional Fourier transform of the total optical field (an enlarged portion is shown for clarity).

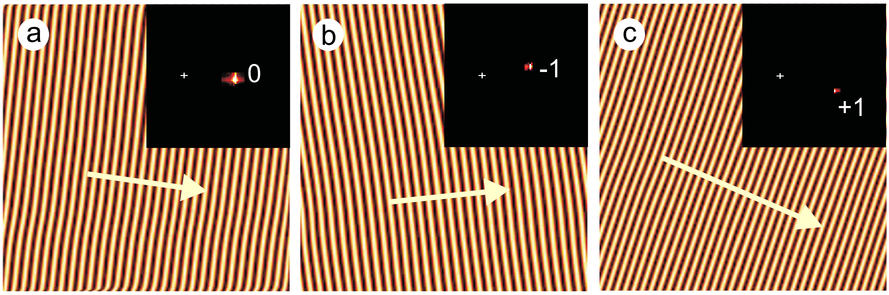

Figure 3.12: Two-dimensional inverse Fourier transform of Fig 3.11b, after separating the three different spatial frequencies. (a) The 0^{th}, (b) the -1^{st}, and (c) the $+1^{\text{st}}$ order diffracted plane waves propagating in different directions. The cosine of the phase is shown for a scan range of 13.3 μm × 18.5 μm. The wave vectors are denoted by the arrows. The insets show the corresponding frequency domain images each of size 4.8 μm^{-1} × 10 μm^{-1}. The white crosses indicate the zero spatial frequency point in the image. To see the feature clearly, a different amplitude normalization was used for the inset in (c).

ted orders are selectively separated and are shown as insets in Fig. 3.12a - 3.12c. An inverse Fourier transformation of the separated features give plane waves propagating at different in-plane directions. The angle between the 0^{th} and the -1^{st} order diffracted components is 19.3°, which is close to the calculated angle, of 20°, between the propagation direction of the prism-coupled and the grating-coupled SPPs. The $+1^{\text{st}}$ diffracted order has a shorter wavelength indicated by a longer in-plane wave vector component in Fig. 3.12c. The in-plane interaction between the two SPPs can be studied by investigating the amplitude and phase relationship between the interfering SPPs.

4

Phase shifts at surface plasmon resonance

4.1 Introduction

The high field enhancement on a metal surface due to the excitation of Surface Plasmon Polaritons (SPPs) has been exploited in the sensing of bio-chemical molecules [5]. The sensitivity of a Surface Plasmon Resonance (SPR) sensor is defined as the smallest change that can be detected in the refractive index or thickness of the medium in contact with the SPPs. SPR sensors have been operated by detecting the change in the angle or wavelength of the absorption dip [111], or by detecting the intensity and phase change [22] in reflection. Among these methods, the phase-detection provides the highest sensitivity due to the abrupt phase jump at the SPR [22, 24, 112]. In laboratory, the phase-detection SPR sensors [15, 22, 112, 113] have been extensively studied, although such SPR sensors are comparatively difficult to commercialize due to the high stability requirements.

The phase change at SPR was measured for the first time using ellipsometry [114]. The difference in the phase change for p- (or parallel) and s- (or perpendicular) polarized incident light in reflection was measured. The s-polarized light was used as a reference in the measurement, due to the fact that the s-polarized incident light do not excite SPPs. However, the phase in the s-polarized light varies slowly at the SPR due to a phase change in the associated evanescent waves. More commonly, an

SPR sensor is inserted in one arm of an interferometer to retrieve the displacement in the phase change [23]. Like the ellipsometric measurement, the interferometric measurement also uses s-polarized light as a benchmark to measure the phase change [14]. However, for a fixed incident angle, the variation of the phase change in the evanescent wave associated with the s-polarized light is different when compared to that of the p-polarized light.

4.2 Resonant phase shift across a glass-metal transition region

Instead of using s-polarized light as a reference, a system that does not support SPPs, such as a glass-air system can be used to measure the phase shift at SPR. A recent interferometric study reported a measurement of the difference between the phase change upon reflection off a glass-gold interface and that off a glass-air interface, at normal incidence in the far field, using a back reflection geometry [115]. In this Section, a near-field detection of the phase shift at SPR is presented. Evanescent waves generated in a glass-gold-air system and a glass-air system are probed from the air side to extract the phase difference of evanescent waves between the two systems, as a function of incident angle.

4.2.1 Goos-Hänchen effect

Total internal reflection of light at an interface separating a denser (for example, glass) and a rarer (for example, air) medium is associated with the generation of evanescent waves in the rarer medium [1]. In 1947, Goos and Hänchen demonstrated a lateral displacement of the total internally reflected beam, thereafter known as the "Goos-Hänchen (GH) effect" [18]. In their experiment, the total internally reflected beam was found to be displaced, with respect to a beam reflected off an adjacent thick metal layer, by few micrometers [2]. A schematic of the GH effect in total internal reflection is shown in Fig. 4.1. For a linearly polarized light total internally reflected at a glass-air interface, the lateral displacement (or GH shift) is perpendicular to the propagation direction of the reflected light in the plane of incidence [116]. The GH shift is maximum just after the total internal reflection and decreases thereafter with increasing incident angle. In the glass-air system, the GH shift is of the same scale as the illumination wavelength [20, 117]. However, GH shift of a few microns has been observed in left-handed materials (or metamaterials) [118] and on surfaces exhibiting SPR-like material resonance [119].

The GH shift is defined [120] as

$$\mathrm{D} = -\frac{\lambda_{\circ}}{2\pi \mathrm{n}}\frac{\mathrm{d}\phi}{\mathrm{d}\theta}, \tag{4.1}$$

where $\lambda_{\circ}$ is the free space wavelength, n is the refractive index of the denser medium, $\frac{\mathrm{d}\phi}{\mathrm{d}\theta}$ is the rate of change of phase in total internal reflection. The negative sign in D implies a negative slope for the phase change. Enhancement of the GH shift, to a few micrometers [117, 121], due to SPR has been shown to increase the sensitivity of SPR sensors [22, 23, 24].

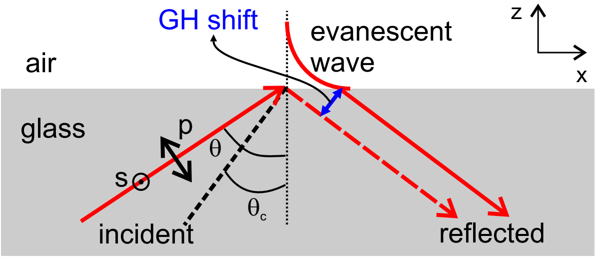

Figure 4.1: Schematic of the Goos-Hänchen (GH) shift in total internal reflection of light in a glass-air system. θ_c is the critical angle of incidence.

The GH shift occurs due to the difference in the phase between the incident and the reflected beams [19]. A change in the phase of the reflected beam implies a corresponding change in the phase of the evanescent waves. The phase change in total internal reflection can be obtained using the Fresnel equations. For p-polarized incident light, the Fresnel reflection and transmission coefficients in the glass-air system [32] are given by

$$r_{ij}^{p} = \frac{n_j^2 k_{\perp i} - n_i^2 k_{\perp j}}{n_j^2 k_{\perp i} + n_i^2 k_{\perp j}}, \tag{4.2}$$

and

$$t_{ij}^{p} = r_{ij}^{p} + 1, \tag{4.3}$$

where i and j denote glass and air with refractive indices n_i and n_j, respectively. $k_{\perp i}$ and $k_{\perp j}$ are the perpendicular components of the incident wave vector in the two media given in Eq. (2.5) in Chapter 2. Similarly, for s-polarized incident light, the Fresnel coefficients are given by

$$r_{ij}^{s} = \frac{k_{\perp i} - k_{\perp j}}{k_{\perp i} + k_{\perp j}}, \tag{4.4}$$

and

$$t_{ij}^{s} = r_{ij}^{s} + 1. \tag{4.5}$$

4.2.2 Combination of Goos-Hänchen and SPR effects

For a glass-gold-air system, the phase change in the Fresnel transmission coefficients can be calculated using Eq. (2.9) and (2.10) in Chapter 2. A schematic of the glass-air and the glass-gold-air systems adjacent to each other is shown in Fig. 4.2a. Evanescent waves are generated by total internal reflection on the glass-air interface and SPPs by the Kretschmann-Raether configuration in the glass-gold-air stack. The different optical constants for glass and gold as well as the thin layer of gold on the glass surface induces a stationary difference between the phases of the evanescent waves on the glass-air and the gold-air interfaces. In addition to this constant phase difference, there are two other significant phase changes that vary with the incident angle: one associated with the Goos-Hänchen effect on the glass-air interface and another with the SPR effect on the gold-air interface. The phase change associated with the SPR effect occurs only when the incident light is p-polarized; not when it is s-polarized. The phase change in the Fresnel transmission coefficients for p- and s-polarized incident light, as a function of the incident angle, for the glass-air and the glass-gold-air systems are shown in Fig. 4.2b. The phase changes for the p- and s-polarized incident light vary by different amounts with the incident angle [122]. The phase change associated with the Goos-Hänchen effect and the SPR effect have been separately studied in the past [15]. By combining the glass-air system with a glass-gold-air system, the differences in the phase change between the two systems can be measured.

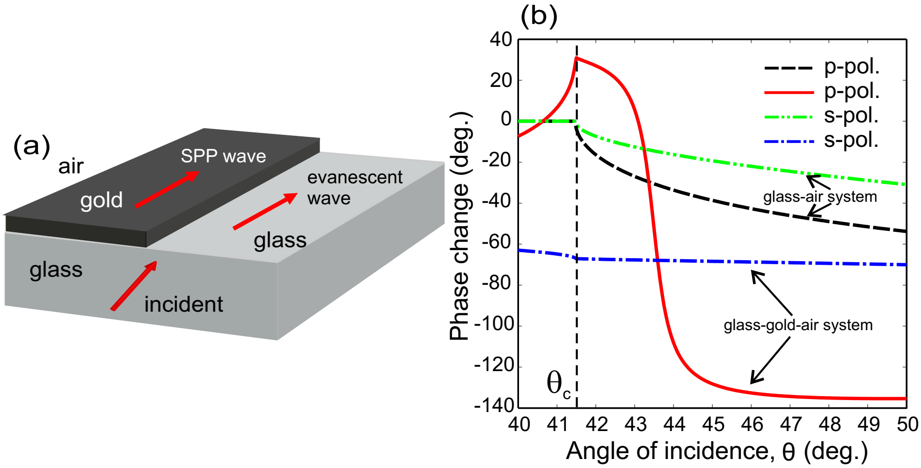

Figure 4.2: (a) Schematic of the transition region between glass and gold supporting the evanescent and the SPP waves, respectively. (b) Calculated phase change in the Fresnel transmission coefficients as a function of the incident angle for a glass-air and a glass-gold-air system. θ_c is the critical angle of incidence for total internal reflection on the glass-air interface.

4.2.3 Spatial phase evolution on glass-metal transition region

Photon Scanning Tunneling Microscope (PSTM) measurements were performed on a commercially available gold SPR sensor (Ssens) with a titanium adhesive layer on a 10 × 10 × 0.3 mm glass substrate. The thickness of the gold layer was approximately 50 nm. Using Focused Ion Beam (FIB) milling, a ‘glass window’ on the sample was made by removing a 50 μm×500 μm strip of gold. A Scanning Electron Microscope (SEM) image of the glass window on the gold sample is shown in Fig. 4.3a. Technical constraints on the FIB milling of the gold made it impossible to remove the gold completely from the glass substrate and hence traces of gold remained (Fig. 4.3b). The sample was arranged in the Kretschmann-Raether configuration as explained in Chapter 2. The region of interest is the transition from glass-air to gold-air. The laser light (free space wave length of 632.8 nm) was focused to the glass-gold transition region of the sample. The sample was oriented in such a way that the gold 'step' was parallel to the plane of incidence so that reflection effects due to the gold step were eliminated [123].

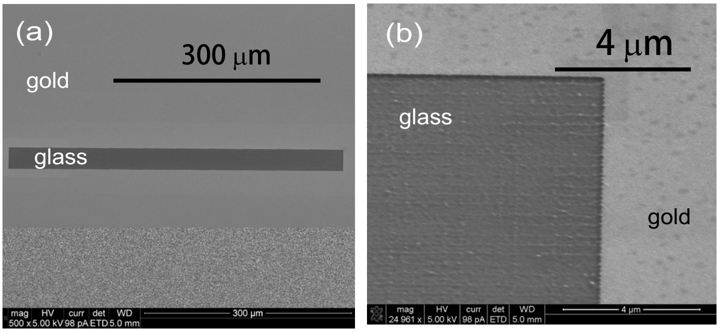

Figure 4.3: (a) SEM image of a 'glass window' milled into a 50 nm thick gold film and (b) an enlarged portion of the corner of the glass window.

The incident angle was fixed at 43.3° to excite SPPs on the gold-air interface. Owing to the inhomogeneous nature of evanescent waves, the phase change upon evanescent wave coupling into the fiber, across an air gap, is independent of the width of the gap [124]. The PSTM images for s- and p-polarized incident light are shown in Fig. 4.4. The height of the gold step is measured to be 49.2 nm in Fig. 4.4a and 51 nm in Fig. 4.4d. The difference in the heights could be due to a FIB milling error of ±5 nm or the different regions scanned on the sample. The optical amplitude measured is uniform above each interface (Fig. 4.4b and 4.4e). For s-polarized incident light, the optical amplitude on the gold region is lower due to a lower transmission through the gold film in the absence of SPPs. For p-polarized incident light, the field amplitude increases on the gold region of the sample compared to the glass region due to the excitation of SPPs on the gold-air interface. Small features on the gold surface scatter the SPPs [125], which is seen as strong amplitude variations on the gold region. The cosine of the phase of the optical field on the transition region for p- and s-polarized incident beams is shown in Fig. 4.4c and 4.4f, respectively.

The spacing between adjacent dark or bright lines is a direct measurement of the in-plane wave vector component $k_{\parallel}$ (with a period $\lambda_{\parallel}$ given in Eq. (2.8)) of the incident light on the sample surface. The measured $\lambda_{\parallel}$ is 576 nm. The incident angles calculated back from the measured values of $\lambda_{\parallel}$ are found to be increased by approximately 3° from the set value of the incident angle. This discrepancy between the observed and the back-calculated incident angles might be due a refraction of the incident light in the glass prism (mentioned in Chapter 2). To avoid ambiguity in the generation of SPPs, the PSTM measurements were cross-checked with reflectivity measurements.

4.2.4 Measurement of the phase shift at SPR

The phase shift can be defined as the phase difference between the two waves with the same spatial frequency. For p-polarized incident light, the incident angle was varied from 42.2° to 43.6° to measure the phase shift across the glass-gold transition

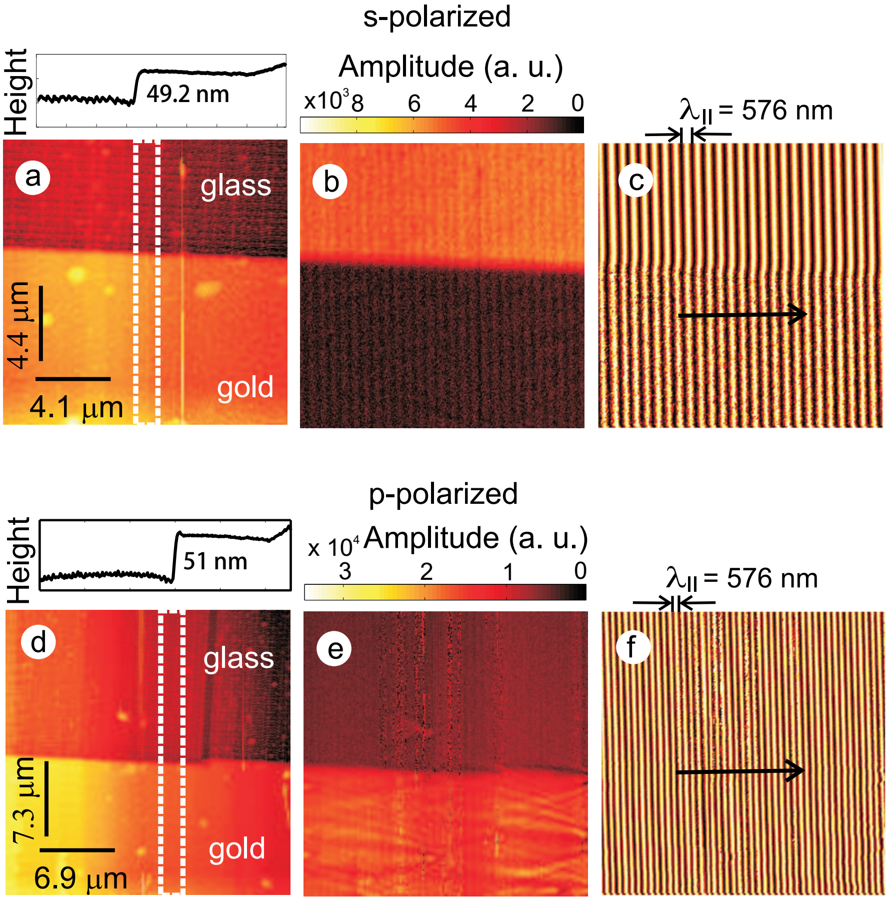

Figure 4.4: Interferometric PSTM measurement of the glass-gold transition region of the sample. (a) Topography, (b) optical amplitude and (c) cosine of the phase of the optical field for s-polarized incident beam. (d) Topography, (e) optical amplitude and (f) cosine of the phase of the optical field for p-polarized incident beam. The height profile averaged over an area indicated by a white dashed rectangle in the topography image is shown above the corresponding topography image.

region. The PSTM images obtained using a metal coated fiber tip are depicted in Fig. 4.5. Figure 4.5a shows the measured topography of the glass-gold transition region. The images Fig. 4.5b - 4.5e show the evolution of the phase shift across the glass-gold transition region.

Using a two-dimensional Fourier transform, the phases on the gold and glass regions of the sample were extracted from the PSTM images for incident angles ranging from 40° to 50°. Figure 4.6a shows the difference between the phases, together with the calculated phase difference (from Fig. 4.3d). The change in measured phase difference is 130°, which agrees well with the theory and is caused mainly by the enhanced spatial phase shift on the glass-gold-air system due to the generation of SPPs. This enhanced phase shift corresponds to a GH shift [119] of 3.5 µm, calculated using Eq. (4.1). Interestingly, we see an offset in the phase difference

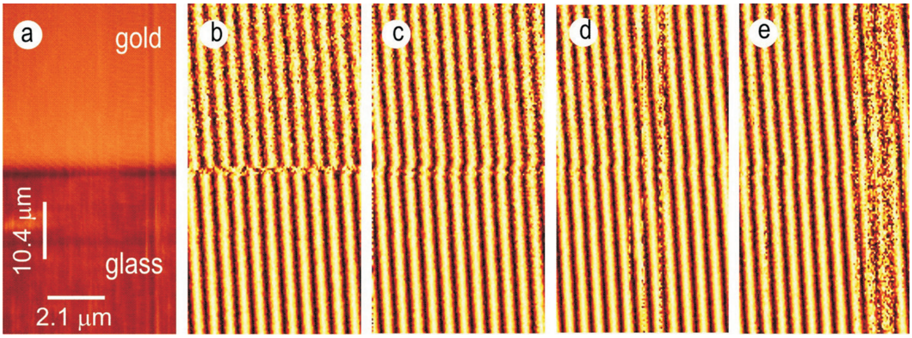

Figure 4.5: Interferometric PSTM images for a p-polarized incident light. (a) Topography, and the sine of the spatial phase for different incident angles (b) 42.2°, (c) 42.7°, (d) 43.3°, and (e) 43.6°.

measured using a coated fiber tip compared to that measured using an uncoated fiber tip for both p- and s-polarized incident light. The interaction between the metal coated probe and the surface might introduce an additional phase shift for the entire range of incident angles, which may explain the offset observed.

The far-field reflection measurement explained in Chapter 2 was performed to cross-check the generation of SPPs. The absorption dip in the reflection measurement for the p-polarized incident light clearly indicates the SPR angle as 43.3°. Figure 4.6b shows a comparison between the far-field reflection measurement and the near-field PSTM measurement. The distinct change in the phase difference of 130° is measured over the SPR range for the p-polarized incident light, whereas a negligible change is measured over the SPR region for the s-polarized incident light. A minor fluctuation is seen in the reflected intensity, which is attributed to polarization impurity. This impurity leads to a similar fluctuation in the corresponding phase difference plot. A change in the ambient refractive index influences the SPPs so that the location of the sharp phase shift associated with the SPR would move along the *angle of incidence* axis [23]. However, the location of the measured shift in phase difference for the p-polarized incident beam coincides with the absorption dip in the plot obtained from the reflection measurement. This observation underlines the fact that the measured change in phase difference is not influenced by the presence of the PSTM tip.

4.3 Resonant phase shift on a metal grating

The sensitivity as well as the dynamic range of an SPR sensor can be improved by using a metallic grating [126]. The measurement of the phase change on a grating, associated with the SPR effect, is complicated due to the phase changes associated with the modulated grating surface. Incident light with s-polarization state has been used to measure the phase shift at the grazing emergence of a diffracted order on a grating surface (or called ‘Rayleigh anomaly’) [127]. An in-plane rotation of the grating will break the diffraction symmetry, so that the s-polarized beam can also couple to SPPs. In this section, a different approach is introduced to detect

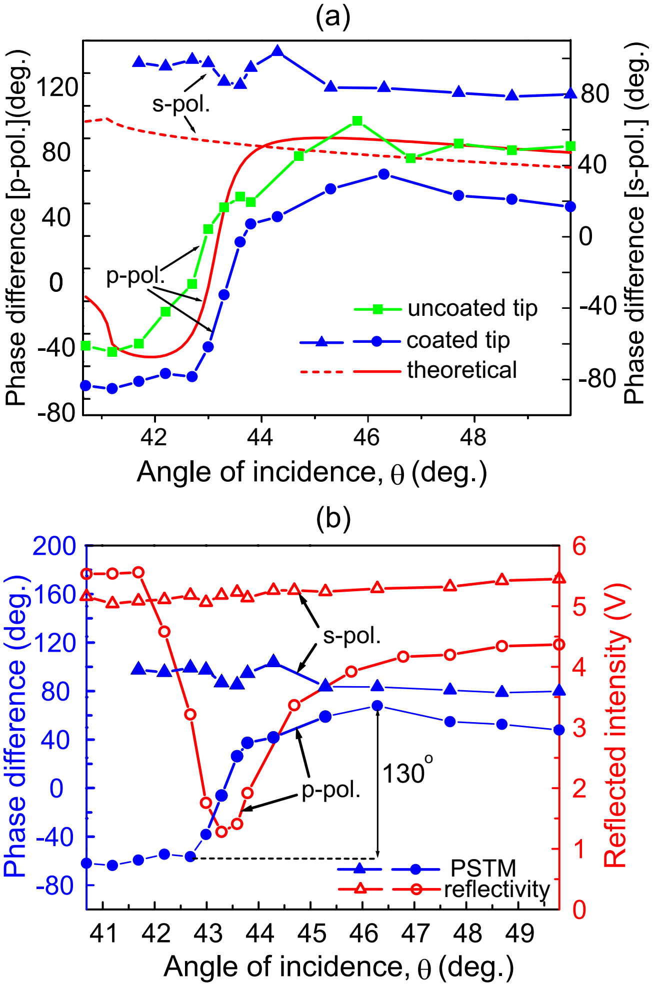

Figure 4.6: (a) Comparison between the theoretical and experimental phase difference as a function of the angle of incidence for p- and s-polarized incident light. (b) Comparison between the far-field reflectivity and the near-field PSTM measurements for p- and s-polarized incident light.

the phases of the resonant and the non-resonant diffracted orders simultaneously using the PSTM. The phase of the non-resonant diffracted order can then be used as the reference to extract the phase of the resonant diffracted order.

4.3.1 Grating orientations: classical and conical mounts

Excitation of SPPs using the prism and the grating coupling schemes are commonly used separately. A grating can be combined with the prism to simultaneously generate multiple SPPs (presented in Chapter 3), to decouple SPPs to light into the air space via the grating [36], or to induce cross-coupling between SPPs excited on both sides of the grating [39]. In the diffraction of light by a one-dimensional grating combined with the Kretschmann-Raether configuration, the grating can be arranged in two different mounts: a classical and a conical mount [128] as shown in Fig. 4.7a and Fig. 4.7b, respectively.

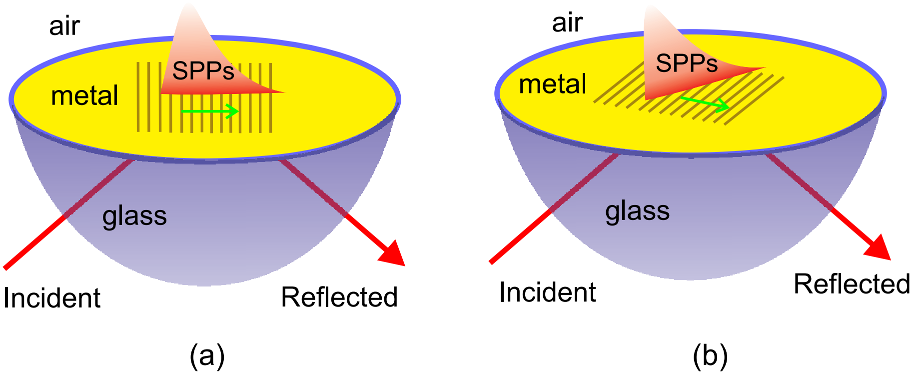

Figure 4.7: A grating combined with a Kretschmann-Raether configuration arranged in (a) a classical mount to excite collinear SPPs, and (b) a conical mount to excite non-collinear SPPs. The green arrows indicate the grating wave vectors.

Classical mount

In the classical mount, the grating lines are perpendicular to the plane of incidence, and hence the different diffracted orders lie in the plane of incidence. The SPPs, excited by the addition or substraction of the grating wave vector $\mathrm{k_g}$ (equal to $\frac{2\pi}{\Lambda_\mathrm{g}}$, where Λ_g is the period of the grating), propagate perpendicular to the grating lines. The SPP wave vector $\mathrm{k_{spp}}$, the grating wave vector $\mathrm{k_g}$, and the in-plane wave vector of the incident light $\mathrm{k}_\parallel$ all lie in the plane of incidence. Hence the SPPs excited in the classical mount are called ‘collinear SPPs’. Only p-polarized incident light can couple to collinear SPPs. Two counter-propagating SPPs, generated via a grating, create a band gap due to the formation of a standing wave on the grating surface [9].

Conical mount

In a conical mount, the grating lines are oblique to the plane of incidence, and hence the diffracted orders lie outside the plane of incidence [129]. The conical mount is achieved by an in-plane rotation of the grating, referred to as the ‘azimuthal angle’ β (Fig. 4.10c), from the plane of incidence. When $\beta = 0$, the conical mount reduces to the classical mount. The SPPs, that are excited via a grating arranged in the conical mount, propagate at an oblique angle to the grating lines and are called ‘non-collinear SPPs’. Both p- and s-polarized incident light can couple to non-collinear SPPs, provided that there is a component of the incident electric field along the direction of propagation of the SPPs [130, 131]. A binary grating [132] and a functional phase-matched grating [8] can themselves break the diffraction symmetry so that the type of the mount is an irrelevant issue in those cases.

The conical mount provides flexibility for the SPR sensor by tuning the azimuthal angle for a fixed illumination wavelength and incident angle. The phase matching condition to excite non-collinear SPPs on a metal-air interface via the grating wave vector (Fig. 4.10c) is given by

$$k_{spp}^2 = k_{\parallel}^2 + (mk_g)^2 \pm 2mk_{\parallel}k_g\cos\beta, \tag{4.6}$$

where m is the order of diffraction, and $k_{\parallel}$ and k_{spp} are the in-plane wave vector components of the incident light and the SPPs, as given in Eq. (2.6) and (2.7) in Chapter 2, respectively.

4.3.2 Fabrication

Surface plasmon polaritons propagating on a grating surface scatter into radiation [36, 44, 45]. The scattering can be reduced by turning the grating upside down to form a 'buried' grating; a detailed study of which is presented in Chapter 5. Thin film metallic gratings can be fabricated either using a top-down method such a Focused Ion Beam (FIB) milling or a bottom-up approach such as a lift-off technique. The measurement was performed on a buried grating that was fabricated using the FIB. The steps to fabricate the grating are illustrated in Fig. 4.8. A 125 μm×125 μm grating of period 1.65 μm, depth 50 nm, and duty cycle 0.5 was milled into 15 × 15 × 0.15 mm glass cover slip using the FIB (Fig. 4.8b). A thin layer of gold-palladium mixture was deposited on the glass cover slip prior to the milling action to eliminate charging effects (not shown). The grooves were then filled with gold using the FIB together with a gold gas injection system (Fig. 4.8c). SEM images of the grating filled with gold are shown in Fig. 4.9. A gold layer of thickness of 50 nm was deposited on top of the grating surface using electron beam evaporation technique (base pressure in the chamber equal to 2 × 10^{-6} mbar) to obtain a buried grating as shown in Fig. 4.8d. Drift of the FIB or an inaccurate dwell time for the filling of gold can cause a FIB positioning error and hence an over/under filling of the grooves. The sample was arranged in the Kretschmann-Raether configuration as explained in Chapter 2.

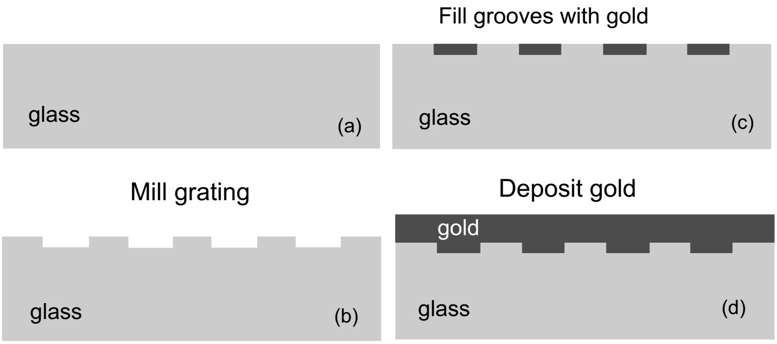

Figure 4.8: Fabrication of a gold buried grating using FIB mill and fill procedure.

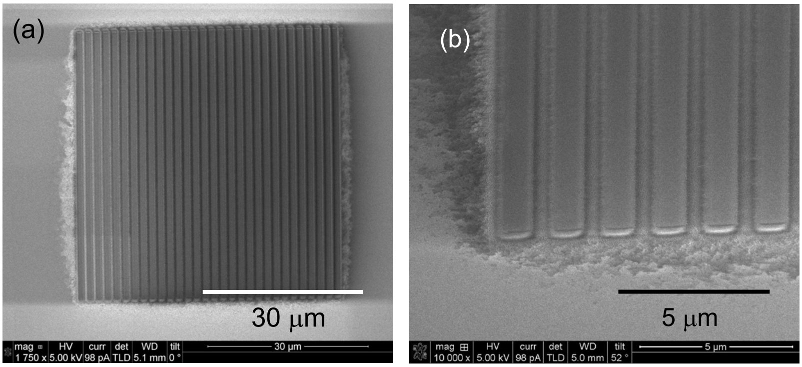

Figure 4.9: (a) SEM image of the grating filled with gold using FIB assisted deposition and (b) an enlarged portion of the bottom-left corner of (a).

4.3.3 Modeling

A buried gold grating is modeled [133] using the rigorous coupled wave analysis [134]. The grating parameters were taken from those of the fabricated buried grating. The complex dielectric function of gold was taken from Johnson and Christy [31]. The diffraction efficiency of the -1^{st} diffracted order in reflection as a function of the incident angle θ and the azimuthal angle β is shown in Fig 4.10a. The buried grating is shown as an inset. Sharp discontinuities in the diffraction efficiency plot correspond to the resonant excitation of SPPs. The values of the incident angle and the azimuthal angle for which SPPs are coupled via the grating wave vector are shown in Fig. 4.10b. The resonance bands, labeled as +1 and -1, are asymmetric with respect to the azimuthal angle for low values of β. This asymmetry in the resonance bands is due to fact that the grating wave vector $\mathrm{k_g}$ lies inside the gold-air SPP curve when the +m order couples to SPPs, and outside the gold-air SPP curve when the -m order couples to SPPs (Fig. 4.10c). In Fig 4.10a, a sharp resonance is seen at the incident angle of 44.3°, labeled as '0' and is independent of the azimuthal angle. The origin of the 0 resonance in the -1^{st} diffracted order is a two step process: first, the SPPs are excited at the gold-air interface by the evanescent tail of the specularly reflected beam (prism coupling) and second, the light reradiated from the SPPs back into gold is diffracted via the periodic corrugation at the gold-glass interface. Since the SPPs are excited via the prism coupling scheme, their propagation direction is independent of the in-plane rotation of the grating [36]. Interestingly, the incident angles for which the SPR occur shift significantly with the in-plane rotation of the grating [135], which can improve the dynamic range of grating incorporated SPR sensors [136].

4.3.4 Phase change in diffracted orders

The phase changes upon diffraction of light on dielectric and metallic gratings have been studied theoretically using methods such as an Iterative Series method [137] and a differential method [138]. A detailed theoretical calculation is beyond the

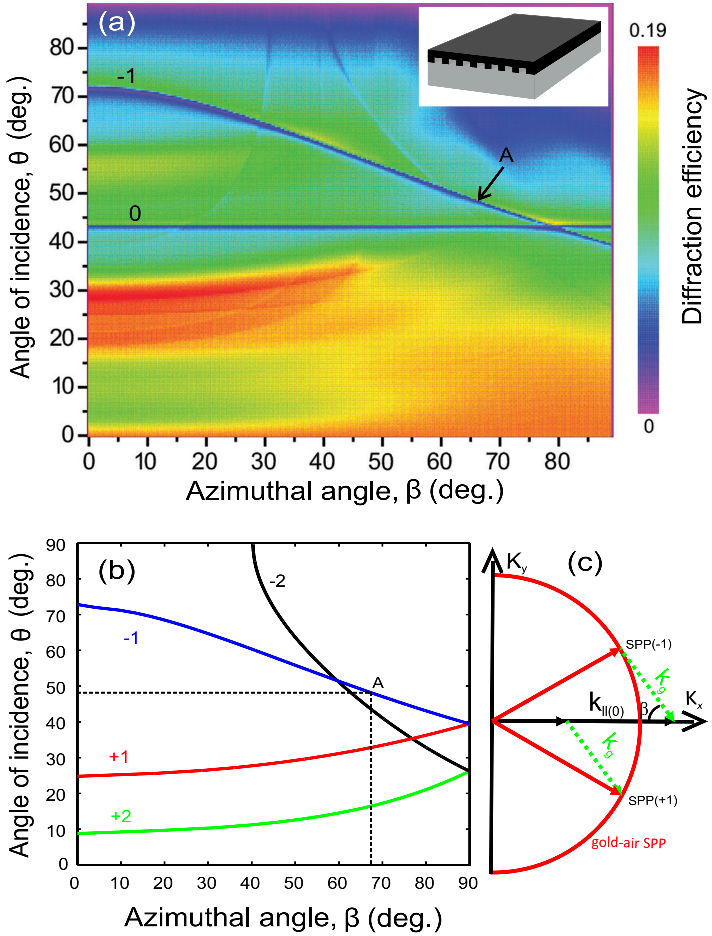

Figure 4.10: (a) The simulated diffraction efficiency in the -1^{st} diffracted order reflected off a grating at the gold-glass interface for varying incident angle θ and azimuthal angle β. The inset shows the buried grating. (b) The θ and β values for which SPPs are excited via the different diffracted orders. The marker 'A' denotes a location that was used in the experiment. (c) The reciprocal space representation of the excitation of SPPs via the -1^{st} and the $+1^{\mathrm{st}}$ diffracted orders for two different incident angles. The solid red curve denotes the momentum of the SPPs at the gold-air interface, the solid red arrow denotes the wave vector of the SPPs, the solid black arrow denotes the in-plane wave vector of the incident light, and the dotted green arrows indicate the grating wave vectors.

scope of this thesis. A theoretical model based on the Fresnel coefficients calculated for a glass-gold (50 nm)-air system is presented. The in-plane wave vector component of the $\pm 1^{\mathrm{st}}$ diffracted orders is given by

$$\mathrm{k}^2_{\parallel(\pm1)} = \mathrm{k}^2_{\parallel(0)} + \mathrm{k}_{\mathrm{g}}^2 \pm 2\mathrm{k}_{\parallel(0)}\mathrm{k}_{\mathrm{g}}\cos\beta, \tag{4.7}$$

where $\mathrm{k}_{\parallel(0)}$ is the in-plane wave vector component of the 0^{th} diffracted order. The Fresnel coefficients [Eq. (2.9) and (2.10) in Chapter 2] for a glass-gold-air system are calculated for the $\pm 1^{\mathrm{st}}$ diffracted orders. For a grating period of 1.65 µm and an azimuthal angle of 67°, the phase changes in the Fresnel transmission coefficients in the -1^{st} and the $+1^{\text{st}}$ diffracted orders as a function of the incident angle are shown in Fig. 4.11a. The abrupt jump in the phase at 46° (indicated by an arrow), is due to the grazing emergence of a diffracted order on the grating surface [139]. The drop in the phase around 48.5° is due to the resonant coupling to SPPs at the gold-air interface. The $+1^{\text{st}}$ diffracted order does not show a considerable change in phase for these incident angles due to the absence of a resonance.

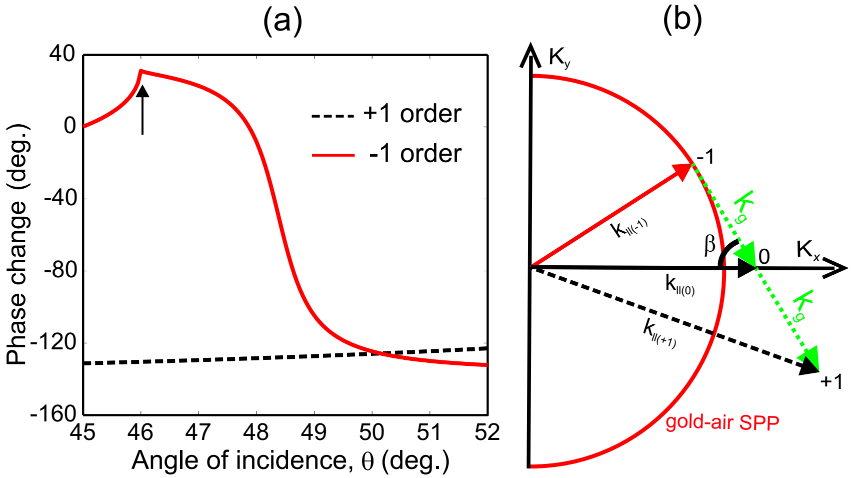

Figure 4.11: (a) Calculated phase change in the Fresnel transmission coefficients as a function of the incident angle for the -1^{st} and the $+1^{\text{st}}$ diffracted orders in a glass-gold (50 nm)-air system. The arrow indicates grazing of a diffracted order on the grating (Rayleigh anomaly). (b) The reciprocal space representation of the excitation of grating-coupled SPPs in a conical mount of the grating. The solid red curve denotes the momentum of the SPPs at the gold-air interface, the solid red arrow denotes the wave vector of the SPPs coupled via the -1^{st} diffracted order, the dashed black arrow denotes the wave vector of the $+1^{\text{st}}$ diffracted order, and the dotted green arrows indicate the grating wave vectors.

4.3.5 Excitation of grating-coupled SPPs

A reciprocal space representation of the excitation of SPPs via the -1^{st} diffracted order is shown in Fig. 4.11b. When the diffraction angle for a diffracted order is higher than the critical angle in total internal reflection for a glass-air interface, the diffracted order generates evanescent waves at the gold-air inerface. For a suitable combination of the incident angle and the azimuthal angle (marker 'A' in Fig. 4.10), the -1^{st} diffracted order couples to SPPs with an in-plane wave vector component denoted by $\mathrm{k}_{\|(-1)}$. The in-plane wave vector component corresponding to the evanescent waves generated by the 0^{th} order incident light is denoted by $\mathrm{k}_{\|(0)}$. For a fixed azimuthal angle, a change in the incident angle changes $\mathrm{k}_{\|(0)}$ and the $\mathrm{k}_{\|(-1)}$ goes through the SPR. The in-plane wave vector component $\mathrm{k}_{\|(+1)}$ is higher than the momentum of the SPPs and hence for the chosen range of incident angles, the $+1^{\text{st}}$ diffracted order can be taken as a reference to measure the phase change in the -1^{st} diffracted order.

4.3.6 Measurement of prism-coupled SPPs

Prism-coupled SPPs are excited, via the 0th diffracted order, on the buried grating that was arranged in the conical mount. The conical mount will break the diffraction symmetry and hence the diffracted orders will have different field strengths on the sample surface. The interferometric PSTM images for p-polarized incident light are shown in Fig. 4.12. The topography of the sample surface is shown in Fig. 4.13a. The optical amplitude image (Fig. 4.12a) shows a modulated field pattern. The cosine of the phase of the optical field (Fig. 4.12b) clearly shows plane waves associated with the 0th diffracted order ($k_{\parallel(0)}$). A two-dimensional Fourier transform of the complex optical field (Fig. 4.12c) shows that the brightest feature is the 0th diffracted order, which is due to the resonant coupling to SPPs. The magnitude of the -1^{st} diffracted order relative to the peak magnitude in the 0th diffracted order is 0.37; while that of the $+1^{st}$ diffracted order is 0.05. The relative magnitude of the -1^{st} diffracted order is higher than that of the $+1^{st}$ diffracted order, which is attributed to an unequal field strength for the evanescent waves associated with the -1^{st} and $+1^{st}$ diffracted orders on the grating surface due to their different diffraction angles. In addition, a difference in the coupling efficiency of the diffracted orders into the fiber tip of the PSTM has been reported for the different diffracted orders [11].

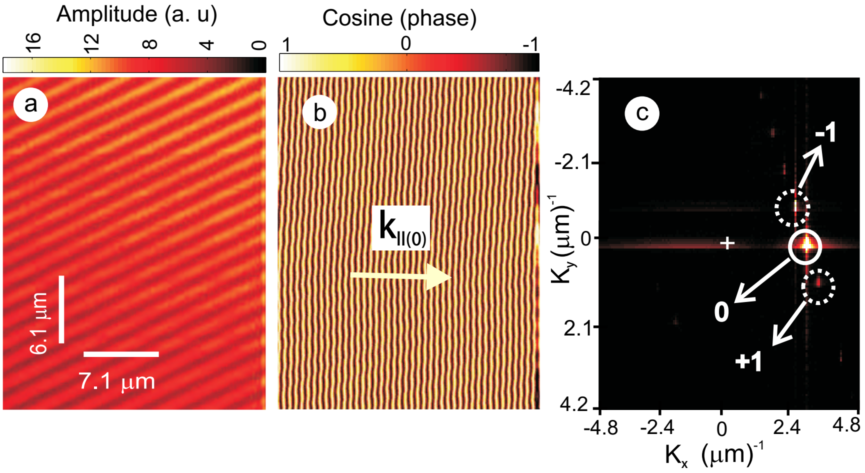

Figure 4.12: Interferometric PSTM measurement imaging SPPs excited via the 0th diffracted order. (a) The measured Optical amplitude, (b) the cosine of the phase of the optical field, and (c) the Fourier transform of the complex optical field.

4.3.7 Measurement of grating-coupled SPPs

For a p-polarized incident light, the incident angle was fixed at 48.5° and the azimuthal angle at 67° to excite SPPs via the -1^{st} diffracted order (marker 'A' in Fig. 4.10). The PSTM images obtained using a metal coated fiber tip are shown in Fig. 4.13. Figures 4.13a, 4.13b, and 4.13c show the topography, optical amplitude, and cosine of the phase of the optical field on the grating surface, respectively. A line trace

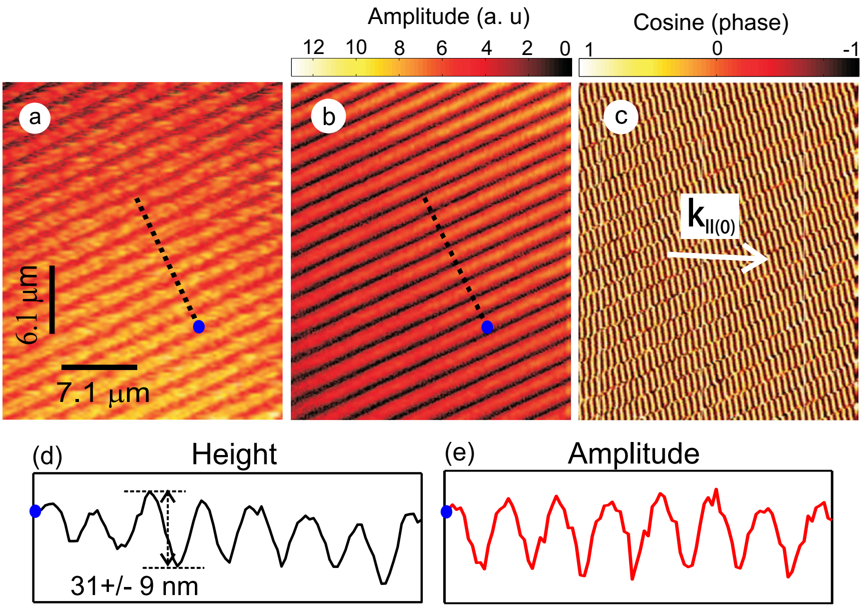

Figure 4.13: Interferometric PSTM images of the gold grating. (a) The measured topography, (b) the optical amplitude, and (c) the cosine of the phase of the optical field. The white arrow indicates the direction of $k_{\|(0)}$. (d) and (e) Line traces along the black dashed line.

perpendicular to the grating lines is shown in Fig. 4.13d. The residual modulation on the grating is measured to be 31 ± 9 nm, which is attributed to an underfilling/overfilling of the grating grooves during the FIB milling process (mentioned in Sec. 4.3.2). A similar line trace in the optical amplitude image (Fig. 4.13e) shows that the optical amplitude is higher on the peaks and lower on the valleys of the grating. An underfilling or overfilling of the grooves leads to an overcoupling or undercoupling of SPPs due to the difference in the thickness of the metal layer. The SPPs propagating along the direction of the in-plane wave vector component of the -1^{st} diffracted order interferes with the in-plane wave vector component of the 0^{th} diffracted order, producing the modulated field pattern on the surface. The cosine of the phase of the optical field on the grating (Fig. 4.13c) shows abrupt phase jumps due to the interference between multiple plane waves propagating on the interface. Unlike the SPPs generated across the glass-gold transition region explained in Sec. 4.2.3, the spatial phase shift of the SPPs excited on the grating by varying the incident angle cannot be observed directly, since the diffracted orders have different spatial frequencies.

4.3.8 Reciprocal space analysis

A Fourier transform of the topography and the complex optical field (Fig. 4.13) are shown in Fig. 4.14. The Fourier image of the topography (Fig. 4.14a) shows that the different spatial frequencies are distributed symmetrically with respect to the zero frequency point. The Fourier image of the total optical field (Fig. 4.14b) shows fea-

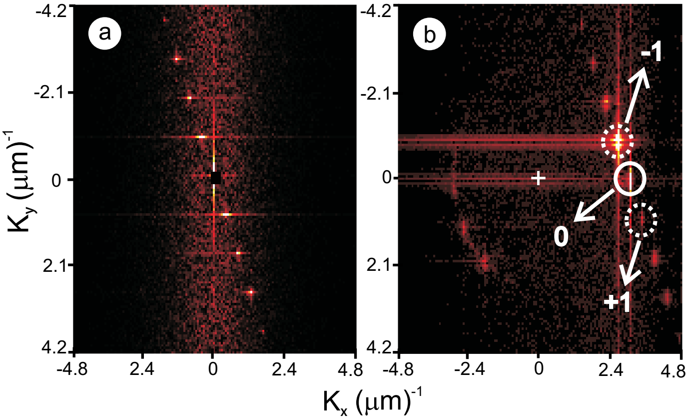

Figure 4.14: A two-dimensional Fourier Transform of the (a) the topography and (b) the complex optical field.

tures with different spatial frequencies. The -1^{st} diffracted order is the brightest spot due to the resonant coupling to SPPs. The magnitudes of the higher diffracted orders are relatively weak. The magnitude of the 0^{th} diffracted order relative to the peak magnitude in the -1^{st} diffracted order is 0.75; while that of the $+1^{st}$ and the -2^{nd} diffracted orders are 0.04 and 0.08, respectively. To obtain a precise extraction of the phase angle from the frequency domain image, zeros were added to the spatial domain image, increasing its size by a factor of 10 in both axes.

4.3.9 Phase extraction method

The shift in the phase of the -1^{st} diffracted order due to the resonant excitation of the SPPs can be extracted using the phase of the non-resonant $+1^{st}$ diffracted order as the reference. A pictorial representation of the phases of the incident and the diffracted orders upon excitation of SPPs via the -1^{st} diffracted order is shown in Fig. 4.15. For simplicity, higher diffracted orders are neglected. The phase of the

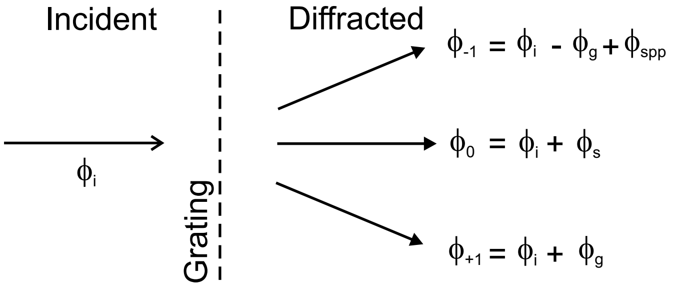

Figure 4.15: A pictorial representation of the diffraction of incident light with phase ϕ_i into diffracted orders 0, -1 and +1 with phases ϕ_0, ϕ_{-1}, and ϕ_{+1}, respectively. ϕ_g is the grating phase, and ϕ_{spp} is the resonant phase due to the excitation of SPPs. ϕ_s is the resonant phase in the 0^{th} order due to the SPPs scattered by the buried grating.

incident field is denoted as ϕ_i. The phase of the field that is measured in the -1^{st} diffracted order is given by

$$\phi_{-1} = \phi_\mathrm{i} - \phi_\mathrm{g} + \phi_\mathrm{spp}, \tag{4.8}$$

where ϕ_g is the static phase of the grating, and ϕ_spp is the resonant phase due to the excitation of SPPs. Similarly, the phase of the field that is measured in the $+1^{\mathrm{st}}$ order is given by

$$\phi_{+1} = \phi_\mathrm{i} + \phi_\mathrm{g}. \tag{4.9}$$

Using Eq. (4.8) and (4.9), the resonant phase in the -1^{st} diffracted order is obtained as

$$\phi_\mathrm{spp} = \phi_{-1} - \phi_{+1} + 2\phi_\mathrm{g}. \tag{4.10}$$

It might appear that since the value of the $\mathrm{k}_{\parallel(0)}$ is greater than k_spp, there should not be a resonant part in the phase ϕ_0 of the 0^{th} order field. However, coupling to the modulation at the glass-gold interface of the buried grating causes the SPPs in the -1^{st} order to couple to the 0^{th} order. Hence the phase in the 0^{th} order is given as

$$\phi_0 = \phi_\mathrm{i} + \phi_\mathrm{s}. \tag{4.11}$$

Using Eq. (4.9) and (4.11), the resonant phase, ϕ_s in the 0^{th} order is obtained as

$$\phi_\mathrm{s} = \phi_0 - \phi_{+1} + \phi_\mathrm{g}. \tag{4.12}$$

The grating phase (ϕ_g) is obtained from the Fourier transform of the topography image. The Fourier Transform of the complex optical field is used to extract the phases ϕ_0, ϕ_{-1} and ϕ_{+1} of the diffracted orders. Using Eq. (4.10) and (4.12), the resonant phase change in the -1^{st} and the 0^{th} diffracted orders are extracted.

4.3.10 Resonant phase shift on the grating

The phases ϕ_g, ϕ_0, ϕ_{-1}, and ϕ_{+1} are extracted for incident angles ranging from 47° to 50°. Using Eq. (4.10) and (4.12), the resonant phases ϕ_spp and ϕ_s are calculated and plotted against the incident angle in Fig. 4.16a, together with the difference between the theoretical phase changes shown in Fig. 4.11. A phase shift of 133° is observed, which is due to the resonant coupling to the SPPs and it matches with the theoretical phase shift. As observed in Sec. 4.2.4, an offset in the measured phase is observed compared to the theoretical phase plot, which is tentatively attributed to an interaction between the metal-coated probe and the gold surface. In addition to the resonant phase in the -1^{st} diffracted order, a phase change of 34° is measured in the 0^{th} diffracted order due to the SPPs that are scattered into the 0^{th} order via the modulation at the glass-gold interface.

Simultaneous far-field reflection measurement is used to cross-check the generation of the SPPs. Figure 4.16b shows a comparison between the reflection and the PSTM measurements. The absorption dip in the reflected intensity in the -1^{st} diffracted order, for the p-polarized incident beam, indicates the SPR angle as 48.5°. The distinct change in the phase of 133° is measured over the SPR range. The phase shift measured on the gold buried grating calculates [120] a Goos-Hänchen shift of 6.2 µm.

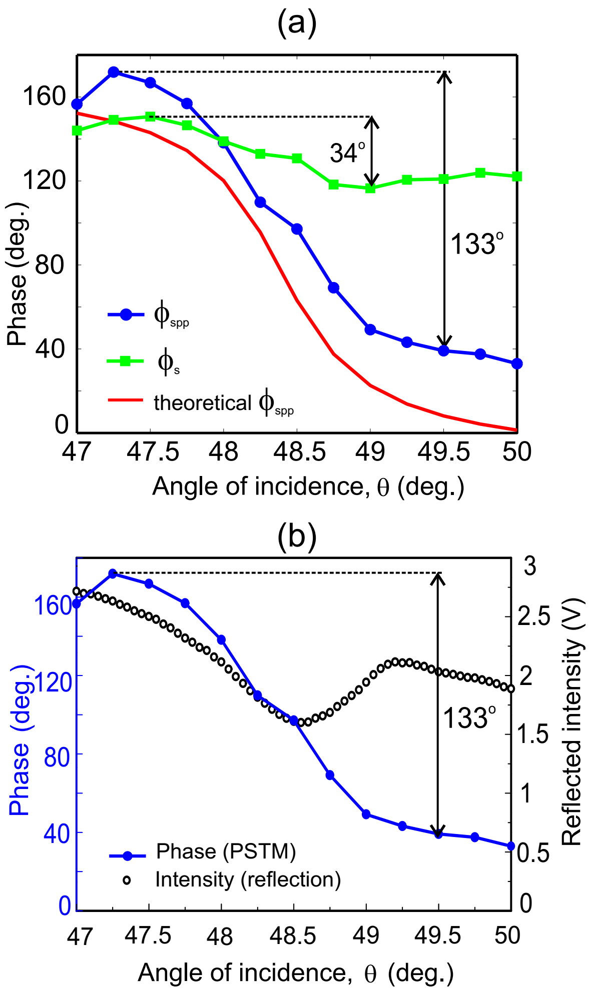

Figure 4.16: (a) Comparison of the theoretical and the experimental change in the resonant phase in the -1^{st} and the 0^{th} order diffracted light as a function of the incident angle. (b) Comparison between the near-field resonant phase shift in the -1^{st} diffracted order and the far-field reflected intensity in the -1^{st} order reflected light.

4.4 Conclusions

Near-field extractions of the phase shifts at surface plasmon resonance on a flat gold-air interface and a corrugated gold surface were presented. The shift in the spatial phase of evanescent waves on the glass-gold transition region as a function of incident angle has been visualized locally using a heterodyne interferometric PSTM. The spatial phase shift associated with the SPR shows an enhanced Goos-Hänchen shift of 3.5 μm. The change in the phase difference of the evanescent waves across the glass-gold transition region of the sample as a function of incident angle shows the combined effect of the GH effect and the generation of SPPs and agrees well with the theoretical predictions.

A phase extraction method has been presented to obtain the resonant phase change in the -1^{st} diffracted order at SPR on a gold buried grating. The non-resonant diffracted order has been used as a reference. The measured resonant phase shift matches with the theoretical phase. The scattering of the SPPs leads to a resonant phase shift in the 0^{th} diffracted order. The GH shift, corresponding to the phase shift in the -1^{st} diffracted order, on the grating is 6.2 μm. The near-field extraction of the resonant phase of the SPPs using the non-resonant diffracted order has been shown as a convenient way of measuring the phase of SPPs which can find application in grating-incorporated SPR sensors.

5

Exposed versus buried grating

5.1 Introduction

Surface Plasmon Resonance (SPR) sensors are mostly based on the Kretschmann-Raether configuration, where a shift in the resonance angle or wavelength is used to detect changes in the refractive index or thickness of a specimen layer. The Kretschmann-Raether configuration using a single incident wave vector couples to a single SPR. Coupling to multiple surface plasmon resonances make it possible to detect a range of materials using a single sensing device [126]. Moreover, the in-plane rotation of the grating is an additional parameter, that can be tuned through the SPR making a flexible SPR sensor. Multiple surface plasmon resonances can be excited by incorporating a grating in the Kretschmann-Raether configuration so that different diffracted orders can couple to SPPs. This chapter discusses a grating design to reduce the radiative damping of SPPs with the aim of finding application in sensing devices.

5.2 Grating arranged in Kretschmann-Raether configuration

The prism and the grating coupling schemes can be combined either to decouple the prism-coupled SPPs to radiation via the grating or to detect the grating-coupled SPPs via the leakage radiation emitted into the prism. Incorporating a grating in the Kretschmann-Raether configuration opens up flexible designs for applications ranging from sensing to waveguiding. In the Kretschmann-Raether configuration, a grating can be incorporated either at the metal-air interface or at the metal-prism interface. The former is called an exposed grating and the latter a buried grating. A third type of grating is a conformal one with a periodic corrugation on both the metal-air and the metal-prism interfaces in such a way that the thickness of the grating is constant throughout. Unlike the conformal grating, the SPP field intensities at the metal-air interface of the exposed and the buried gratings show an enhancement due to a strong coupling across the thin parts of the metal film [140].

SPPs can be excited at the metal-air interface or the metal-glass interface. For sensing applications, excitation of SPPs at the metal-air interface is desired so that the specimen will be in contact with the SPP field. Schematic of the exposed and the buried gratings with SPPs propagating on the metal-air interface are shown in are shown in Fig. 5.1a and 5.1b, respectively. In the case of the exposed grating, the SPPs propagate on the grating. The grating wave vector converts the SPPs back to light or scatters into other SPPs [32, 36, 44, 45]. For the buried grating, the SPPs propagate on the flat metal surface, which can reduce the radiative damping into the air space.

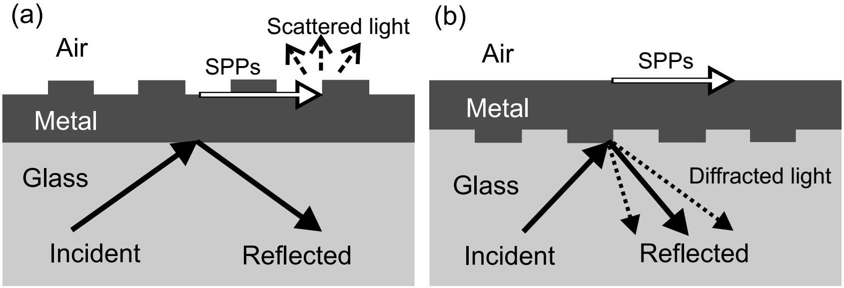

Figure 5.1: Illustration of SPPs propagating on the metal-air interface in (a) an exposed grating and (b) a buried grating.

The propagation length (L_{spp}) of the SPPs depends on the internal and radiative damping of SPPs. The internal damping is a characteristic of the metal and hence will be roughly same for both the gratings. However, the radiation damping will be different for the gratings due to the additional scattering of the SPPs propagating on the exposed grating surface. The buried grating can also scatter the SPPs due to the fact that the SPP field also extends into the metal. In this work, we discuss the radiative damping of SPPs into the air space for both the gratings.

The surface plasmon resonance has a Lorentzian (L) line profile given by

$$L(\theta) = \sum_{n=0,-1} \left\{ C_n \frac{(\frac{\Gamma_n}{2})^2}{(\theta-\theta_n)^2 + (\frac{\Gamma_n}{2})^2} \right\}, \tag{5.1}$$

where n=0,-1 correspond to the 0^{th} and the -1^{st} diffracted orders, Γ_n is the full width at half maximum (FWHM) of the Lorentzian distribution, θ_n is the incident angle at which SPR occurs and C_n is a constant that denotes the peak value of the intensity corresponding to the SPR. A smaller FWHM implies a sharper Lorentzian line profile for the surface plasmon resonance and a longer SPP propagation length. Furthermore, the sensitivity of SPR sensors increases by decreasing the FWHM of the resonance. A near-field experimental investigation of the SPPs excited on an exposed and a buried grating is presented. The FWHM of the surface plasmon resonances excited on a buried and an exposed grating are measured by detecting the optical amplitude in the near-field on the gratings for varying incident angles.

5.3 Fabrication

Exposed grating
A gold layer of thickness of 70 nm was deposited on a $15 \times 15 \times 0.15$ mm glass cover slip by electron-beam evaporation at a base pressure equal to 2×10^{-6} mbar. Using a Focused Ion Beam (FIB) in a dual-beam machine (FEI Nova nanolab 600), a one-dimensional grating of size 125 µm × 125 µm with a period of 1.65 µm, depth of 22.5 nm, and duty cycle of 0.5 was milled into the gold.

Buried grating
The buried grating was fabricated using a template-stripping technique [141], employed to make ultrasmooth metal films for scanning probe microscopy and plasmonics [52]. The different steps in the fabrication of the buried grating are shown in Fig. 5.2. The native oxide layer on a one-side polished silicon wafer ($< 100 >$) was removed by immersing the wafer in 1% HF solution for approximately one minute. To remove the residual HF, the wafer was rinsed thoroughly in deionized water (Quick Dump Rinser) until the conductivity was less than 0.1 µS/cm, and then dried in a flow of N_2. The wafer was mounted in a vacuum chamber within an hour to prevent further oxidation. When the pressure inside the vacuum chamber was 2×10^{-6}mbar, the wafer was sputter-cleaned in an argon atmosphere at 200 mA for 5 minutes. A 70 nm thick gold layer was deposited using electron-beam evaporation (Fig. 5.2a). A grating was milled into the gold using the FIB, with the same size, period, depth and duty cycle as used for the exposed grating. A drop of UV curable optical glue (Norland Blocking Adhesive NBA 107) was put on top of the grating and a clean glass cover slip was placed on top of the glue so that the glue is spread without any air bubbles trapped in between (Fig. 5.2b). The glue was cured by shining UV radiation (UV crosslinker spectolink) for 30 minutes from the glass side (Fig. 5.2c). After curing the glue, the edges of the cover slip were cut using a razor blade and a mechanical leverage was applied on one end of the coverslip. Due to poor adhesion of gold to the silicon wafer, the gold clings to the glass and easily detached from the wafer (Fig. 5.2d).

5.4 Scanning electron microscopic imaging

The gratings were examined under a Scanning Electron Microscope (SEM) by collecting the secondary electrons emitted from the sample.

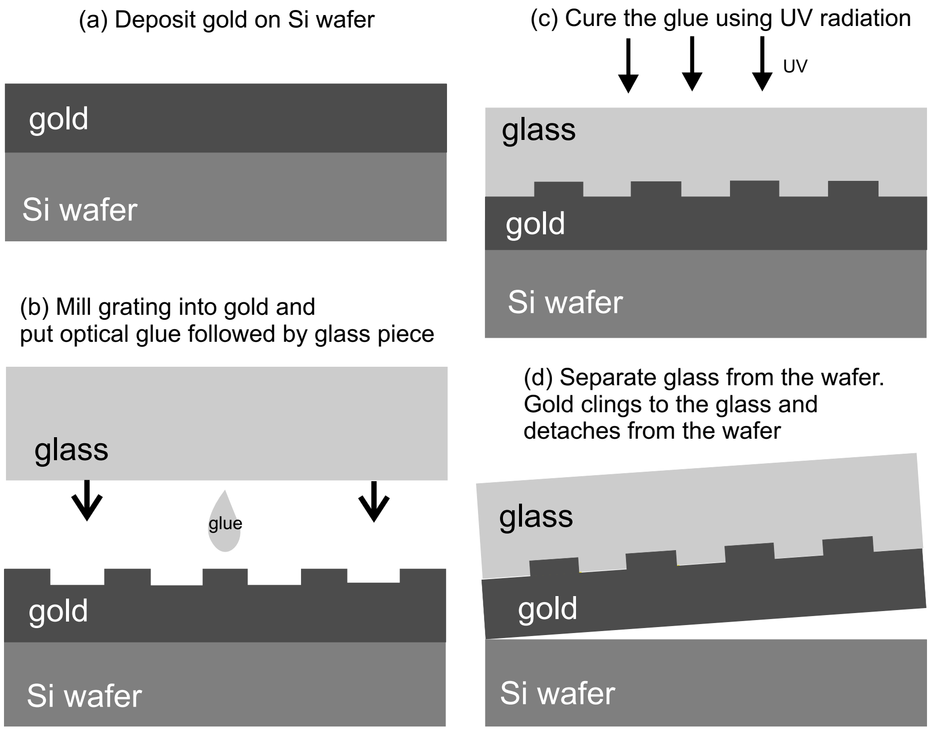

Figure 5.2: Fabrication of the buried grating.

Exposed grating
A SEM image of the grating is shown in Fig. 5.3. The grooves are 22.5 nm deep into the glass substrate. The poor contrast in the image is due to the low acceleration voltage (5kV) used to acquire the image.

Buried grating
Using the FIB, a rectangular hole was made into the sample. SEM images of the sample taken at two different acceleration voltages are shown in Fig. 5.4. The profile of the grating is slightly visible on the top edge of the hole shown in Fig. 5.4a. For a low acceleration voltage (5 kV), the secondary electrons are collected from the first few nanometers of the sample, which in our case is gold. When the acceleration voltage is increased to 30 kV, a periodic contrast is seen in the SEM image (Fig. 5.4b). This is due to the fact that the penetration depth of the incident electrons increases and the electrons are scattered by the grating buried in the interior of the sample. A prolonged exposure to the high energy electron beam was found to melt the optical glue and subsequently cracks were visible on the edges of the hole.

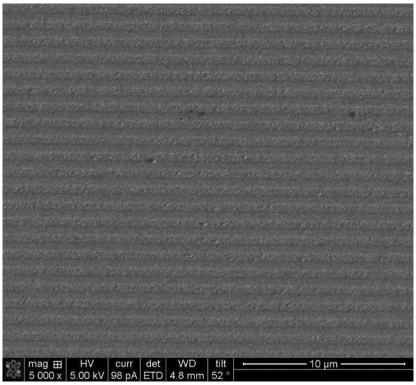

Figure 5.3: SEM image of a 22.5 nm deep grating milled into a 70 nm thick film of gold using a FIB.

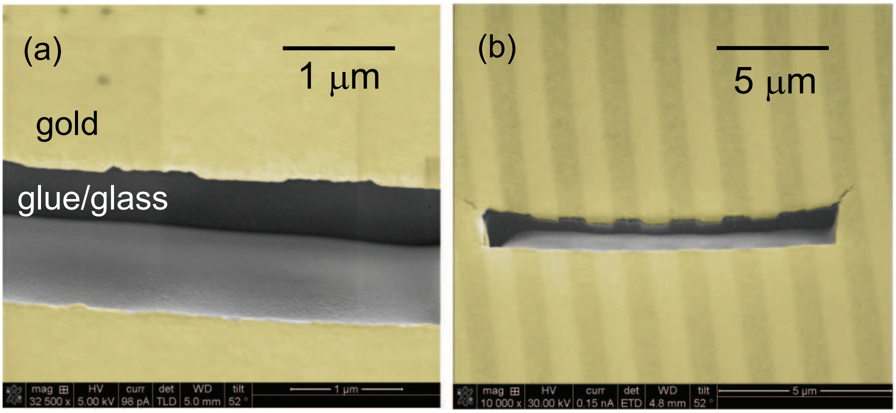

Figure 5.4: SEM images (false color) of the buried grating (sample is tilted by 52°) at acceleration voltages of (a) 5kV and (b) 30kV. The rectangular hole has been made by the FIB.

5.5 Excitation of multiple surface plasmon polaritons

The gratings were investigated in the near field using the heterodyne interferometric PSTM. Schematic representation of the sample configuration and the reciprocal space map to excite multiple SPPs are shown in Fig. 5.5a and 5.5b, respectively. The gratings were arranged in a conical mount (Fig.4.7b in Chapter 4) in which the grating wave vector k_g was rotated in-plane to make an angle β with $k_{\parallel}$. The $k_{\parallel}$ (corresponding to the free space wave length of 657.3 nm) was varied by tuning the incident angle θ. Two SPP modes were excited at the gold-air interface: the prism-coupled SPPs and the grating-coupled SPPs, as shown in Fig. 5.5b. The former was excited via the specularly reflected light (0^{th} order) and the latter via the -1^{st} order diffracted light. The in-plane wave vector of the $+1^{\text{st}}$ order diffracted light is higher than the value of the wave vector of SPPs at the gold-air interface and hence cannot couple to SPPs.

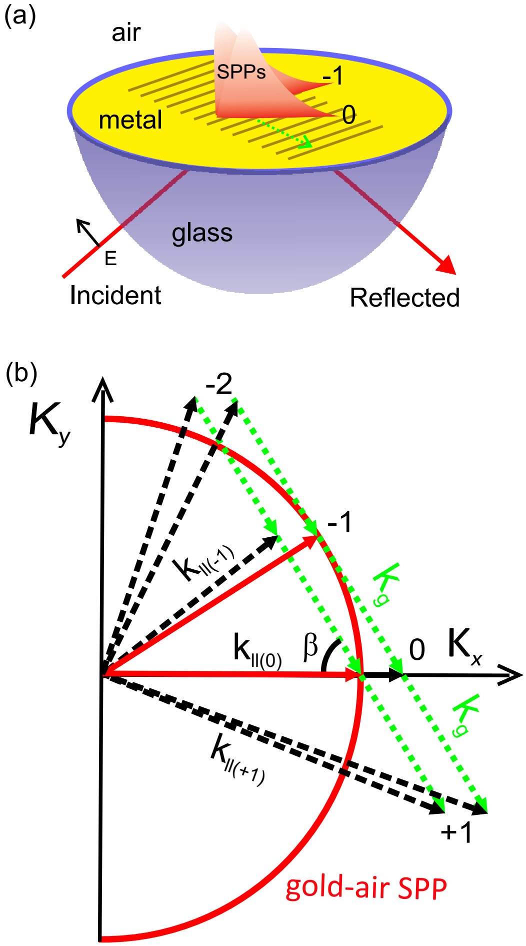

Figure 5.5: (a) A Grating arranged in a conical mount in the Kretschmann-Raether configuration and (b) the reciprocal space representation of the excitation of multiple SPP modes. The solid red curve denotes the momentum of the SPPs at the gold-air interface, the solid red arrows represent the wave vectors of the SPPs, the black dashed arrows represent the wave vectors of the diffracted light, and the dotted green arrows indicate the grating wave vectors.

5.5.1 Polarization state of the incident light

The incident light was set to p-polarization were the electric field vector lies in the plane of incidence (Fig. 5.5a). The optical amplitude at a fixed position on the exposed grating was detected, using the metal coated fiber tip placed in the near-field of the grating surface, for different incident angles. The corresponding intensity, after smoothing using a moving average method, is shown in Fig. 5.6a. Two peaks are visible: the prism-coupled SPR at 42.5° and the grating-coupled SPR at 45.7°. The peak corresponding to the prism-coupled SPR is higher than that of the grating-coupled SPR. The higher intensity in the prism-coupled SPR peaks are due to the fact that the orientation of the electric field vector is along the direction of the

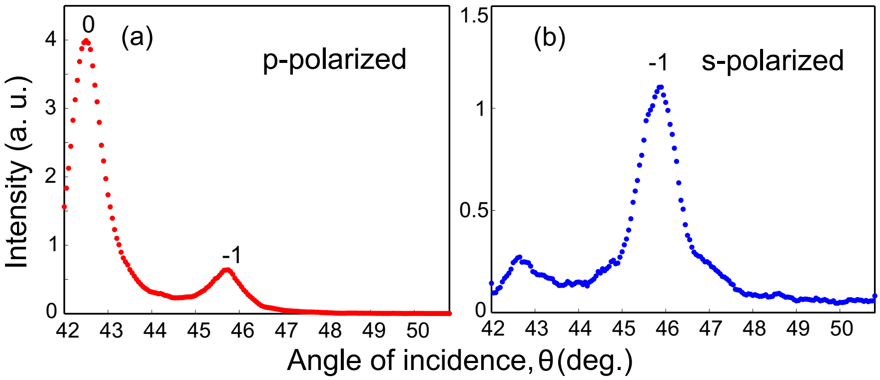

Figure 5.6: The intensity measured on the exposed grating as a function of the incident angle for (a) p-polarized and (b) s-polarized incident light.

prism-coupled SPPs (p-polarized) and the specularly reflected light (0^{th} order) carries more power than the -1^{st} order diffracted light. The intensity for s-polarized incident light is shown in Fig. 5.6b. Here the grating-coupled SPR peak rises significantly compared to the prism-coupled SPR peak because the incident electric field vector now has a component along the grating-coupled SPPs, but not along the prism-coupled SPPs. The peak corresponding to the prism-coupled SPPs is present due to polarization impurity of the incident light. An optimum grating coupling will be achieved when the electric field vector is oriented at an angle equal to the angle α that the grating-coupled SPPs makes with the plane of incidence [130, 131]. The angle α is given by

$$\alpha = \cos^{-1}\left\{\frac{\mathrm{k}_{\parallel}^2 + \mathrm{k}_{\mathrm{spp}}^2 - \mathrm{k}_{\mathrm{g}}^2}{2\mathrm{k}_{\parallel}\mathrm{k}_{\mathrm{spp}}}\right\}, \tag{5.2}$$

where $\mathrm{k}_{\mathrm{spp}}$ is the wave vector of the SPPs at the gold-air interface. The variation of α with the incident angle for which the grating-coupled SPPs are excited is shown in Fig. 5.7.

5.5.2 Full width at half maximum of the resonances

The PSTM tip was kept at a fixed position on the grating in the measurements of the FWHM of the surface plasmon resonances. For p-polarized incident light, the near-field optical amplitude on the exposed and the buried gratings were detected as a function of the incident angle θ. The corresponding intensities, after smoothing, are shown in Fig. 5.8. The experimental data are fitted to the Lorentzian function (L) given in Eq. (5.1). The fitting parameters are given in Table 5.1. The FWHM of the SPR in the case of the buried grating is reduced to 57% for the prism-coupled SPPs and 77% for the grating-coupled SPPs. The location and the FWHM of the SPRs are dependent on the real and imaginary parts of the complex dielectric constant of gold, respectively. A reduction in the FWHM of the SPR implies an increase in the propagation length of the SPPs. A reduced radiative scattering of the SPPs generated on the buried grating therefore also leads to a reduction in the

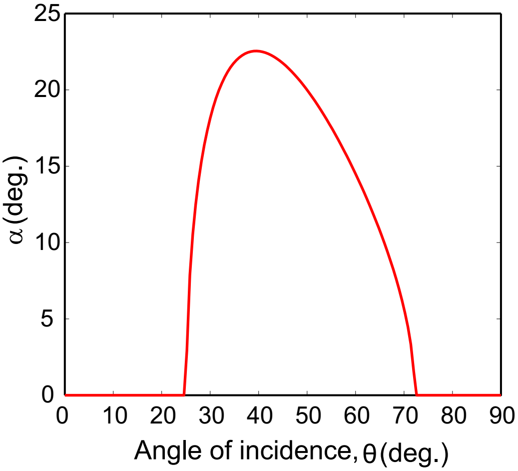

Figure 5.7: The variation of the angle α the grating-coupled SPPs make with the $k_{\parallel}$ as a function of the incident angle θ.

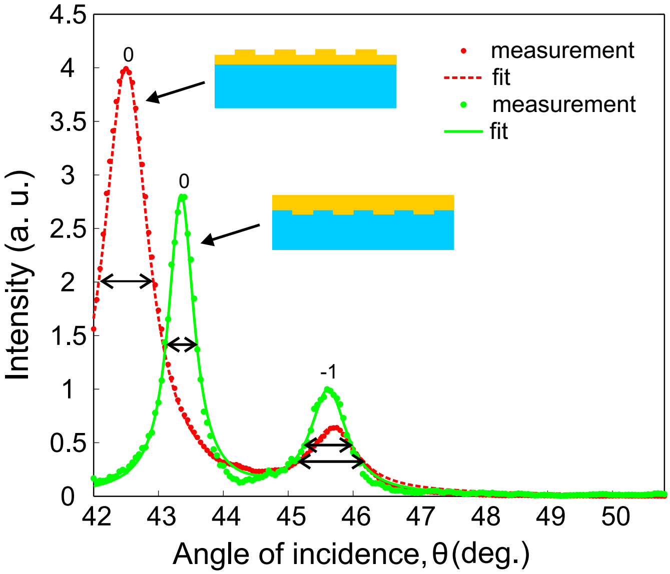

Figure 5.8: The intensities measured on the near-field of the exposed and the buried gratings. The solid and dashed lines are the lorentzian fits to the experimental values (dots). Insets show the schematic of the buried and the exposed gratings. The FWHM of the resonances are indicated by double-sided arrows.

FWHM of the SPR [32]. The shift in the position of the prism-coupled SPR by 0.9° for the buried grating might be due to a difference in the refractive index for the glue compared to the glass substrate [146]. For a 70 nm thick gold layer, a change in the refractive index of the glass prism by 0.026 corresponds to a displacement of 0.9° in the position of the SPR.

Table 5.1: The fitting parameters C_n, Γ_n and the SPR angles θ_n for 0^{th} and -1^{st} order resonances measured on the exposed and the buried gratings.

	Exposed grating		Buried grating	
n	0	−1	0	−1
C_n	3.99	0.58	2.79	0.97
Γ_n	0.84°	0.88°	0.48°	0.68°
θ_n	42.5°	45.7°	43.4°	45.6°

5.6 Decay of grating-coupled SPPs

The PSTM tip was raster scanned on the edge of the grating to detect the SPPs propagating beyond the grating. The size of the incident laser spot was bigger than the size of the grating and hence the incident light illuminated the grating and the surrounding flat gold surface. By measuring the amplitude and phase of the optical field using the heterodyne interferometric PSTM, the SPPs can be separated from the 0^{th} order evanescent waves.

Exposed grating
The incident angle was fixed at 45.7° to excite SPPs via the -1^{st} diffracted order. The PSTM images are shown in Fig. 5.9. Figures 5.9a, 5.9b and 5.9c show the topography after tilt correction [109], the optical amplitude and the cosine of the phase of the optical field, respectively. The optical amplitude is higher on the grating than outside the grating due to the excitation of SPPs. The SPPs propagate beyond the grating as an exponentially decaying wave.

Buried grating
The incident angle was fixed at 45.6° to excite SPPs via the -1^{st} diffracted order. The PSTM images are shown in Fig. 5.10. Figures 5.10a, 5.10b, and 5.10c show the topography, the optical amplitude and the cosine of the phase of the optical field, respectively. The topography of the template-stripped surface shows no residual modulation. The edge of the grating is not revealed in the topography; but is clear in the optical amplitude image.

5.7 SPP propagation length beyond the exposed grating

To separate the SPPs from the diffracted order and thereby to measure the propagation length of the SPPs, a two-dimensional Fourier transform analysis [104] of the PSTM images is performed. The Fourier transform of the complex optical field measured on the exposed grating (Fig. 5.9) is shown in Fig. 5.11a. An enlarged portion of the Fourier transform image is shown in Fig. 5.11b. Two prominent features are visible in the image: the 0^{th} and the -1^{st} order diffracted components. The intense feature in the image is the -1^{st} order which is due to the resonant coupling

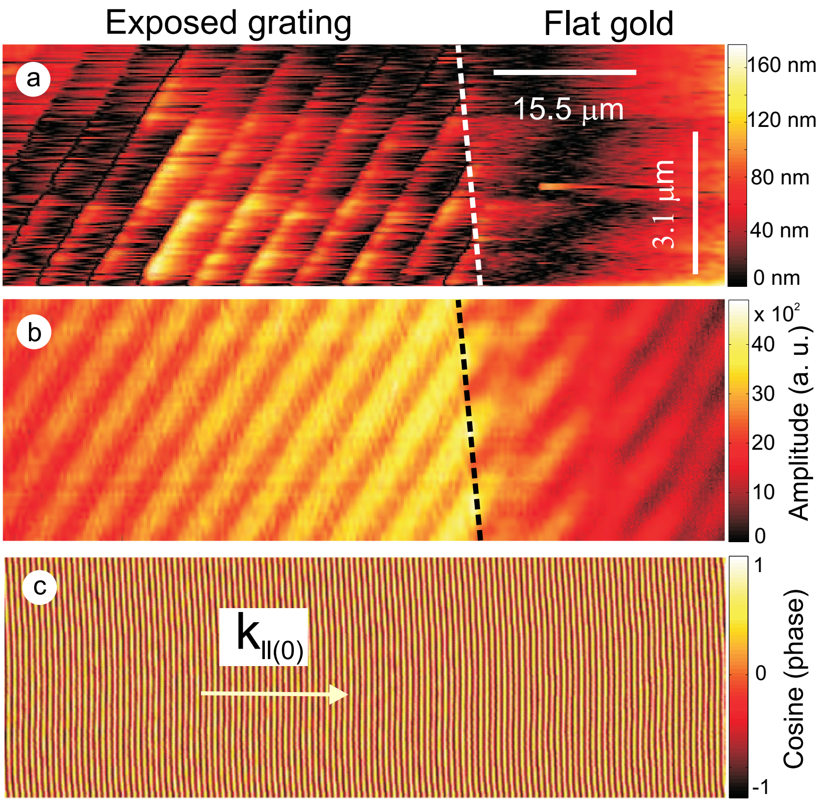

Figure 5.9: Interferometric PSTM measurements on the edge of the exposed grating. (a) The topography, (b) the amplitude of the optical field, and (c) the cosine of the phase of the optical field. The scan size is 78.6 µm×5.3 µm. The edge of the grating is denoted by the white and the black dashed lines in (a) and (b), respectively.

to the SPPs. In addition to the coupling to SPPs, the highest amplitude for the -1^{st} order can also be due to two other factors. First, a conical mount will break the diffraction symmetry and subsequently the diffracted orders will have different field strengths on the grating surface. Hence the magnitude of the -1^{st} order can be higher than that of the $+1^{st}$ diffracted order. Second, a difference in the coupling strength for the $+1^{st}$ and the -1^{st} diffracted orders into the tip of the PSTM has been attributed to a tilt of the tip [11]. But this is not the case in our measurements due to the fact that repeated measurements with new fiber tips showed a similar behavior. The former factor was clarified by detecting the reflected intensity in the -1^{st} reflected order, which showed a minimum due to the resonant excitation of SPPs.

In addition to the prominent features, a circular pattern is seen with respect to the zero frequency point in Fig. 5.11a, which corresponds to the SPPs that undergo directional scattering [32] by the surface roughness. The magnitude of the SPP wave vector has been preserved in the scattering process as is evident from the circular pattern of the scattered spatial frequencies. Interestingly, a comparatively higher amplitude is observed on the region of the circle which is situated diagonal to the

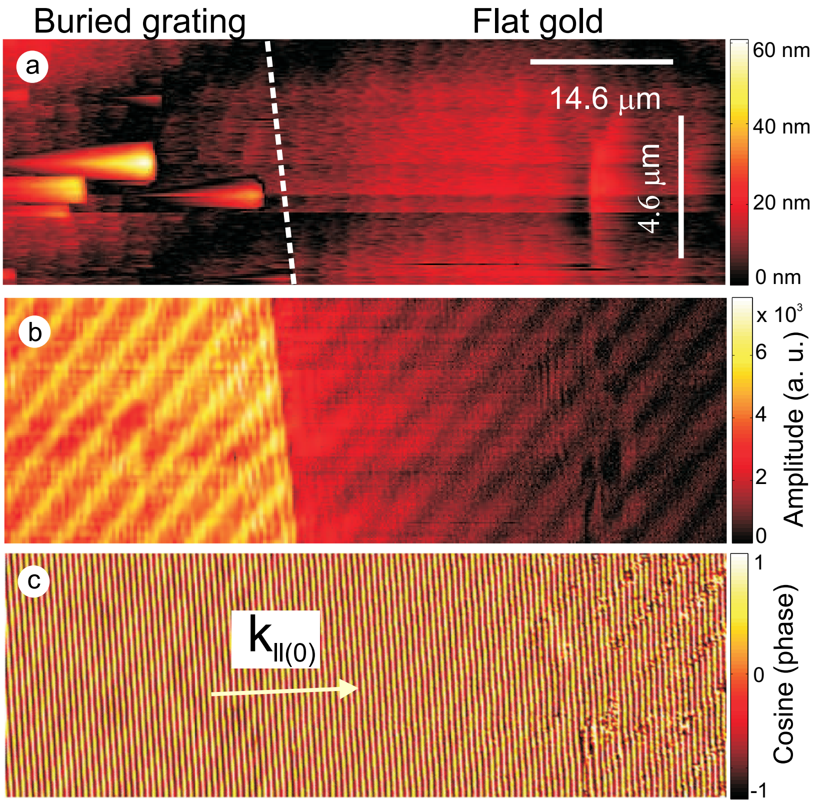

Figure 5.10: Interferometric PSTM measurements of the edge of the buried grating. (a) The topography, (b) the amplitude of the optical field, and (c) the cosine of the phase of the optical field. The scan size is 74.2 μm×7.9 μm. The edge of the grating is denoted by the white dashed line in (a).

-1^{st} diffracted order, which is attributed to the scattering of SPPs by the grating wave vector. The 0^{th} and the -1^{st} order features are filtered [104] to extract the SPPs. The magnitudes of the inverse Fourier transforms of the separated features give the optical amplitude images for the two diffracted orders and are shown in Fig. 5.11c and 5.11d. For both orders, the optical amplitude is higher on the grating than outside the grating. For the 0^{th} order, the higher optical amplitude on the grating is attributed to the different average thickness of the gold layer; the 22.5 nm deep grooves in the 70 nm thick gold layer increase the coupling strength. For the -1^{st} order, the optical amplitude increases on the grating due to the resonant excitation of the SPPs. The optical amplitude decreases away from the grating due to internal losses in the gold.

Line traces along the black dashed line in Fig. 5.11c and 5.11d are shown in Fig. 5.12. A linear fit to the intensity in the -1^{st} order yields a propagation length of 10.7 ± 0.6 μm along K_x (Fig. 5.12b). The SPPs propagate at an angle of 9.5° from the K_x axis. The propagation length along the direction of propagation of the SPPs is 10.8 ± 0.6 μm.

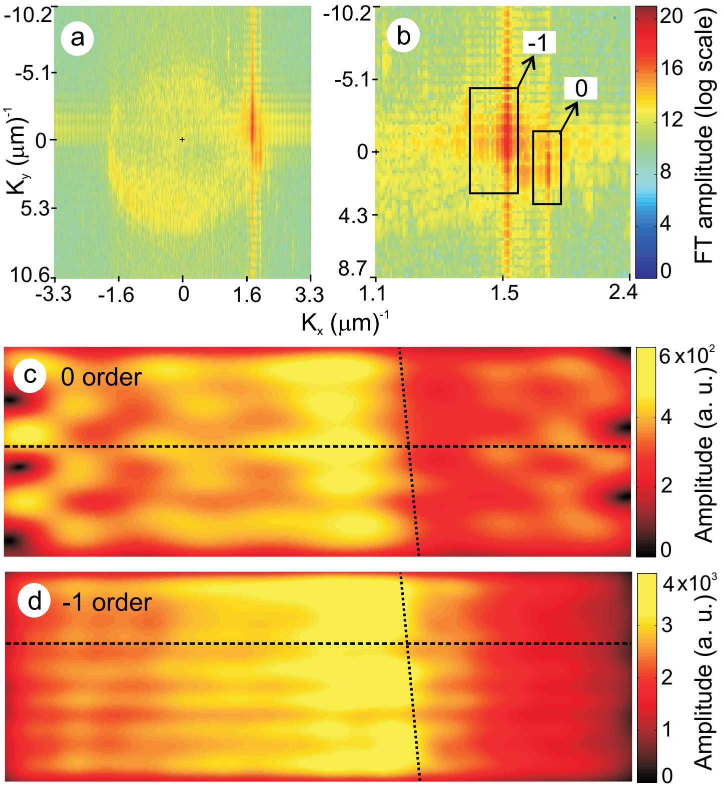

Figure 5.11: (a) The Fourier transform of the complex optical field measured on the edge of the exposed grating and (b) an enlarged portion of (a) showing the different features. The black boxes show the region selected for filtering. The magnitude of the inverse FT of the filtered spatial frequency region for (c) the 0^{th} order and (d) the -1^{st} order.

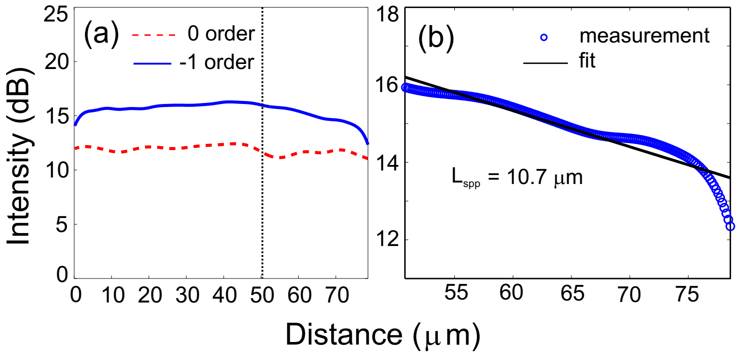

Figure 5.12: (a) Line trace along the black dashed line in the optical amplitude images. The edge of the grating is indicated by the black dotted line. (b) Linear fit to the intensity in the -1^{st} order beyond the grating. The intensities are plotted in a logarithmic scale.

5.8 SPP propagation length beyond the buried grating

The Fourier transform of the total field measured on the buried grating (Fig. 5.10) is shown in Fig. 5.13a. The circular pattern corresponding to the scattered SPPs observed in Fig. 5.11a for the exposed grating is absent for the buried grating. An enlarged portion of the Fourier transform image is shown in Fig. 5.13b. Four prominent features are visible in the image: 0^{th}, $+1^{st}$, -1^{st}, and -2^{nd} order diffracted components. As for the exposed grating, the intense spot corresponds to the -1^{st}

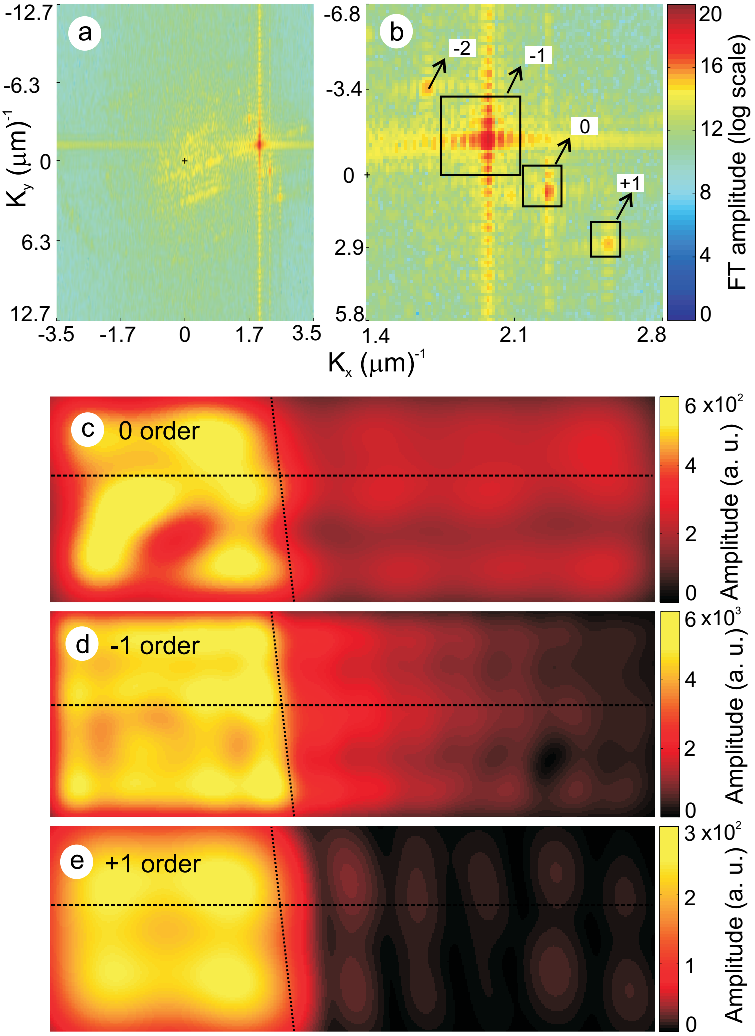

Figure 5.13: (a) The Fourier transform of the complex optical field measured on the edge of the buried grating and (b) an enlarged portion of (a) showing the different features. The black boxes show the region selected for filtering. The magnitude of the inverse FT of the filtered spatial frequency region for (c) the 0^{th}, (d) the -1^{st}, and (e) the $+1^{st}$ orders. The edge of the grating is indicated by the black dotted line.

order which is due to the resonant coupling to the SPPs. The 0th, +1st, and −1st features are filtered out separately and the magnitudes of the inverse Fourier transforms of the features are shown in Fig. 5.13c, 5.13d, and 5.13e, respectively. All the three orders have higher intensities on the grating than outside the grating. The 0th order evanescent wave (Fig. 5.13c) behaves similar as on the exposed grating. The +1st order (Fig. 5.13e) does not couple to SPPs since its momentum is higher than the SPP momentum and hence the optical amplitude drops to zero outside the grating.

Line traces taken along the black dashed lines for the three different orders are shown in Fig. 5.14. The intensity in the −1st diffracted order is the highest on the

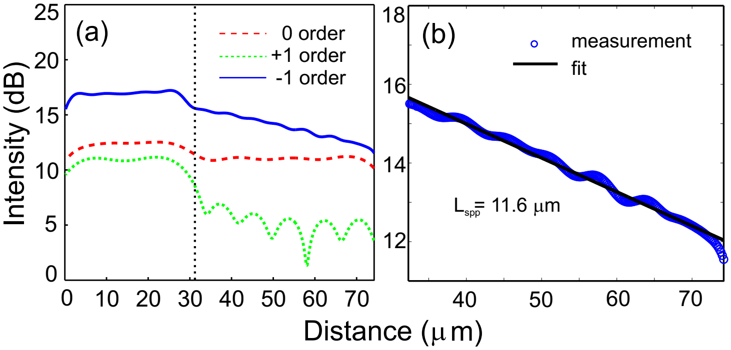

Figure 5.14: (a) Line traces along the black dashed line for the three diffracted orders shown in Fig. 5.13. The edge of the grating is indicated by the black dotted line. (b) Linear fit to the −1st order beyond the grating. The intensities are plotted in a logarithmic scale.

grating due to the resonant excitation of the SPPs. The SPPs decay beyond the grating due to the internal losses in the metal (Fig. 5.13d). A linear fit to the intensity in the −1st order yields the propagation length of 11.6 ± 0.1 μm as shown in Fig. 5.13b. The SPPs propagate at angle of 13.7° from the K_x axis. The propagation length along the direction of the SPPs is 11.9 ± 0.1 μm.

The propagation length of SPPs on an ideal gold surface of negligible radiation damping and scattering losses [32] is 15 μm with dielectric constant of gold taken from Johnson and Christy [31]. The SPP propagation lengths measured on the template-stripped surface of the buried grating and the evaporated gold surface of the exposed grating are close to the calculated propagation length. The reduction in the FWHM is related to the surface plasmon resonances measured on the buried grating, whereas the SPP propagation length was measured outside the grating. The significant reduction in the FWHM of the surface plasmon resonances for the buried grating can be attributed to a reduced directional scattering of SPPs, as is evident in the Fourier transform image shown in Fig. 5.13a. The buried grating with a significant reduction in the FWHM of the surface plasmon resonances can improve the sensitivity of grating-incorporated SPR sensors.

5.9 Applications

5.9.1 Sensing

A SPR sensor is a label-free sensing device capable of detecting bio-chemical molecules [5] and monitoring real-time interaction in molecules [62]. The field enhancement on the sensor's metal surface due to the excitation of the SPPs implies that a small variation in the refractive index can perturb the SPP field [125]. The dependance of the SPP field on small changes in the near field of the metal surface determines the sensitivity of a SPR sensor. In this section, the effects of a buried and an exposed grating on the sensitivity of a SPR sensor are studied.

The sensitivity of a SPR sensor can be represented by its figure of merit. The Figure of Merit (FOM) of a sensor can be defined as the ratio of the rate of change of SPR angle θ_n to the FWHM of the SPR resonance given by

$$\mathrm{FOM} = \frac{\frac{d\theta_\mathrm{n}}{d\mathrm{n}}}{\mathrm{FWHM}}, \tag{5.3}$$

where n is the refractive index of the medium in contact with the SPPs on the metal surface (or the specimen). Calculations [133] based on rigorous coupled wave analysis [134] were performed on an exposed and a buried grating with the grating parameters taken from the fabricated gratings. The diffraction efficiencies in the 0^{th} order light reflected off the gratings, as a function of the incident angle, for different values of the refractive indices are shown in Fig. 5.15. For both gratings, the SPR angle increases with the refractive index, as expected. The depth of the SPR dip for the exposed grating is observed to fluctuate with the refractive index. For the buried grating, the depth of the SPR dip remains constant for refractive indices below 1.3. Figures 5.16a - 5.16c show the variation of the SPR angle, the FWHM, and the FOM for different refractive indices.

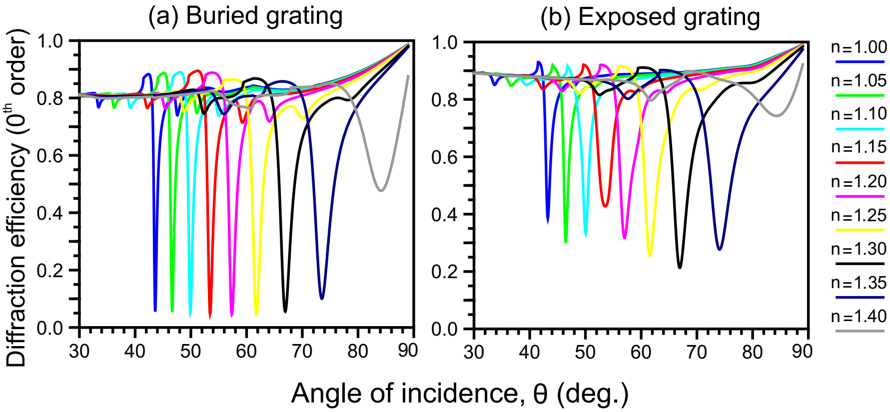

Figure 5.15: Calculated diffraction efficiency in the 0^{th} order reflected beam in (a) a buried grating and (b) an exposed grating.

The variation of the SPR angle with the refractive index shows that the slope for the exposed and the buried gratings are almost the same. The variation of the

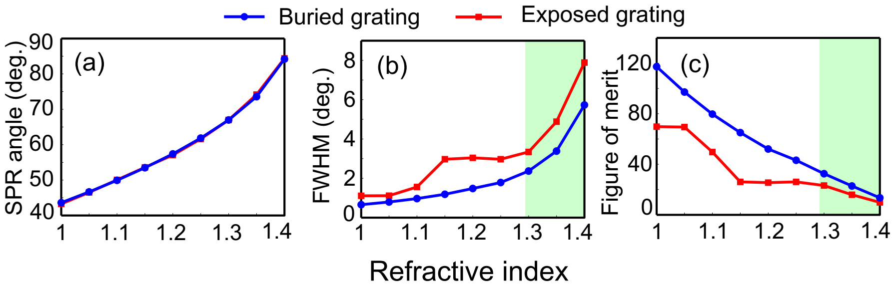

Figure 5.16: The influence of the refractive index of the medium in contact with the SPPs on (a) the SPR angle, (b) the FWHM, and (c) the FOM. The bio-relevant region is shaded in the plots.

FWHM of the resonances with the refractive indices shows an increasing trend for the gratings (Fig. 5.16b). Interestingly the exposed grating shows an increase in the FWHM for a refractive index of 1.15 and remains constant until the refractive index reaches 1.3. Thereafter, both gratings show a similar increasing trend. The FOM for the two gratings [Eq. (5.3)] is shown in Fig. 5.16c. For a refractive index of unity, the FOM is 70 for the exposed grating and is 117 for the buried grating. A figure of merit of 85 has been reported at a refractive index of 1.52 for a grating-incorporated SPR sensor [136]. In both exposed and buried gratings, a refractive index higher than 1.35, increases and widens the SPR dip which is attributed to the fact that the refractive index of the specimen approaches to the refractive index of the glass substrate (1.51). The refractive index range of 1.3 to 1.4 is applicable to bio-molecules [142]. The higher FOM observed for the buried grating when compared to the exposed grating, at the refractive index of 1.3, can improve the sensitivity of SPR bio-sensors.

5.9.2 Nanofocusing

A phase-matched exposed grating has been used previously to focus SPPs and an increased scattering of the SPPs was observed, which can decrease the propagation length of SPPs. [8]. The SPPs generated on the gold-air interface of a grating propagate towards the center of the grating using a non-collinear phase matching scheme as shown in Fig. 5.17. By burying the phase-matched grating, the radiative damping of SPPs can be reduced, so that the SPPs are focused with less scattering.

One promising application of a phase-matched buried grating is in the excitation of SPPs for confinement to nanoscale dimension by using a tapered waveguide [143, 144]. The SPPs generated and focused by the buried phase matched grating can be focused further to the apex of the tapered waveguide as depicted in Fig. 5.18. Both two-dimensional [17, 143] and three-dimensional tapered waveguides [42, 145] have been demonstrated for SPP confinement. In the three-dimensional confinement of SPPs, the coupling to SPPs has been achieved by periodic grooves milled on the metallic waveguide. By using a phase-matched buried grating, a pattering of the waveguide can be avoided, which could reduce the scattering of SPPs propagating towards the apex of the waveguide.

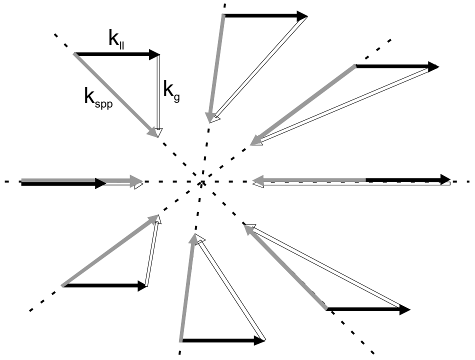

Figure 5.17: Non-collinear phase matching mechanism to focus the SPPs. The black solid arrows indicate the in-plane wave vector of the incident light for a fixed incident angle, the black open arrows denote the grating wave vectors, and the grey arrows denote the SPP wave vector (converging towards the center).

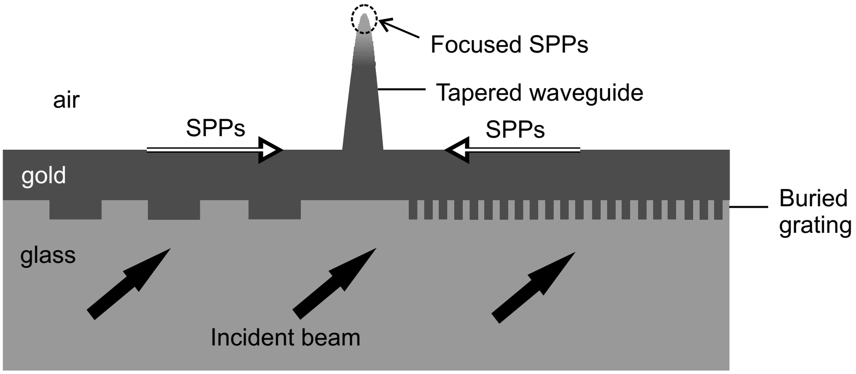

Figure 5.18: Cross sectional view of a phase-matched buried grating in combination with a tapered waveguide to achieve three-dimensional nanofocusing of SPPs.

5.10 Conclusions

An experimental investigation of the effect of a grating on the FWHM of the surface plasmon resonance has been presented. An exposed and a buried grating have been investigated in the near-field using a heterodyne interferometric PSTM. For a fixed position of the PSTM tip on the grating, the full width at half maximum of the SPR on the buried grating is measured to be significantly lower than that on the exposed grating. A considerable reduction in the SPP scattering on the buried grating has been observed by comparing the two-dimensional Fourier transform images of the complex optical field measured on the gratings. The propagation lengths of SPPs measured beyond the gratings have been found to be close to the calculated propagation length on an ideal gold surface. The significant reduction in the FWHM might indicate that the buried grating particularly reduces radiative damping of SPPs into the air space and hence increases the SPP propagation length.

Furthermore, a theoretical study based on RCWA simulations has been performed on both buried and exposed gratings. A higher FOM has been observed for the buried grating at a bio-relevant refractive index of 1.3. The buried grating has shown a large reduction in the FWHM of the surface plasmon resonances in the experiments and a higher FOM in simulations compared to the exposed grating, which might improve the sensitivity of grating-incorporated SPR sensors. In addition, a phase-matched buried grating in combination with a tapered waveguide has been proposed to focus SPPs in three-dimensions.

Bibliography

[1] I. Newton, *Opticks*, Dover Publications (1952).

[2] N. J. Harrick, *Internal reflection spectroscopy,* 0-470-35250-7, Interscience Publishers (1967).

[3] R. H. Ritchie, *Plasma losses by fast electrons in thin films,* Phys. Rev. **1**, 874–881 (1957).

[4] E. Kretschmann and H. Raether, *Radiative deacy of nonradiative surface plasmons excited by light,* Z. Naturforsch. A **23**, 2135–2136 (1968).

[5] J. Homola, S. S. Yee, and G. Gauglitz, *Surface plasmon resonance sensors: review,* Sensor. Actuat. B-Chem. **54**, 3–15 (1999).

[6] P. Dawson, K. W. Smith, F. Defornel, and J. P. Goudonnet, *Imaging of surface-plasmon launch and propagation using a photon scanning tunneling microscope,* Ultramicroscopy **57**, 287–292 (1995).

[7] R. W. Wood, *On a remarkable case of uneven distribution of light in a diffraction grating spectrum,* Proc. Phys. Soc. London **18**, 269 (1902).

[8] H. L. Offerhaus, B. van den Bergen, M. Escalante, F. B. Segerink, J. P. Korterik, and N. F. van Hulst, *Creating focused plasmons by noncollinear phasematching on functional gratings,* Nano Lett. **5**, 2144–2148 (2005).

[9] W. L. Barnes, T. W. Preist, S. C. Kitson, and J. R. Sambles, *Physical origin of photonic energy gaps in the propagation of surface plasmons on gratings,* Phys. Rev. B **54**, 6227–6244 (1996).

[10] P. Dawson, B. A. F. Puygranier, and J. P. Goudonnet, *Surface plasmon polariton propagation length: A direct comparison using photon scanning tunneling microscopy and attenuated total reflection,* Phys. Rev. B **63**, 205410 (2001).

[11] M. Sandtke and L. Kuipers, *Spatial distribution and near-field coupling of surface plasmon polariton Bloch modes,* Phys. Rev. B **77**, 235439 (2008).

[12] P. Dawson, F. Defornel, and J. P. Goudonnet, *Imaging of surface-plasmon propagation and edge interaction using a photon scanning tunneling microscope,* Phys. Rev. Lett. **72**, 2927–2930 (1994).

[13] J. C. Weeber, J. R. Krenn, A. Dereux, B. Lamprecht, Y. Lacroute, and J. P. Goudonnet, *Near-field observation of surface plasmon polariton propagation on thin metal stripes,* Phys. Rev. B **64**, 045411 (2001).

[14] K. H. Chen, J. H. Chen, and J. Y. Lin, *Comparison of kretschmann-raether configuration angular and thickness regimes with phase-difference shift for measuring changes in refractive index,* Opt. Eng. **45**, 023803 (2006).

[15] H. P. Ho, W. W. Lam, and S. Y. Wu, *Surface plasmon resonance sensor based on the measurement of differential phase,* Rev. Sci. Instrum. **73**, 3534–3539 (2002).

[16] L. L. Yin, V. K. Vlasko-Vlasov, J. Pearson, J. M. Hiller, J. Hua, U. Welp, D. E. Brown, and C. W. Kimball, *Subwavelength focusing and guiding of surface plasmons,* Nano Lett. **5**, 1399–1402 (2005).

[17] E. Verhagen, A. Polman, and L. Kuipers, *Nanofocusing in laterally tapered plasmonic waveguides,* Opt. Express **16**, 45–57 (2008).

[18] F. Goos and H. Hänchen, *Ein neuer und fundamentales versuch zur total reflexion,* Ann. Phys **1**, 333–345 (1947).

[19] K. Artmann, *Berechnung der seitenversetzung des totalreflektierten strahles,* Annalen Der Physik **2**, 87–102 (1948).

[20] F. I. Baida, D. V. Labeke, and J. M. Vigoureux, *Numerical study of the displacement of a three-dimensional gaussian beam transmitted at total internal reflection. near-field applications,* J. Opt. Soc. Am. A **17**, 858–866 (2000).

[21] M. Merano, A. Aiello, G. W. 't Hooft, M. P. van Exter, E. R. Eliel, and J. P. Woerdman, *Observation of goos-hänchen shifts in metallic reflection,* Opt. Express **15**, 15928–15934 (2007).

[22] S. G. Nelson, K. S. Johnston, and S. S. Yee, *High sensitivity surface plasmon resonance sensor based on phase detection,* Sensor. Actuat. B-Chem. **35**, 187–191 (1996).

[23] P. I. Nikitin, A. A. Beloglazov, V. E. Kochergin, M. V. Valeiko, and T. I. Ksenevich, *Surface plasmon resonance interferometry for biological and chemical sensing,* Sensor. Actuat. B-Chem. **54**, 43–50 (1999).

[24] H. P. Chiang, J. L. Lin, and Z. W. Chen, *High sensitivity surface plasmon resonance sensor based on phase interrogation at optimal incident wavelengths,* Appl. Phys. Lett. **88**, 141105 (2006).

[25] W. L. Barnes, *Surface plasmon-polariton length scales: a route to sub-wavelength optics,* J. Opt. A-Pure Appl. Opt. **8**, S87–S93 (2006).

[26] A. M. Fox, *Optical properties of Solids*, 0-19-850613-9, Oxford university Press, USA (2002).

[27] K. A. Willets and R. P. V. Duyne, *Localized surface plasmon resonance spectroscopy and sensing,* Ann. Rev. Phys. Chem. **58**, 267–297 (2007).

[28] S. A. Maier, *Plasmonics: Fundamentals and Applications*, 978-0387331508, Springer (2007).

[29] E. Burstein, W. P. Chen, Y. J. Chen, and A. Hartstein, *Surface polaritons - propagating electromagnetic modes at interfaces,* J. Vac. Sci. Technol. **11**, 1004–1019 (1974).

[30] U. Fano, *The theory of anomalous diffraction gratings and of quasi-stationary waves on metallic surfaces(sommerfeld's waves),* J. Opt. Soc. Am. **31**, 213–222 (1941).

[31] P. B. Johnson and R. W. Christy, *Optical-constants of noble-metals,* Phys. Rev. B **6**, 4370–4379 (1972).

[32] H. Raether, *Surface Plasmons on Smooth and Rough Surfaces and on Grating,* 3-540-17363-3, Springer, Berlin (1988).

[33] B. Hecht, H. Bielefeldt, L. Novotny, Y. Inouye, and D. W. Pohl, *Local excitation, scattering, and interference of surface plasmons,* Phys. Rev. Lett. **77**, 1889–1892 (1996).

[34] A. Otto, *Excitation of nonradiative surface plasma waves in silver by method of frustrated total reflection,* Z. Fur Physik **216**, 398 (1968).

[35] L. Salomon, F. de Fornel, and P. M. Adam, *Analysis of the near field and the far field diffracted by a metallized grating at and beyond the plasmon resonance,* J. Opt. Soc. Am. A **16**, 2695–2704 (1999).

[36] P. T. Worthing and W. L. Barnes, *Coupling efficiency of surface plasmon polaritons to radiation using a corrugated surface; angular dependence,* J. Mod. Optic. **49**, 1453–1462 (2002).

[37] Z. Chen, I. R. Hooper, and J. R. Sambles, *Strongly coupled surface plasmons on thin shallow metallic gratings,* Phys. Rev. B **77**, 161405 (2008).

[38] C. E. Wheeler, E. T. Arakawa, and R. H. Ritchie, *Photon excitation of surface plasmons in diffraction gratings - effect of groove depth and spacing,* Phys. Rev. B **13**, 2372–2376 (1976).

[39] M. G. Weber and D. L. Mills, *Grating-induced cross coupling of surface-polaritons,* Phys. Rev. B **32**, 5057–5061 (1985).

[40] I. Pockrand, *Coupling of surface plasma-oscillations in thin periodically corrugated silver films,* Opt. Commun. **13**, 311–313 (1975).

[41] Z. W. Liu, Q. H. Wei, and X. Zhang, *Surface plasmon interference nanolithography,* Nano Lett. **5**, 957–961 (2005).

[42] C. Ropers, C. C. Neacsu, T. Elsaesser, M. Albrecht, M. B. Raschke, and C. Lienau, *Grating-coupling of surface plasmons onto metallic tips: A nanoconfined light source,* Nano Lett. **7**, 2784–2788 (2007).

[43] W. L. Barnes, A. Dereux, and T. W. Ebbesen, *Surface plasmon subwavelength optics,* Nature **424**, 824–830 (2003).

[44] M. Kreiter, J. Oster, R. Sambles, S. Herminghaus, S. Mittler-Neher, and W. Knoll, *Thermally induced emission of light from a metallic diffraction grating, mediated by surface plasmons,* Opt. Commun. **168**, 117–122 (1999).

[45] S. Park, G. Lee, S. H. Song, C. H. Oh, and P. S. Kim, *Resonant coupling of surface plasmons to radiation modes by use of dielectric gratings,* Opt. Lett. **28**, 1870–1872 (2003).

[46] Y. Y. Teng and E. A. Stern, *Plasma radiation from metal grating surfaces,* Phys. Rev. Lett. **19**, 511 (1967).

[47] P. Berini, R. Charbonneau, and N. Lahoud, *Long-range surface plasmons on ultrathin membranes,* Nano Lett. **7**, 1376–1380 (2007).

[48] M. van Exter and A. Lagendijk, *Ultrashort surface-plasmon and phonon dynamics,* Phys. Rev. Lett. **60**, 49–52 (1988).

[49] R. C. Reddick, R. J. Warmack, and T. L. Ferrell, *New form of scanning optical microscopy,* Phys. Rev. B **39**, 767–770 (1989).

[50] E. Devaux, T. W. Ebbesen, J. C. Weeber, and A. Dereux, *Launching and decoupling surface plasmons via micro-gratings,* Appl. Phys. Lett. **83**, 4936–4938 (2003).

[51] V. V. Temnov, U. Woggon, J. Dintinger, E. Devaux, and T. W. Ebbesen, *Surface plasmon interferometry: measuring group velocity of surface plasmons,* Opt. Lett. **32**, 1235–1237 (2007).

[52] P. Nagpal, N. C. Lindquist, S. H. Oh, and D. J. Norris, *Ultrasmooth patterned metals for plasmonics and metamaterials,* Science **325**, 594–597 (2009).

[53] H. Ditlbacher, J. R. Krenn, N. Felidj, B. Lamprecht, G. Schider, M. Salerno, A. Leitner, and F. R. Aussenegg, *Fluorescence imaging of surface plasmon fields,* Appl. Phys. Lett. **80**, 404–406 (2002).

[54] T. Inagaki, K. Kagami, and E. T. Arakawa, *Photo-acoustic study of surface-plasmons in metals,* Appl. Optics **21**, 949–954 (1982).

[55] D. Heitmann, *Radiative decay of surface-plasmons excited by fast electrons on periodically modulated silver surfaces,* J. Phys. C-Solid State **10**, 397–405 (1977).

[56] B. A. Sexton, B. N. Feltis, and T. J. Davis, *Characterisation of gold surface plasmon resonance sensor substrates,* Sensor. Actuat. A-Phys. **141**, 471–475 (2008).

[57] A. Bouhelier and G. P. Wiederrecht, *Surface plasmon rainbow jets,* Opt. Lett. **30**, 884–886 (2005).

[58] A. Giannattasio and W. L. Barnes, *Direct observation of surface plasmon-polariton dispersion,* Opt. Express **13**, 428–434 (2005).

[59] I. H. El-Sayed, X. H. Huang, and M. A. El-Sayed, *Surface plasmon resonance scattering and absorption of anti-egfr antibody conjugated gold nanoparticles in cancer diagnostics: Applications in oral cancer,* Nano Lett. **5**, 829–834 (2005).

[60] P. Zijlstra, J. W. M. Chon, and M. Gu, *Five-dimensional optical recording mediated by surface plasmons in gold nanorods,* Nature **459**, 410–413 (2009).

[61] F. J. Haug, T. Soderstrom, O. Cubero, V. Terrazzoni-Daudrix, and C. Ballif, *Plasmonic absorption in textured silver back reflectors of thin film solar cells,* J. Appl. Phys. **104**, 064509 (2008).

[62] R. J. Green, R. A. Frazier, K. M. Shakesheff, M. C. Davies, C. J. Roberts, and S. J. B. Tendler, *Surface plasmon resonance analysis of dynamic biological interactions with biomaterials,* Biomaterials **21**, 1823–1835 (2000).

[63] T. Kan, N. Tsujiuchi, E. Iwase, K. Matsumoto, and I. Shimoyama, *Planar near-infrared surface plasmon resonance sensor with si prism and grating coupler,* Sensor. Actuat. B-Chem. **144**, 295–300 (2010).

[64] K. Kneipp, Y. Wang, H. Kneipp, L. T. Perelman, I. Itzkan, R. Dasari, and M. S. Feld, *Single molecule detection using surface-enhanced raman scattering (sers),* Phys. Rev. Lett. **78**, 1667–1670 (1997).

[65] Y. Lu, G. L. Liu, J. Kim, Y. X. Mejia, and L. P. Lee, *Nanophotonic crescent moon structures with sharp edge for ultrasensitive biomolecular detection by local electromagnetic field enhancement effect,* Nano Lett. **5**, 119–124 (2005).

[66] T. Vo-Dinh, L. R. Allain, and D. L. Stokes, *Cancer gene detection using surface-enhanced raman scattering (sers),* J. Raman Spectr. **33**, 511–516 (2002).

[67] D. P. O'Neal, L. R. Hirsch, N. J. Halas, J. D. Payne, and J. L. West, *Photo-thermal tumor ablation in mice using near infrared-absorbing nanoparticles,* Cancer Lett. **209**, 171–176 (2004).

[68] C. Loo, A. Lowery, N. Halas, J. West, and R. Drezek, *Immunotargeted nanoshells for integrated cancer imaging and therapy,* Nano Lett. **5**, 709–711 (2005).

[69] H. Ditlbacher, J. R. Krenn, G. Schider, A. Leitner, and F. R. Aussenegg, *Two-dimensional optics with surface plasmon polaritons,* Appl. Phys. Lett. **81**, 1762–1764 (2002).

[70] R. C. Jin, Y. W. Cao, C. A. Mirkin, K. L. Kelly, G. C. Schatz, and J. G. Zheng, *Photoinduced conversion of silver nanospheres to nanoprisms,* Science **294**, 1901–1903 (2001).

[71] T. W. Ebbesen, H. J. Lezec, H. F. Ghaemi, T. Thio, and P. A. Wolff, *Extraordinary optical transmission through sub-wavelength hole arrays,* Nature **391**, 667–669 (1998).

[72] R. Ortuno, C. Garcia-Meca, F. J. Rodriguez-Fortuno, A. Hakansson, A. Griol, J. Hurtado, J. A. Ayucar, L. Bellieres, P. J. Rodriguez, F. Lopez-Royo, J. Marti, and A. Martinez, *Midinfrared filters based on extraordinary optical transmission through subwavelength structured gold films,* J. Appl. Phys. **106**, 124313 (2009).

[73] J. M. Vigoureux and D. Courjon, *Detection of nonradiative fields in light of the heisenberg uncertainty principle and the rayleigh criterion,* Appl. Optics **31**, 3170–3177 (1992).

[74] E. H. Synge, *A suggested method for extending microscopic resolution into the ultramicroscopic region,* Philos. Mag. **6**, 356 – 362 (1928).

[75] E. A. Ash and G. Nicholls, *Super-resolution aperture scanning microscope,* Nature **237**, 510 (1972).

[76] A. Lewis, M. Isaacson, A. Harootunian, and A. Muray, *Development of a 500 angstrom spatial-resolution light-microscope .1. light is efficiently transmitted through λ/16 diameter apertures,* Ultramicroscopy **13**, 227–231 (1984).

[77] D. W. Pohl, W. Denk, and M. Lanz, *Optical stethoscopy - image recording with resolution lambda/20,* Appl. Phys. Lett. **44**, 651–653 (1984).

[78] U. C. Fischer and D. W. Pohl, *Observation of single-particle plasmons by near-field optical microscopy,* Phys. Rev. Lett. **62**, 458–461 (1989).

[79] F. d. Fornel, *Evanescent waves : from Newtonian optics to atomic optics,* 3-540-65845-9, Springer (2001).

[80] P. Gleyzes, A. C. Boccara, and R. Bachelot, *Near-field optical microscopy using a metallic vibrating tip,* Ultramicroscopy **57**, 318–322 (1995).

[81] M. Schnell, A. Garcia-Etxarri, A. J. Huber, K. B. Crozier, A. Borisov, J. Aizpurua, and R. Hillenbrand, *Amplitude- and phase-resolved near-field mapping of infrared antenna modes by transmission-mode scattering-type near-field microscopy,* J. Phys. Chem. C **114**, 7341–7345 (2010).

[82] T. J. Yang, G. A. Lessard, and S. R. Quake, *An apertureless near-field microscope for fluorescence imaging,* Appl. Phys. Lett. **76**, 378–380 (2000).

[83] A. Hartschuh, E. J. Sanchez, X. S. Xie, and L. Novotny, *High-resolution near-field raman microscopy of single-walled carbon nanotubes,* Phys. Rev. Lett. **90**,095503 (2003).

[84] S. Takahashi, T. Fujimoto, K. Kato, and I. Kojima, *High resolution photon scanning tunneling microscope,* Nanotechnology **8**, A54–A57 (1997).

[85] M. Balistreri, *Coherent imaging of guided optical fields,* 90-365-14924, PhD thesis, University of Twente, Enschede (2000).

[86] D. Richards, *Near-field microscopy: throwing light on the nanoworld,* Philos. T. Roy. Soc. A **361**, 2843–2857 (2003).

[87] D. Courjon, K. Sarayeddine, and M. Spajer, *Scanning tunneling optical microscopy,* Opt. Commun. **71**, 23–28 (1989).

[88] G. Binnig, H. Rohrer, C. Gerber, and E. Weibel, *Tunneling through a controllable vacuum gap,* Appl. Phys. Lett. **40**, 178–180 (1982).

[89] E. Hecht, *Optics,* 0-201-83887-7, Addison Wesley (1998).

[90] L. Salomon, F. de Fornel, and J. P. Goudonnet, *Sample tip coupling efficiencies of the photon-scanning tunneling microscope,* J. Opt. Soc. Am. A **8**, 2009–2015 (1991).

[91] R. Quidant, J. Webber, A. Dereux, D. Payrade, Y. Chen, and G. Girard, *Near-field observation of evanescent light wave coupling in subwavelength optical waveguides,* Europhys. Lett. **57**, 191–197 (2002).

[92] F. de Fornel, L. Salomon, P. Adam, E. Bourillot, J. P. Goudonnet, and M. Neviere, *Resolution of the photon scanning tunneling microscope - influence of physical parameters,* Ultramicroscopy **42**, 422–429 (1992).

[93] D. Courjon, J. M. Vigoureux, M. Spajer, K. Sarayeddine, and S. Leblanc, *External and internal-reflection near-field microscopy - experiments and results,* Appl. Optics **29**, 3734–3740 (1990).

[94] K. Karrai and R. D. Grober, *Piezoelectric tip-sample distance control for near-field optical microscopes,* Appl. Phys. Lett. **66**, 1842–1844 (1995).

[95] M. Garciaparajo, E. Cambril, and Y. Chen, *Simultaneous scanning tunneling microscope and collection mode scanning near-field optical microscope using gold coated optical-fiber probes,* Appl. Phys. Lett. **65**, 1498–1500 (1994).

[96] E. Betzig, P. L. Finn, and J. S. Weiner, *Combined shear force and near-field scanning optical microscopy,* Appl. Phys. Lett. **60**, 2484–2486 (1992).

[97] M. L. M. Balistreri, J. P. Korterik, L. Kuipers, and N. F. van Hulst, *Photon scanning tunneling optical microscopy with a three-dimensional multiheight imaging mode,* Appl. Phys. Lett. **77**, 4092–4094 (2000).

[98] Y. Toda and M. Ohtsu, *High-spatial-resolution diagnostics of optical wave-guides using a photon-scanning tunneling microscope,* IEEE Photonic. Tech. L. **7**, 84–86 (1995).

[99] D. P. Tsai, J. Kovacs, Z. H. Wang, M. Moskovits, V. M. Shalaev, J. S. Suh, and R. Botet, *Photon scanning-tunneling-microscopy images of optical-excitations of fractal metal colloid clusters,* Phys. Rev. Lett. **72**, 4149–4152 (1994).

[100] R. M. Vazquez, R. Osellame, D. Nolli, C. Dongre, H. van den Vlekkert, R. Ramponi, M. Pollnau, and G. Cerullo, *Integration of femtosecond laser written optical waveguides in a lab-on-chip,* Lab Chip **9**, 91–96 (2009).

[101] M. L. M. Balistreri, J. P. Korterik, G. J. Veldhuis, L. Kuipers, and N. F. van Hulst, *Quantitative photon tunneling and shear-force microscopy of planar waveguide splitters and mixers,* J. Appl. Phys. **89**, 3307–3314 (2001).

[102] M. L. M. Balistreri, J. P. Korterik, L. Kuipers, and N. F. van Hulst, *Local observations of phase singularities in optical fields in waveguide structures,* Phys. Rev. Lett. **85**, 294–297 (2000).

[103] A. Nesci, R. Dandliker, M. Salt, and H. P. Herzig, *Measuring amplitude and phase distribution of fields generated by gratings with sub-wavelength resolution,* Opt. Commun. **205**, 229–238 (2002).

[104] E. Fluck, M. Hammer, A. M. Otter, J. P. Korterik, L. Kuipers, and N. F. van Hulst, *Amplitude and phase evolution of optical fields inside periodic photonic structures,* J. Lightwave Technol. **21**, 1384–1393 (2003).

[105] M. Burresi, R. J. P. Engelen, A. Opheij, D. van Oosten, D. Mori, T. Baba, and L. Kuipers, *Observation of polarization singularities at the nanoscale,* Phys. Rev. Lett. **102**, 033902 (2009).

[106] M. L. M. Balistreri, H. Gersen, J. P. Korterik, L. Kuipers, and N. F. van Hulst, *Tracking femtosecond laser pulses in space and time,* Science **294**, 1080–1082 (2001).

[107] H. Gersen, T. J. Karle, R. J. P. Engelen, W. Bogaerts, J. P. Korterik, N. F. van Hulst, T. F. Krauss, and L. Kuipers, *Real-space observation of ultraslow light in photonic crystal waveguides,* Phys. Rev. Lett. **94**, 073903 (2005).

[108] E. Verhagen, M. Spasenovic, A. Polman, and L. Kuipers, *Nanowire plasmon excitation by adiabatic mode transformation,* Phys. Rev. Lett. **102**, 203904 (2009).

[109] C. S. Lindquist and F. K. Urban, *Surface analysis algorithms for scanning probe microscopy,* Thin Solid Films **270**, 399–405 (1995).

[110] S. C. Kitson, W. L. Barnes, and J. R. Sambles, *Full photonic band gap for surface modes in the visible,* Phys. Rev. Lett. **77**, 2670–2673 (1996).

[111] G. Steiner, *Surface plasmon resonance imaging,* Analytical Bioanalytical Chem. **379**, 328–331 (2004).

[112] S. A. Shen, T. Liu, and J. H. Guo, *Optical phase-shift detection of surface plasmon resonance,* Appl. Optics **37**, 1747–1751 (1998).

[113] V. Kochergin, A. Beloglazov, M. Valeiko, and P. Nikitin, *Phase properties of a surface-plasmon resonance from the viewpoint of sensor applications,* Quantum Electron. **28**, 444–448 (1998).

[114] F. Abeles and T. Lopezrioz, *Decoupled optical excitation of surface plasmons at two surfaces of a thin-film,* Opt. Commun. **11**, 89–92 (1974).

[115] K. M. Medicus, M. Chaney, J. E. Brodziak, and A. Davies, *Interferometric measurement of phase change on reflection,* Appl. Optics **46**, 2027–2035 (2007).

[116] M. McGuirk and C. K. Carniglia, *Angular spectrum representation approach to goos-hanchen shift,* J. Opt. Soc. Am. **67**, 103–107 (1977).

[117] C. F. Li, T. Duan, and X. Y. Yang, *Giant goos-hänchen displacement enhanced by dielectric film in frustrated total internal reflection configuration,* J. Appl. Phys. **101**, 013103 (2007).

[118] I. V. Shadrivov, A. A. Zharov, and Y. S. Kivshar, *Giant goos-hänchen effect at the reflection from left-handed metamaterials,* Appl. Phys. Lett. **83**, 2713–2715 (2003).

[119] P. Mazur and B. Djafarirouhani, *Effect of surface-polaritons on the lateral displacement of a light-beam at a dielectric interface,* Phys. Rev. B **30**, 6759–6762 (1984).

[120] A. Puri and J. L. Birman, *Goos-hänchen beam shift at total internal-reflection with application to spatially dispersive media,* J. Opt. Soc. Am. A **3**, 543–549 (1986).

[121] X. B. Yin and L. Hesselink, *Goos-hänchen shift surface plasmon resonance sensor,* Appl. Phys. Lett. **89**, 261108 (2006).

[122] K. Kiersnowski, L. Jozefowski, and T. Dohnalik, *Effective optical anisotropy in evanescent wave propagation in atomic vapor,* Phys. Rev. A **57**, R4079–R4081 (1998).

[123] F. de Fornel, P. M. Adam, L. Salomon, J. P. Goudonnet, A. Sentenac, R. Carminati, and J. J. Greffet, *Analysis of image formation with a photon scanning tunneling microscope,* J. Opt. Soc. Am. A **13**, 35–45 (1996).

[124] C. Carniglia and L. Mandel, *Phase-shift measurement of evanescent electromagnetic waves,* J. Opt. Soc. Am. **61**, 1035 (1971).

[125] G. Stabler, M. G. Somekh, and C. W. See, *High-resolution wide-field surface plasmon microscopy,* J. Microsc. **214**, 328–333 (2004).

[126] C. J. Alleyne, A. G. Kirk, R. C. McPhedran, N. A. P. Nicorovici, and D. Maystre, *Enhanced spr sensitivity using periodic metallic structures,* Opt. Express **15**, 8163–8169 (2007).

[127] C. Bonnet, D. Chauvat, O. Emile, F. Bretenaker, A. L. Floch, and L. Dutriaux, *Measurement of positive and negative goos-hänchen effects for metallic gratings near wood anomalies,* Opt. Lett. **26**, 666–668 (2001).

[128] R. Petit, *Electromagnetic Theory of Gratings*, 978-0387101934, Springer-Verlag Berlin (1980).

[129] M. Veith, K. G. Muller, S. Mittlerneher, and W. Knoll, *Propagation and deflection of guided modes in planar wave-guides via grating rotation,* Appl. Phys. B **60**, 1–4 (1995).

[130] D. Beaglehole, *Coherent and incoherent radiation from optically excited surface plasmons on a metal grating,* Phys. Rev. Lett. **22**, 708–711 (1969).

[131] G. P. Bryanbrown, J. R. Sambles, and M. C. Hutley, *Polarization conversion through the excitation of surface-plasmons on a metallic grating,* J. Mod. Optic. **37**, 1227–1232 (1990).

[132] T. Inagaki, J. P. Goudonnet, J. W. Little, and E. T. Arakawa, *Photoacoustic study of plasmon-resonance absorption in a bigrating,* J. Opt. Soc. Am. B **2**, 433–439 (1985).

[133] *DiffractMOD* (Rsoft Design Group, Ossining, NY).

[134] M. G. Moharam and T. K. Gaylord, *Rigorous coupled-wave analysis of planar-grating diffraction,* J. Opt. Soc. Am. **71**, 811–818 (1981).

[135] D. Kim, *Effect of the azimuthal orientation on the performance of grating-coupled surface-plasmon resonance biosensors,* Appl. Optics **44**, 3218–3223 (2005).

[136] H. W. Gao, J. Henzie, M. H. Lee, and T. W. Odom, *Screening plasmonic materials using pyramidal gratings,* Natl. Acad. Sci. USA **105**, 20146–20151 (2008).

[137] A. A. Maradudin, *Iterative solutions for electromagnetic scattering by gratings,* J. Opt. Soc. Am. **73**, 759–764 (1983).

[138] J. Chandezon, M. T. Dupuis, G. Cornet, and D. Maystre, *Multicoated gratings - a differential formalism applicable in the entire optical-region,* J. Opt. Soc. Am. **72**, 839–846 (1982).

[139] I. Pockrand, *Resonance anomalies in light-intensity reflected at silver gratings with dielectric coatings,* J. Phys. D Appl. Phys. **9**, 2423–2432 (1976).

[140] U. Schroter and D. Heitmann, *Grating couplers for surface plasmons excited on thin metal films in the Kretschmann-Raether configuration,* Phys. Rev. B **60**, 4992–4999 (1999).

[141] M. Hegner, P. Wagner, and G. Semenza, *Ultralarge atomically flat template-stripped au surfaces for scanning probe microscopy,* Surf. Science **291**, 39–46 (1993).

[142] Y. L. Jin, J. Y. Chen, L. Xu, and P. N. Wang, *Refractive index measurement for biomaterial samples by total internal reflection,* Phys. Med. Biol. **51**, N371–N379 (2006).

[143] A. Bouhelier, J. Renger, M. R. Beversluis, and L. Novotny, *Plasmon-coupled tip-enhanced near-field optical microscopy,* J. Microsc-oxford **210**, 220–224 (2003).

[144] M. I. Stockman, *Nanofocusing of optical energy in tapered plasmonic waveguides,* Phys. Rev. Lett. **93**, 137404 (2004).

[145] N. C. Lindquist, P. Nagpal, A. Lesuffleur, D. J. Norris, and S. H. Oh, *Three-dimensional plasmonic nanofocusing,* Nano Lett. **10**, 1369–1373 (2010).

[146] A. Rueda and N. Vogel and M. Kreiter, *Characterization of gold films by surface plasmon spectroscopy: Large errors and small consequences,* Surf. Science **603**, 491–497 (2009)

Summary

This thesis presents results of a near-field investigation of Surface Plasmon Polaritons (SPPs) on gold thin films and gratings, using a heterodyne interferometric Photon Scanning Tunneling Microscope (PSTM). The ideas described in the thesis are intended to improve the sensitivity and dynamic range of bio-sensors.

The interaction of light with metals contains a resonant phenomenon called the Surface Plasmon Resonance (SPR). SPPs are sensitive to a change in the refractive index of the bounding medium. The level of sensitivity depends on the sharpness of the resonance, which depends on the propagation length of SPPs on the metal surface.

The dynamic range of SPR sensors can be improved by corrugating the metal surface. The SPPs propagating on a corrugated metal surface will scatter back to radiation, which decreases the propagation length and broaden the SPP resonance. Hence it becomes important to design the corrugation in such a way that the dynamic range of a SPR sensor is preserved, without compromising the sensor's sensitivity.

In Chapter 2, an introduction to plasmonics is given, emphasizing the generation of SPPs on metal thin films. An optical coupling to SPPs is only possible by increasing the momentum of light, since the SPP momentum is higher than that of light in free space. The prism and the grating coupling schemes to excite SPPs are described. The thickness of the metal film divides the coupling of SPPs into three regimes: under-coupling, optimum-coupling and over-coupling. An optimum coupling is achieved when the internal losses in the metal film is equal to the radiative losses. A conventional far-field reflection setup is used to show that SPPs are excited only for p-polarized incident light. Direct detection of SPPs is only possible by perturbing the SPP field by using a sub-wavelength scatterer.

In Chapter 3, a Photon Scanning Tunneling Microscope (PSTM) to image sur-

faces with sub-wavelength resolution is presented. The sub-wavelength resolution is obtained by frustrating evanescent waves using a sharp tapered optical fiber tip. A heterodyne interferometric technique is used to obtain both the amplitude and the phase of the SPP field on a 50 nm thick gold film. Multiple SPPs, excited by combining the prism and the grating coupling schemes, are imaged using the PSTM, and a Fourier analysis untangles the different plane waves propagating on a gold buried grating. Light exiting an integrated optical waveguide embedded in a microchip is imaged using the PSTM, which reveals a radially-symmetric intensity profile.

An interesting property of SPPs, such as the phase shift at SPR, can be extracted by probing the amplitude and phase of the SPP field on a metal surface. In Chapter 4, the extraction of the phase shifts at SPR on two different samples, a flat gold surface and a buried gold grating, is demonstrated. In the case of the 50 nm thick gold film, an adjacent glass region is used as a reference. The difference between the phase of the evanescent wave on the glass and the gold surfaces is measured for varying incident angles. A phase shift of 130° is measured over the SPR region, which agrees with the theoretical prediction. In the case of the gold buried grating, the resonant phase shift at SPR is extracted using a non-resonant diffracted order as the reference. The measured resonant phase shift of 133° matches with the theoretical phase.

In Chapter 5, the propagation length of SPPs is investigated for two different types of grating designs: a buried grating and an exposed grating. In a glass-gold-air system, the buried grating has corrugations at the glass-gold interface and the exposed grating has corrugations at the gold-air interface. The PSTM is used to detect the near-field intensities on the gratings. The full width at half maximum (FWHM) of the surface plasmon resonances on the buried grating is reduced to 57% for the prism-coupled SPPs and 77% for the grating-coupled SPPs, in comparison with the exposed grating. The reduction in the FWHM of the SPR implies an increase in the propagation length of SPPs.

The edge of the gratings are imaged using the PSTM and the propagation lengths of SPPs beyond the gratings have been found to be close to the calculated SPP propagation length on an ideal gold surface. Using simulations based on rigorous coupled wave analysis, the figure of merit of a SPR sensor for both gratings are evaluated. At a bio-relevant refractive index of 1.3, a higher figure of merit observed for the buried grating, implies a sensitivity enhancement in grating-incorporated SPR sensors. Finally, a combination of a phase-matched buried grating and a tapered waveguide is proposed as a device for three-dimensional nanofocusing of SPPs.

Samenvatting

In dit proefschrift worden de resultaten gepresenteeerd van het nabije-veld onderzoek naar oppervlakte plasmon polaritonen (SPPs) op dunne goudfilms en goudroosters. Dit onderzoek is uitgevoerd met een heterodyne interferometrische Photon Scanning Tunneling Microscoop (PSTM). De belangrijkste bevindingen in dit proefschrift zijn gericht op het verbeteren van de gevoeligheid en het dynamisch bereik van bio-sensoren.

Bij de interactie van licht met metalen treedt een resonant verschijnsel op, genaamd oppervlakte plasmonresonantie (SPR). SPPs zijn gevoelig voor verandering van de brekingsindex van het omringende medium. De mate van gevoeligheid van een SPR sensor is afhankelijk van de scherpte van de resonantie. Die is op zijn beurt afhankelijk van de propagatie lengte van SPPs op het metaaloppervlak.

Het dynamisch bereik van SPR sensoren kan worden verbeterd door het vervormen van het metaaloppervlak. Echter, de SPPs die zich voortplanten op een vervormd metalen oppervlak ondervinden echter terugverstrooiing naar straling, wat een verbreding van de resonantie tot gevolg heeft. Daarom is het belangrijk om de vervorming van het metaaloppervlak op een zodanige wijze te ontwerpen dat de dynamisch bereik van een SPR sensor wordt verbeterd, zonder afbreuk te doen aan de gevoeligheid van de sensor.

In hoofdstuk 2, wordt een kort overzicht van plasmonics gegeven, waarbij de nadruk ligt op de SPPs op uitgestrekte dunne films. Een optische koppeling aan SPPs is alleen mogelijk door het verhogen van de impuls van het licht, omdat de SPP impuls hoger is dan die van het licht in lucht. De prisma- en rooster-koppeling methodes worden beschreven. De dikte van de metaallaag verdeelt de koppeling van SPPs in drie regimes: onder-koppeling, optimale koppeling en over-koppeling. Een optimale koppeling wordt bereikt wanneer de interne verliezen in de metaalfilm gelijk zijn aan de stralingsverliezen. Een conventionele verre-veld reflectie opstelling wordt gebruikt om aan te tonen dat de SPPs alleen aangeslagen worden door p-gepolariseerd invallend licht. Het direct detecteren van SPPs is alleen mogenlijk door het SPP veld te verstoren door een sub-golflengte verstrooier gebruiken.

In hoofdstuk 3, wordt een PSTM, op het beeld om te oppervlakken met sub-golflengte resolutie gepresenteerd . Sub-golflengte informatie wordt verkregen door het frustreren van de evanescente golven, met een scherpe optische vezel tip. Een heterodyne interferometrie techniek wordt gebruikt om zowel de amplitude als de fase van het SPP-veld op een 50 nm dikke gouden film te verkrijgen. Meerdere SPPs aangeslagen door het combineren van de prisma- en de rooster-koppeling methodes, worden afgebeeld met behulp van de PSTM en een Fourier analyse haalt de verschillende vlakke golven uiteen. Het licht aan the uitgang van een geïntegreerde optische golfgeleider is gescand met behulp van de PSTM.

Een interessante eigenschap van SPPs, zoals de faseverschuiving bij resonantie, kunnen direct worden geëxtraheerd door het meten van de amplitude en fase van het SPP-veld op een metalen oppervlak. Hoofdstuk 4 beschrijft het meten van faseverschuivingen ten gevolge van SPR op twee verschillende oppervlakken: een plat gouden oppervlak en een ingegraven goud rooster. In het geval van een 50 nm dikke gouden film, is een aangrenzende gebied van glas gebruikt als referentie. Het verschil tussen de fase van de golven op het glas en het goud wordt gemeten voor verschillende invalshoeken. Een fase verschuiving van 130° is gemeten over de SPR regio, het geen overeenkomt met de theoretische voorspelling. In het geval van het ingegraven gouden rooster, wordt de resonante faseverschuiving op SPR gemeten met een niet-resonante diffractie orde als referentie. De gemeten resonante faseverschuiving van 133° komt overeen met de theoretische faseverschuiving.

In hoofdstuk 5 is de vermeerdering lengte van SPPs onderzocht voor twee verschillende soorten rooster ontwerpen: een ingegraven rooster en een open rooster. Het ingegraven rooster heeft ribbels op de glas-goud-overgang en het open rooster heeft ribbels op de goud-lucht overgang. De PSTM wordt gebruikt om de intensiteiten te meten op de roosterstructuren. De volle breedte op halve hoogte (FWHM) van de oppervlakte plasmonresonanties op het ingegraven rooster reduceert naar 57% voor de prisma-gekoppelde SPPs en naar 77% voor de rooster-gekoppelde SPPs, in vergelijking met de open rooster. Een vermindering van de FWHM van de SPR impliceert een toename van de verspreiding lengte van SPPs.

De rand van de roosters worden afgebeeld en de propagatie lengtes van SPPs buiten de roosters zijn dicht bij de berekende SPP propagatie lengte op een ideale goud oppervlak. Met behulp van simulaties op basis van sterk gekoppelde golfanalyse, is het rendement van een SPR-sensor voor beide roosters geëvalueerd. Bij een biologisch relevante brekingsindex van 1.3, een hoger rendement wordt voorspeld voor het ingegraven rooster impliceert een verbetering in de gevoeligheid raspenopgenomen SPR sensoren. Ten slotte wordt een ontwerp voorgesteld, bestaande uit een combinatie van een fase-gematcht ingegraven rooster en een taps toelopende golfgeleider, voor drie-dimensionale nanofocussering van SPPs.

Acknowledgements

I express my sincere gratitude to my supervisor Herman Offerhaus, to whom I am deeply grateful for extending his expertise and helpful advice. Herman, working with you I have learnt many things - both scientific and personal - many of which have nurtured me along the road. Thank you for giving me the ultimate freedom in every aspects of my work and for patiently listening to me in times of frustration.

Many thanks to Jeroen and Frans, the 'terrific duo' in the group, for all the technical support in my project. Jeroen, thank you very much for offering help when I got stuck in the unfamiliar Dutch system. I have enjoyed the time we spent in the lab building the PSTM and thank you for your valuable suggestions and contributions in my work. Frans, thank you for the FIB sessions in the clean-room. Fabrication of buried gratings became a lot faster with your timely involvement. I have learnt from you to 'never stop doing things just because you fail; keep on trying and you will succeed'. Talking to you is highly motivational.

Jennifer, thank you for being my promotor and for extending your support. Kobus, thank you for being my mentor since last year and for your understanding and guidance. I am grateful to Bill Barnes, Jurriaan Huskens and Martin van Exter for participating in my thesis defense.

Thanks to NanoNed for financially supporting the project and for the fruitful user committee meetings. Thank you, Hans Mertens and Huib van Vossen for the fast response to my occasional scientific questions. A special thanks to Vishwas Gadgil for the assistance in FIB work on a really short notice. Thanks to Alberto and Chaitanya for the collaborations. Karen, thank you for helping me with the paper works right from the beginning. I think we both will never forget the fun we had when we were lost in Barcelona...

Many thanks to Di for your thoughtful suggestions and for being a good listener. I wish you *All The Best* for your upcoming PhD defense. Robert, thank you for the

nice time we spend together in T10. Little did I knew about NSOM, I am sure you have enjoyed answering my questions, like I have enjoyed listening to you. Thank you Stytse for the occasional after work dinner, Jacob and Ali for the insightful chats, Martin for the funny moments inbetween (especially my biking lessons). Furthermore, thank you Oya, Ewout, Leila, Dan, Dirk Jan, Daan, Erik, Simon, Alexander, Eric, Alyssa, Erwin, Joris, Bob, Kasper, Jorick, Wietske, Pepijn and Philip for the rewarding scientific and social get togethers. Thanks to those who helped me by correcting the thesis; especially Ali, thank you for the discussions that followed.

Doing a PhD is not just working in the lab. There are some people who have made my stay in the Netherlands as lively and homely as possible. First of all, thanks to my house mates Xiaoying, Xinyan, Shu-Han, and Denny for the nice time we shared. Shu-Han and Xiaoying, many thanks for taking good care of me after my foot injury. Thanks to Rani, Sumy, Somayeh, Banu, Hrudya, Shahina and Musthafa, Mercy and Shaji, Indu and Babu for the occasional recharging events. Lily, I am glad to know you. Thank you for your hospitality, especially the regular *Sunday coffee*, and the nice time we spent together. I would like to thank Dr. Anil Peters for the prompt help after my foot injury, and Dr. Prasad Varkey and Rene Polman for assistance in the recovery stage.

Most sincerely, I express my heartfelt gratitude to my parents. Without your unconditional love and blessings, I would not have come so far. Thank you, Jesmy and Shaine, Jainy, Jissy and Mathew for your love, support and for just being a terrific family. Above all I thank God for the uncountable blessings showered upon me and for guiding me towards hope.

Enschede,
October 2010

Jincy Jose

Scientific contributions

- *Near-field observation of spatial phase-shifts associated with Goos-Hänschen and Surface Plasmon Resonance effects*, J. Jose, F. B. Segerink, J. P. Korterik and H. L. Offerhaus, Opt. Express **16**, 3 (2008).
- *Enhanced surface plasmon polariton propagation length using a buried gold grating*, J. Jose, F. B. Segerink, J. P. Korterik, A. Gomez-Casado, J. Huskens, J. L. Herek, and H. L. Offerhaus, submitted to J. Appl. Phys. (September 2010).
- *Imaging of surface plasmon polariton interference using phase-sensitive Photon Scanning Tunneling Microscope*, J. Jose, F. B. Segerink, J. P. Korterik, J. L. Herek and H. L. Offerhaus, submitted to J. Appl. Phys. A - Special issue.
- *Near-field extraction of phase shift at surface plasmon resonance on a metal grating*, J. Jose, J. P. Korterik, F. B. Segerink, J. L. Herek and H. L. Offerhaus, in preparation.
- *Template-stripped buried grating for plasmonics*, J. Jose, F. B. Segerink, J. P. Korterik, J. L. Herek, L. Kuipers and H. L. Offerhaus, Gordon Research Conference on Plasmonics, 13-18 June 2010, Colby college, Maine, United States. (Poster)
- *Imaging of Surface Plasmon Polariton interference using phase-sensitive Photon Scanning Tunneling Microscope*, J. Jose, F. B. Segerink, J. P. Korterik, J. L. Herek and H. L. Offerhaus, International conference on Metamaterials, Photonic Crystals and Plasmonics, 22-25 February 2010, Cairo, Egypt. (Oral)
- *Azimuthal dispersion of surface plasmon polaritons excited via a buried grating*, J. Jose, F. B. Segerink, J. P. Korterik, J. L. Herek and H. L. Offerhaus, Fourth

International conference on Surface Plasmon Photonics (SPP4), 21-26 June 2009, Amsterdam, The Netherlands. (Poster)

- *Combined analysis of Goos-Hänschen and Surface plasmon phase shift using PSTM*, J. Jose, F. B. Segerink, J. P. Korterik and H. L. Offerhaus, Third International conference on Surface Plasmon Photonics (SPP3), 17-22 June 2007, Dijon, France. (Oral)

About the author

Jincy Jose was born on July 16, 1983 in Angamaly, Kerala, India. She obtained her Bachelor (2003) and Master (2005) degree in Physics from Mahatma Gandhi University, India. For her Master's project, she fabricated copper indium diselenide thin films for solar cells, supervised by Prof. M. K. Jayaraj, Cochin University of Science and Technology, India. In March 2006, she joined the Optical Techniques group (currently known as Optical Sciences), University of Twente, The Netherlands, as a PhD student supervised by dr. H. L. Offerhaus. Her work involved building a near-field optical microscope to investigate surface plasmon polaritons on gold thin films and gratings. The results of that work are presented in this thesis. In leisure time she likes to engage in reading and experiment her cooking skills.

ISBN 978-90-365-3091-0